UNIVERSIDAD DE JAÉN

ESCUELA POLITÉCNICA SUPERIOR
DE JAÉN
DEPARTAMENTO DE FÍSICA

TESIS DOCTORAL

DESING AND OPTIMIZATION OF ARTIFICIAL NEURAL NETWORK MODELS FOR SOLAR RESOURCE ASSESSMENT

PRESENTADA POR:
ÁLVARO LINARES RODRÍGUEZ

DIRIGIDA POR:
DR. D. JOAQUÍN TOVAR PESCADOR
DR. D. JOSÉ ANTONIO RUIZ ARIAS

JAÉN, 7 DE JULIO DE 2015

ISBN 978-84-8439-938-4

Design and optimization of Artificial Neural Network models for solar resource assessment

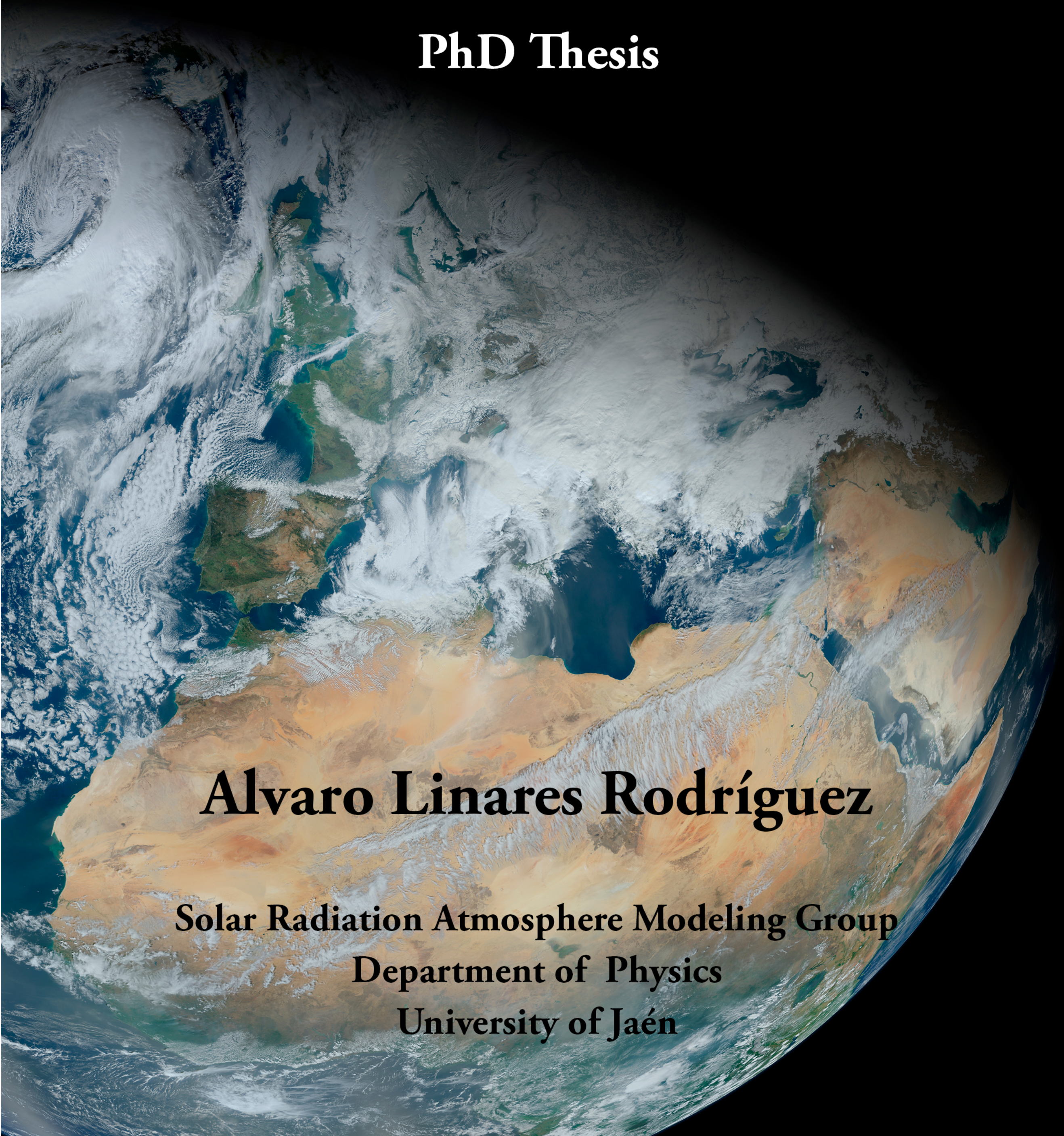

PhD Thesis

Alvaro Linares Rodríguez

Solar Radiation Atmosphere Modeling Group
Department of Physics
University of Jaén

Design and optimization of Artificial Neural Network models for solar resource assessment

PhD THESIS

to obtain the degree of

Doctor by the University of Jaén

Sciences PhD Program

Defended by

Álvaro Linares Rodríguez

Solar Radiation and Atmosphere Modeling Group

Department of Physics

University of Jaén

Thesis Advisors:

Dr. Joaquín Tovar Pescador

Dr. José Antonio Ruiz Arias

May 2015

Diseño y optimización de modelos de Redes Neuronales Artificiales para la evaluación del recurso solar

TESIS DOCTORAL

para obtener el grado de

Doctor por la Universidad de Jaén

Programa de Doctorado en Ciencias

Defendida por

Álvaro Linares Rodríguez

Grupo Modelización de la Atmósfera y Radiación Solar

Departamento de Física

Universidad de Jaén

Directores de Tesis:

Dr. Joaquín Tovar Pescador

Dr. José Antonio Ruiz Arias

Mayo 2015

El **Dr. Joaquín Tovar Pescador**, Catedrático de Escuela Universitaria del Departamento de Física de la Universidad de Jaén, España,

el **Dr. José Antonio Ruiz Arias**, Doctor en Física por la Universidad de Jaén, España,

CERTIFICAN:

Que la presente memoria, titulada "***Design and optimization of Artificial Neural Network models for solar resource assessment***", ha sido realizada bajo su dirección. Y considerando que representa trabajo de Tesis, autorizan su presentación y defensa para optar al grado de Doctor por la Universidad de Jaén.

Dr. Joaquín Tovar Pescador	**Dr. José Antonio Ruiz Arias**
Departamento de Física Universidad de Jaén	Departamento de Física Universidad de Jaén

Memoria presentada para optar al grado de:

Doctor por la Universidad de Jaén

Álvaro Linares Rodríguez

Licenciado en Ciencias Físicas

Jaén, Mayo de 2015

A mi hermana Cristina
que, sin necesidad de estudios ni doctorados,
posee una verdadera sabiduría
de la que intento aprender cada día.

AGRADECIMIENTOS

Toda tesis es el final de un trabajoso recorrido y el comienzo de una nueva etapa. En mi caso, ha sido una oportunidad que la vida me ha brindado para disfrutar trabajando en lo que me gusta y, a la vez, un privilegio al poder trabajar y convivir con un grupo humano sencillamente envidiable.

Es difícil agradecer como se merecen a quienes en los últimos cinco años han sido mis compañeros de fatigas y a tantas personas (familiares y amigos) que han sido fundamentales para poder llevar a cabo este proyecto. Me ceñiré al ámbito estrictamente profesional, como reconocimiento a aquellos que más me han ayudado en la tesis. En primer lugar quiero expresar mi agradecimiento a Joaquín, que desde el primer momento me animó a lanzarme a esta aventura y siempre ha confiado en mí más allá de lo razonable. Él me abrió las puertas del grupo de investigación y ha sido para mí un verdadero maestro, en el sentido más amplio de la palabra. En segundo lugar quiero dar las gracias a David, por acogerme desde el minuto cero como si hubiésemos trabajado juntos muchos años. Con ellos he aprendido lo que debe ser un catedrático de universidad, pues han sabido *crear escuela* formando profesional y humanamente a un grupo de jóvenes, ¡entre los que me incluyo!, haciéndonos sentir importantes y ayudándonos a dar lo mejor de nosotros mismos.

Un puesto importante en mi agradecimiento lo ocupa José Antonio, mi co-director de tesis junto a Joaquín. Ha sido para mí el espejo profesional en quien mirarme, ejemplo de laboriosidad y demostración de que para ser sabio no hay que esperar a que pase el tiempo sino más bien aprovecharlo al máximo. Junto a José Antonio, quiero agradecer a Samuel, Vicente, Paco y Pepe tantos favores y vivencias compartidas, incluida una aventura empresarial prometedora. No es sencillo reunir tanta calidad científica y tanta calidad humana: con ellos es fácil aprender, incluso las claras deficiencias intelectuales de uno se ven atenuadas junto a ellos solo por ósmosis… Es un orgullo presumir de amistad con ellos, siempre atentos a ayudar, siempre disponibles para las dudas, siempre tendiendo la mano. ¡Gracias!

No puedo olvidarme de agradecer por último la colaboración y ayuda de Javi y Clara, los más jóvenes en incorporarse al grupo. Además, sin ellos sería más aburrido el trabajo diario. Espero que se hayan sentido acogidos igual de bien que como nos sentimos antes otros.

CONTENTS

TABLES

FIGURES

ACRONYMS

AEMET	Spanish National Weather Service
AIC	Akaike Information Criterion
ANN	Artificial Neural Network
BSRN	Baseline Surface Radiation Network
CSP	Concentrating Solar Power
DEM	Digital Elevation Model
DNI	Direct Normal Irradiance
ECMWF	European Centre for Medium-Range Weather Forecasts
ERA-Interim	ECMWF ReAnalysis-interim
ESRA	European Solar Radiation Atlas
EUMETSAT	European Organization for Exploitation of Meteorological Satellites
GA	Genetic Algorithm
GHI	Global Horizontal Irradiance
GIS	Geographical Information Systems
IEA	International Energy Agency
MBE	Mean Bias Error
MFG	Meteosat First Generation
MLP	Multi Layer Perceptron
MSG	Meteosat Second Generation
OCDE	Organización para la Cooperación y el Desarrollo Económicos
PIV	Particle Image Velocimetry
PV	PhotoVoltaic
RMSE	Root Mean Square Error
rRMSE	relative Root Mean Square Error
SEVIRI	Spinning Enhanced Visible and Infrared Imager
SKT	Skin temperature, i.e. surface temperature (ERA-Interim data)
SRTM	Shuttle Radar Topography Mission
TCC	Total cloud cover (ERA-Interim data)
TCO	Total column of ozone (ERA-Interim data)
TCW	Total column of water vapour (ERA-Interim data)
TL	Turbidity factor of Linke

UTC	Universal Time Coordinate
WRF	Weather Research and Forecasting model
WWS	Water, Wind, Solar energy

CHAPTER 1

INTRODUCCIÓN

1. Introducción

Hoy en día son ampliamente reconocidos los numerosos beneficios del uso de fuentes de energía renovables frente al uso de combustibles fósiles. En los últimos años se está haciendo un gran esfuerzo internacional en aumentar la proporción de renovables en el sistema global de energía, actualmente dominado en más de un 80% por combustibles fósiles. Según la Agencia Internacional de la Energía (IEA, 2014) para 2040 el suministro energético mundial se dividirá en cuatro partes, casi iguales: petróleo, gas, carbón y fuentes de bajas emisiones de CO_2 (donde se incluyen la energía nuclear y las renovables). La proporción de renovables será mayor en algunas regiones, llegando al 37% de la generación eléctrica, por ejemplo, en los países pertenecientes a la Organización para la Cooperación y el Desarrollo Económicos (OCDE). Las renovables representarán casi la mitad del incremento de la generación eléctrica mundial hasta 2040 (cfr. Fig. 1), mientras que el uso de biocombustibles será más del triple que el actual.

La expansión del uso de renovables está ligada principalmente a dos pilares fundamentales (Johansson, 2013): la disminución del cambio climático y el aumento en la seguridad energética. Como ejemplo, sólo por el hecho de establecer unos objetivos de reducción de emisiones de gases de efecto invernadero en sus políticas energéticas, un territorio puede conectar las diferentes piezas del puzle de la energía: seguridad energética, desarrollo económico, innovación tecnológica y protección medioambiental (deLlano-Paz et al., 2015).

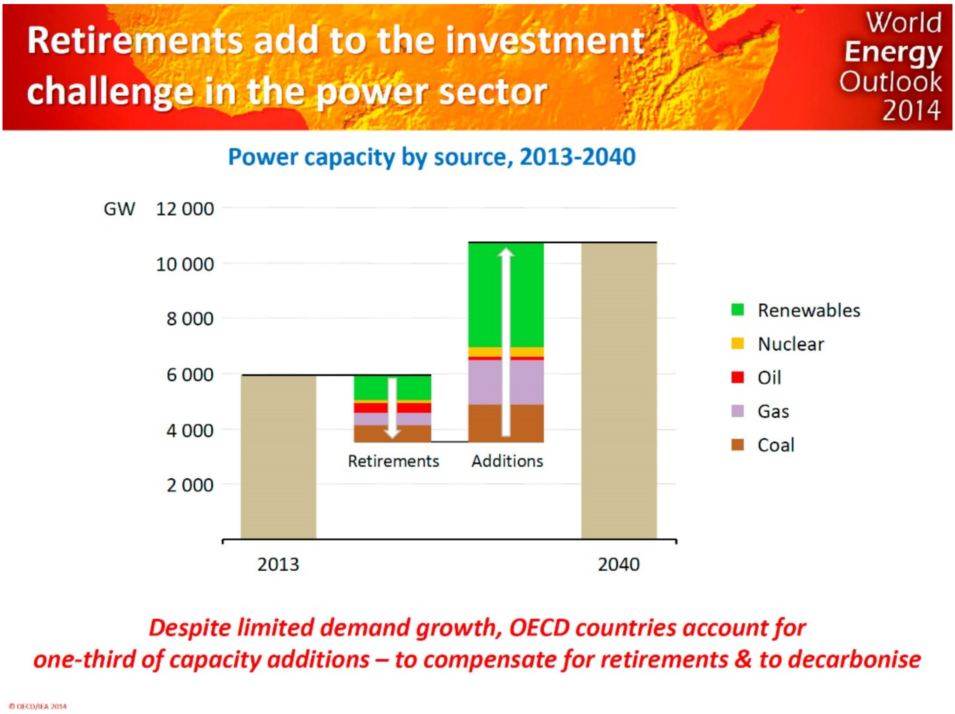

Retirements add to the investment challenge in the power sector

World Energy Outlook 2014

Power capacity by source, 2013-2040

Despite limited demand growth, OECD countries account for one-third of capacity additions – to compensate for retirements & to decarbonise

© OECD/IEA 2014

Figura 1. Previsión de crecimiento de fuentes de energía para 2040. (Fuente: IEA 2014)

Estos pilares han motivado un cambio en las políticas energéticas de muchos países hacia un favorecimiento de las tecnologías renovables. Así por ejemplo, como parte de su política energética y climática, la Unión Europea se marcó los objetivos denominados «20-20-20» para 2020: reducción de un 20% en el consumo de energía primaria (eficiencia energética), reducción vinculante del 20% de las emisiones de gases de efecto invernadero y una cuota de energías renovables del 20% en el consumo de energía final para 2020. También se marcó como objetivo alcanzar un 10% de cuota de renovables en el transporte para 2020 (European_Commission, 2009). Estos objetivos han sido recientemente actualizados y aumentados, gracias a los avances significativos logrados en los últimos años. Así, para 2030 se ha fijado como meta un 40% de reducción de las emisiones de gases de efecto invernadero, al menos una cuota –vinculante– del 27% de renovables en el consumo final de energía, y se han renovado ambiciones en políticas de eficiencia energética para alcanzar el anterior objetivo del 20% (European_Commission, 2014a).

Este último objetivo de eficiencia y ahorro energético está íntimamente ligado al incremento de la cuota de energía procedente de fuentes renovables y a la disminución del cambio climático, de forma que los tres objetivos se complementan mutuamente (European_Commission, 2008; Harmsen et al., 2011; European_Commission, 2012; European_Commission, 2014b).

Algunos autores sostienen que las energías renovables, más concretamente la hidroeléctrica, la eólica y la solar (energías WWS por sus siglas en inglés), serían capaces de satisfacer la demanda mundial de energía para 2030 si se toman una serie de medidas –razonables y factibles– a nivel internacional, y pronostican que para 2050 podrá ser real la conversión de toda la tecnología energética actual a tecnología WWS (Jacobson, 2009; Delucchi and Jacobson, 2011; Jacobson and Delucchi, 2011).

Destacamos a continuación algunos de los beneficios reconocidos internacionalmente del uso de energías renovables, incluyendo los dos principales citados antes de disminución del cambio climático y seguridad energética (deLlano-Paz et al., 2015):

a) Disminución de las emisiones de CO_2 y otros gases contaminantes que afectan críticamente al medioambiente y al cambio climático: calentamiento global de la superficie de la Tierra, aumento del nivel del mar, proliferación de lluvias ácidas, disminución de la capa de ozono, polución del aire, etc. Las renovables son tecnologías limpias y generan pocos residuos.
b) Reducción de pérdidas económicas debidas al cambio climático. Los efectos del cambio climático generan importantes perjuicios económicos, que se han estimado recientemente en pérdidas entre el 4 y el 20% del PIB (producto interior bruto) mundial (Valentine, 2011).
c) Las fuentes renovables tienen disponibilidad casi ilimitada a diferencia de los combustibles fósiles.
d) Reducen la dependencia energética de otros territorios, y por tanto, aumentan la seguridad de suministro y minimizan el riesgo de trastornos de suministro por razones geopolíticas (IEA 2014). No solo los combustibles son caros, sino que su precio es muy dependiente de factores económico-políticos que manejan unos pocos países exportadores. La reciente crisis de Ucrania no hace sino confirmar los riesgos de un sistema energético basado principalmente en importaciones de combustibles fósiles.

e) La naturaleza local de las renovables genera riqueza en el territorio donde están implantadas: tanto directamente, al invertir en nuevas tecnologías renovables, generando también nuevos puestos de trabajo en el territorio; como indirectamente por el beneficio global en el sistema energético al reducir costes dependientes de combustibles fósiles (Johansson, 2013).

Entre las contrapartidas de la implantación de energías renovables están las siguientes:

a) La inseguridad causada por la disponibilidad intermitente del recurso renovable. El recurso renovable varía entre áreas geográficas y a lo largo del tiempo. Esta variabilidad y disponibilidad espacial y temporal de las fuentes de energía renovables afectan tanto a la planificación de nuevas plantas como a su operatividad y a su inclusión en el sistema eléctrico (Widén et al., 2015).
b) La necesidad de una fuerte inversión tanto en la creación de nuevas infraestructuras renovables como en la modificación del sistema energético actual, adaptándose a las características propias de estas fuentes de energía alternativas (como la eólica y la solar) y asegurando por tanto la fiabilidad del suministro eléctrico. Esto requerirá, en algunos casos, reformas del diseño del mercado y de cómo se fijan los precios de la electricidad. Las cargas y demoras administrativas siguen creando dificultades e incrementan el nivel de riesgo de los proyectos de energías renovables; persisten los retrasos en las conexiones y las normas de explotación de la red que perjudican a los productores de energía renovable (IEA, 2014).
c) Necesidad de un marco económico de ayudas seguro que garanticen las inversiones oportunas. La actual coyuntura de crisis económica ha frenado las ayudas así como la confianza de los inversores, debido a los cambios de estrategias económicas en muchos territorios.

Al margen de los inconvenientes que dependen de factores geopolíticos, la variabilidad en la disponibilidad del recurso renovable es el punto crítico. Dos son los principales factores que determinan las posibilidades de crecimiento de estas fuentes dentro de los sistemas eléctricos existentes:

1) una evaluación fiable del recurso renovable a lo largo de decenas de años, incluyendo su variabilidad temporal, así como la producción eléctrica asociada a dicho recurso;

2) la precisión de pronósticos de recurso y producción eléctrica a corto y medio plazo.

Estos dos factores, evaluación y pronóstico de recurso renovable, centran actualmente el debate científico en esta materia (Widén et al., 2015).

Esta tesis se centra explícitamente en la evaluación del recurso solar en zonas de gran extensión geográfica, en las que no existe una red muy densa de medidas de tierra de radiación solar.

Entre todas las fuentes de energía renovables, la energía solar es una de las más abundantes, la fuente de energía que tiene más potencial y la fuente más limpia (Kumar Sahu, 2015). También está reconocida como la industria energética que ha experimentado un crecimiento más rápido, y más expectativas tiene (Kleissl, 2013).

El potencial de la energía solar podemos decir que es casi ilimitado. La radiación solar que alcanza la superficie de la tierra varía desde 0.06 kW/m^2 a altas latitudes a 0.25 kW/m^2 a bajas latitudes. Si tenemos en cuenta la superficie total de tierra del planeta, teóricamente la potencia que se podría obtener del recurso solar sería aproximadamente de 21,840 TW (Kumar Sahu, 2015). Para hacernos una idea de estas cifras, una hora de este recurso solar mundial equivaldría a unas 500 veces el consumo anual de energía en todo el mundo en 2014 (IEA, 2014).

Dos son las tecnologías empleadas para convertir el recurso solar en electricidad: tecnología fotovoltaica y termosolar, más conocidas por sus iniciales en inglés: tecnologías PV (*PhotoVoltaic*) y CSP (*Concentrating Solar Power*).

a) Los sistemas PV utilizan materiales semiconductores para convertir directamente la radiación en electricidad a través del efecto fotoeléctrico. La eficiencia de la célula fotovoltaica es función de la composición del semiconductor y de la intensidad y longitud de onda de la radiación solar incidente. Una célula estándar suele tener una eficiencia en torno al 20%, situándose el récord actual de eficiencia en el 46% (Figura 2).

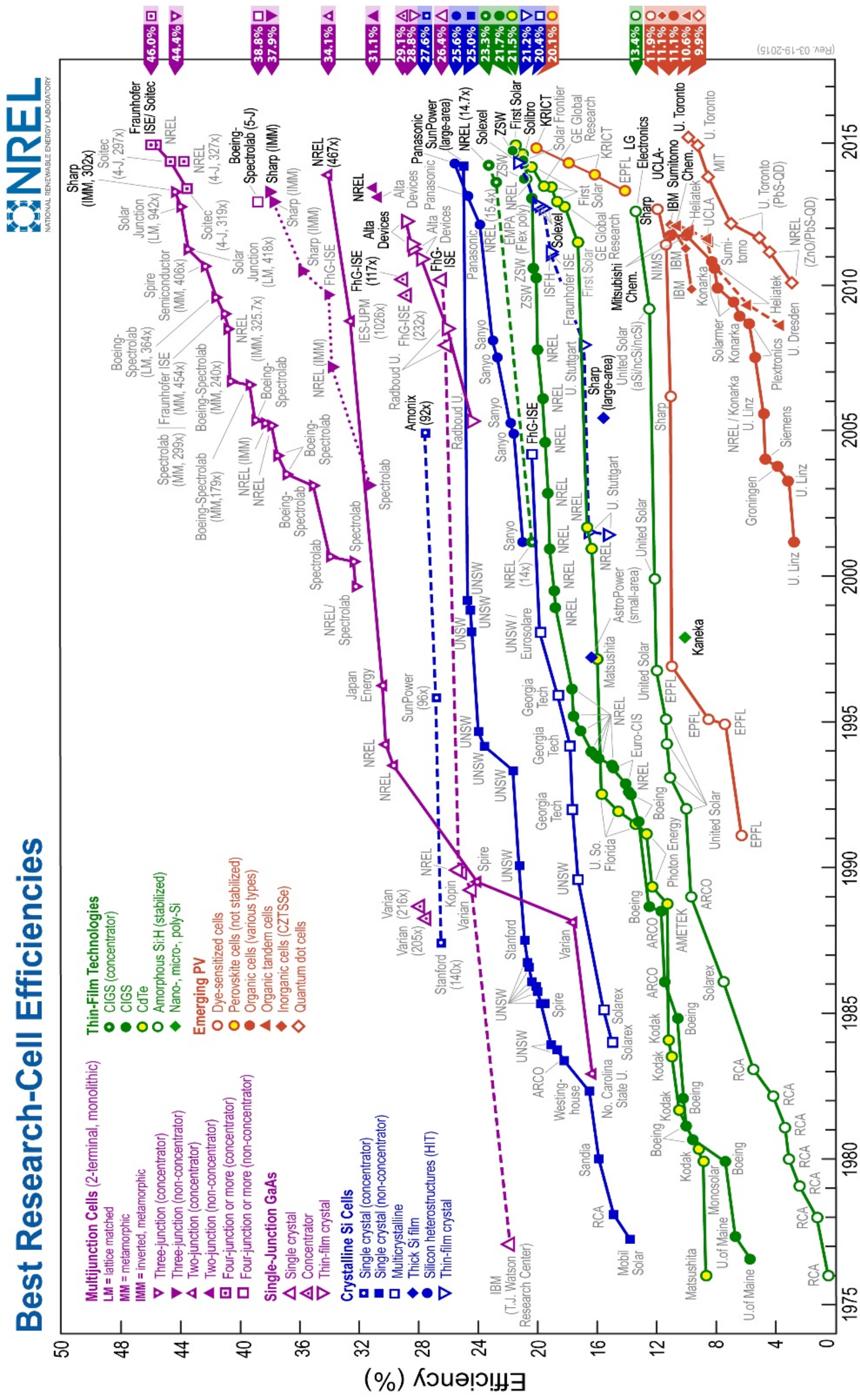

Figura 2. Cronología de las mejoras en eficiencia de células fotovoltaicas desde 1976. El gráfico es cortesía del National Renewable Energy Laboratory, Golden, CO (Estados Unidos).

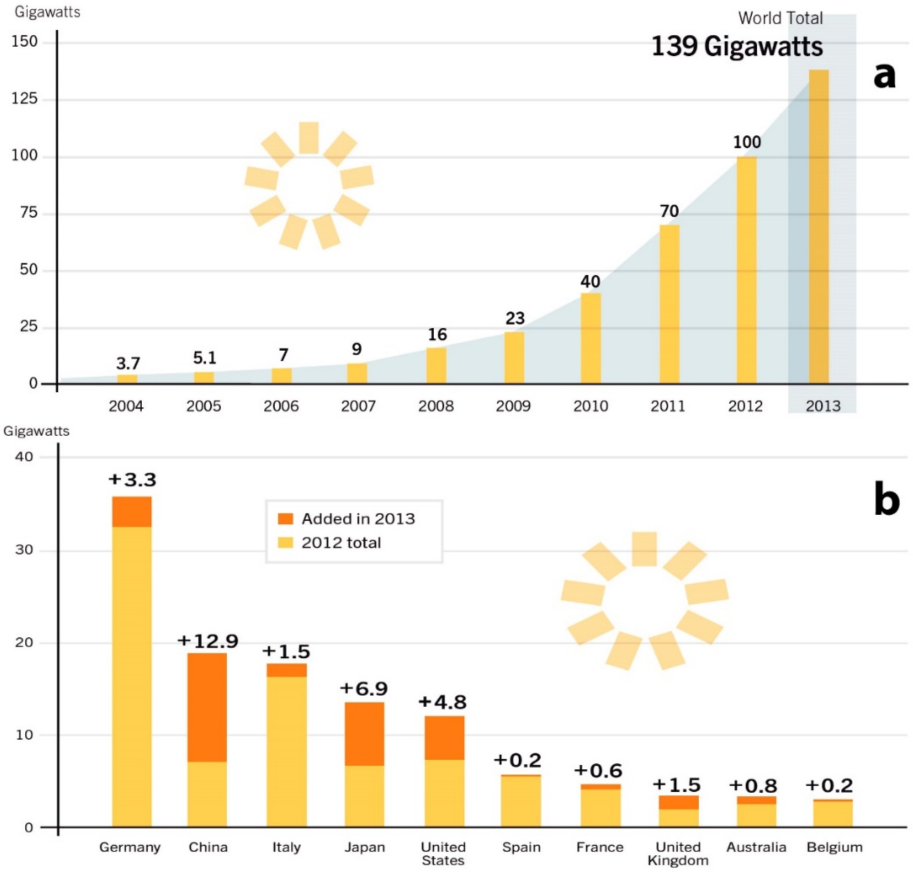

Figura 3. a) Capacidad global total fotovoltaica, 2004–2013. b) Capacidad PV por países, y capacidad añadida en 2013. Fuente: REN21 Renewables 2014. Global Status Report.

b) Los sistemas CSP concentran la radiación solar y la convierten en energía térmica generando vapor, que luego es utilizado para operar una turbina convencional que produce electricidad.

La tecnología fotovoltaica se encuentra mucho más extendida que la térmica, con 139 GW de potencia instalada en todo el mundo en 2013 frente a los 3.4 GW de energía termosolar CSP (cfr. Figuras 3 y 4, REN21 2014).

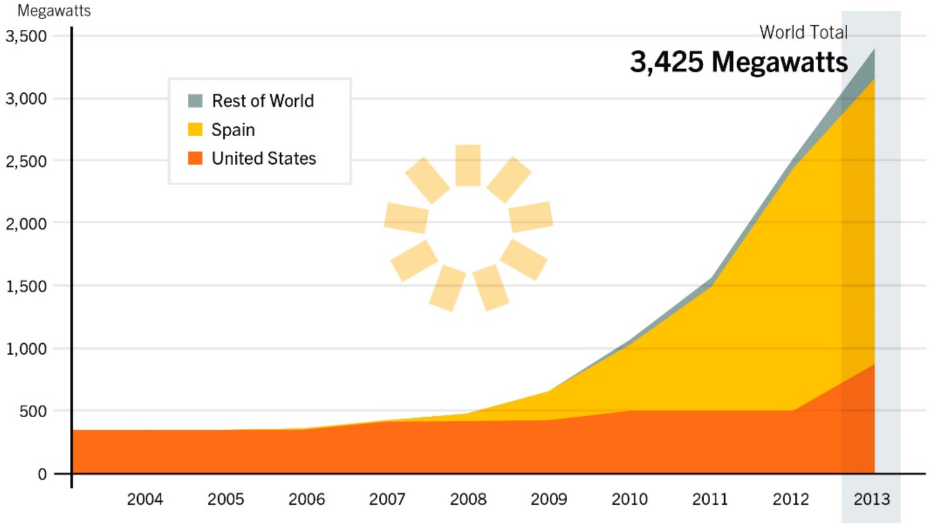

Figura 4 Capacidad global termosolar, 2004–2013. (Fuente: REN21 Renewables 2014. Global Status Report).

Como hemos apuntado anteriormente para las energías renovables en general, hay dos cuestiones que están ahora centrando la investigación y que son del máximo interés para los desarrolladores y promotores de proyectos de energía renovable, y en particular de energía solar, ya sea PV o CSP: la evaluación del recurso solar y el pronóstico solar a corto y medio plazo (Kleissl, 2013; Widén et al., 2015).

Muchos de los riesgos financieros del desarrollo de tecnologías de energía solar se pueden mitigar gracias a:

1) un mejor conocimiento del recurso solar en la zona de estudio, a través por ejemplo de series temporales históricas de radiación solar precisas y de gran resolución espacial y temporal;
2) un sistema fiable de pronóstico del recurso solar que tenga en cuenta su gran variabilidad temporal, tanto a corto plazo como a medio plazo.

La evaluación del recurso solar es fundamental en la fase de proyección de una nueva planta de energía solar. Habitualmente son necesarios mapas de radiación de extensas zonas a lo largo de varias decenas de años para encontrar los emplazamientos óptimos para esas plantas solares. En el siguiente epígrafe explicamos con detalle las dificultades encontradas para obtener esas estimaciones de radiación de alta resolución. Por otro lado, una buena evaluación es el primer paso para algunos de los sistemas de pronóstico del recurso, de forma que el error en la evaluación se superpone al error propio de la predicción (Perez et al., 2010a; Kleissl, 2013). De ahí que sea de principal relevancia disponer de una evaluación de recurso solar de la máxima precisión.

Un sistema óptimo de pronóstico de recurso solar también es importante en la fase de diseño de una planta solar, pero su papel más importante lo juega en la fase de operación de la planta y su inclusión en el mercado eléctrico. Los sistemas de pronóstico solar tienen características específicas dependiendo de la tecnología de conversión utilizada, ya sea PV o CSP. Los sistemas PV generan electricidad no gestionable, es decir, sólo producen electricidad al recibir rayos de sol, no pueden almacenar energía. En cambio, los sistemas CSP sí pueden complementarse con sistemas de almacenamiento, de forma que pueden producir electricidad tanto por el día como por la noche. Los sistemas de pronóstico deben tener en cuenta estas características para asegurar la fiabilidad económica de estos sistemas de energía solar, ya que deben operar en los mercados eléctricos diarios e intra-diarios, con el riesgo de sufrir penalizaciones si se desvían de la producción previamente fijada (Kraas et al., 2013).

En el caso de sistemas fotovoltaicos, la evaluación y el pronóstico se centran en la componente global de la radiación solar (GHI a partir de ahora), mientras que un sistema termosolar necesita conocer la evaluación y el pronóstico de la componente directa normal de la radiación (DNI de aquí en adelante). La DNI requiere de equipamientos muy específicos que precisan un mayor mantenimiento y por ello su medida es más escasa que la GHI. Su evaluación y pronóstico es más difícil que en el caso de la GHI, debido a su enorme sensibilidad a cambios en la nubosidad, propiedades ópticas de aerosoles y otras variables atmosféricas.

Estas dos componentes de la radiación solar están relacionadas entre sí, junto con la componente difusa, que es aquella radiación que llega a la superficie de la tierra después de haber sido dispersada por nubes, aerosoles u otros constituyentes atmosféricos. Así, la radiación global GHI es la suma de la radiación difusa y la proyección horizontal de la radiación directa normal.

2. Objetivo de la tesis

El objetivo de la tesis es desarrollar procedimientos optimizados para mejorar la evaluación del recurso solar a nivel diario y horario, generando estimaciones fiables tanto de GHI como de DNI en zonas geográficas extensas. Tales estimaciones pueden distribuirse como mapas de radiación o como series temporales en una localización concreta.

La principal dificultad para generar mapas de radiación de alta calidad radica en la escasez de estaciones de medida radiométricas. A pesar de la creciente importancia que se le está reconociendo al sector solar, aún son pocas las redes radiométricas si se comparan con las redes de medida de otras variables meteorológicas como la precipitación, la humedad relativa, etc… Si escaso es el número de estaciones que miden la radiación global GHI, aún menor es el número de estaciones que miden la DNI. El mayor coste de los aparatos de medida de radiación unido al coste de mantenimiento de dichos aparatos hace que se hayan tenido que desarrollar métodos alternativos para generar mapas de radiación.

Tradicionalmente, el objetivo de generar mapas de radiación solar se ha abordado a través de tres procedimientos bien diferenciados:

1) En una zona geográfica en la que se cuente con una red densa de estaciones radiométricas, basta con aplicar un simple método de interpolación espacial: ponderación por distancia, *kriging*, red de triángulos irregulares, etc… Se ha demostrado que con este método se generan mapas de calidad si la distancia entre las estaciones de medida es menor de 20-30 km (Zelenka et al., 1999).
2) Si la zona de estudio no cuenta con una red densa de estaciones radiométricas, pero sí de estaciones de medida de otras variables meteorológicas, se puede estimar la radiación solar a partir de esas variables más asequibles y luego aplicar uno de los métodos de interpolación espacial. Son muchas las relaciones que se han encontrado en décadas entre la radiación solar y otras variables como la temperatura, la duración del día, la precipitación, la humedad, la cubierta nubosa, la elevación y la latitud. Estas relaciones pueden agruparse en tres tipos: relaciones físicas, empíricas y semi-empíricas, siendo la ecuación de Ångström (una relación con las horas de luz diarias) la más utilizada durante años. Los mapas de radiación así elaborados son fiables, pero tienen el inconveniente de que el error de la estimación de la radiación se suma al error del posterior método de interpolación espacial, por lo que es conveniente un procedimiento aún más preciso.

3) El tercer procedimiento hace uso de datos derivados de imágenes de satélite, modelos meteorológicos numéricos o productos globales de reanálisis, que cubren todo el globo o áreas geográficas muy extensas, con una alta resolución espacial y temporal. La información contenida en esos mapas se procesa a través de modelos para transformarla en estimaciones de radiación solar en superficie.

En las últimas décadas, ha sido este tercer grupo de aproximaciones el que mayor desarrollo ha experimentado. Se han desarrollado y perfeccionado numerosos modelos de conversión de las radiancias observadas por los sensores de satélites y la radiación solar que alcanza la superficie de la tierra. Entre estos métodos podemos destacar el modelo SUNY (Perez et al., 2002), el Heliosat-2 (Rigollier et al., 2004), el método de DLR-SOLEMI (Schillings et al., 2004a) y sus variaciones. Todos ellos hacen uso de satélites de órbita geoestacionaria, de forma que proporcionan una imagen del globo de hasta 1 km de resolución espacial cada 15 minutos. A través de modelos físicos, empíricos o semi-empíricos se ha conseguido convertir la información de cada pixel en una estimación fiable de la radiación solar que alcanza esa región en su superficie.

La tesis se sitúa dentro de este grupo de modelos, podemos denominar *globales*, capaces de generar mapas de radiación para zonas extensas, con alta resolución espacial y temporal.

El objetivo principal de la tesis es diseñar, implementar y evaluar modelos optimizados para generar estimaciones diarias y horarias de GHI y de DNI, mejorando los resultados obtenidos con las técnicas utilizadas hasta el momento.

Dichos modelos deberán satisfacer los siguientes requisitos:

1) Estimar la GHI y la DNI diaria y horaria en puntos geográficos con independencia de que se tenga o no medidas de radiación en esa localización.
2) Generar mapas de radiación diarios y horarios, y no únicamente estimaciones de radiación en un punto geográfico.
3) Generar mapas horarios de cubierta nubosa, que posteriormente puedan utilizarse en sistemas de pronóstico de radiación de hasta las siguientes 6 horas (Perez et al., 2010a; Marquez and Coimbra, 2013).

4) Mejorar la precisión de las estimaciones de GHI y DNI respecto a las obtenidas con otros procedimientos, y disponer de dichas estimaciones prácticamente a tiempo real, con la única limitación de la disponibilidad temporal de las entradas del modelo.
5) Depender del menor número posible de variables exógenas, de forma que se puedan reproducir los resultados sin necesidad de disponer de fuentes de entrada complicadas o difícilmente disponibles a tiempo real. Ante resultados razonablemente parecidos, se elegirá siempre el modelo más sencillo que cuente con el menor número de entradas.

3. Metodología

Todos los modelos que se han diseñado e implementado en la tesis están basados en redes neuronales artificiales (ANN a partir de ahora). A partir de este tipo de metodología de inteligencia artificial, se van a construir varios modelos capaces de generar estimaciones de radiación solar usando diferentes variables meteorológicas o datos procedentes de satélite.

En las últimas décadas las ANNs se han utilizado en innumerables estudios de diferentes campos científicos, principalmente atraídos por su facilidad para encontrar relaciones no lineales entre variables, incluso en presencia de ruido en esas variables y sin necesidad de tener un conocimiento previo de la relación existente entre ellas.

En el campo concreto de radiación solar son muy abundantes los estudios con redes neuronales, tanto para su estimación espacial y temporal como para su pronóstico a corto, medio o largo plazo. Los estudios comparativos entre las ANNs y métodos tradicionales de regresión muestran que los resultados con redes son usualmente más eficientes (Reddy, 2003; Tymvios et al., 2005; Elminir et al., 2007; Jiang, 2009).

Las variaciones en la utilización de ANNs en trabajos de radiación solar son enormes. Se han utilizado para estimar radiación en numerosas localizaciones de diferentes latitudes y climas, tanto puntuales como mapas de radiación (p. ej., Arabia Saudí (Mohandes et al., 1998; Rehman and Mohandes, 2008), España (Hontoria et al., 2005; Lopez et al., 2005; Bosch et al., 2008; Siqueira et al., 2010), Turquía (Sozen, 2004b; Sozen et al., 2005; Şenkal and Kuleli, 2009; Şenkal, 2010), Grecia (Moustris et al., 2008), China (Lam et al., 2008), etc…), usando varias tipologías internas (p.ej. Mohandes et al., 2000; Dorvlo et al., 2002; Cao and Lin, 2008; Mubiru, 2008a; Siqueira et al., 2010), diferentes variables de entrada (geográficas and climatológicas, p.ej. Sozen, 2004a; Lopez et al., 2005; Rehman and Mohandes, 2008; Behrang et al., 2010; Rahimikhoob, 2010), o varias escalas de tiempo (mensual, diaria, horaria, p.ej. Bosch et al., 2008; Cao and Lin, 2008; Zervas et al., 2008; Behrang et al., 2010). Típicamente, estos modelos se han desarrollado para predecir la radiación solar a partir de datos medidos anteriores, para estimar valores en localizaciones donde no hay medidas de tierra, o para rellenar valores en series temporales de radiación (p.ej. Mohandes et al., 1998; Dorvlo et al., 2002; Cao and Cao, 2006; Hocaoglu et al., 2008; Mubiru, 2008b; Mellit and Pavan, 2010; Voyant et al., 2011).

Una red neuronal está caracterizada por su arquitectura, el algoritmo de entrenamiento utilizado y la función de activación de las neuronas ocultas. Todos los modelos de ANNs utilizados en la tesis parten de redes neuronales sencillas del tipo MLP –perceptrón multicapa– (García-Cuesta et al., 2008), con una capa de variables de entrada, una sola capa de neuronas ocultas y una capa de salida con una única variable de salida: la GHI o DNI horaria o diaria, o una variable directamente relacionada con ellas. El proceso de aprendizaje comienza asignando valores aleatorios a los pesos que conforman la ANN. A partir de ahí, se sigue un proceso iterativo de minimización del error de la predicción de la ANN en el conjunto de aprendizaje. Dicho proceso consiste en la modificación del valor de los pesos hasta alcanzar la condición de mínimo o se supere un determinado número de iteraciones.

Las redes MLP son el tipo de ANNs más utilizado, junto a un algoritmo de aprendizaje con retro-propagación. A su favor están la sencillez del modelo, su rápida convergencia al mínimo, y su reconocida capacidad de poder aproximar cualquier función con la precisión que se desee con una única capa oculta (Hornik et al., 1989; Leshno et al., 1993).

El mayor inconveniente es que la red MLP suele ser muy sensible a los pesos iniciales y con frecuencia el proceso de convergencia queda atrapado en un mínimo local, de forma que hay que complementar el modelo con algún otro procedimiento que asegure que alcanza la mejor de las soluciones posibles, y no un mínimo relativo que suele resultar poco preciso.

Otro inconveniente de este tipo de redes es el riesgo de que el proceso de aprendizaje sobreajuste la red, es decir, simule con gran precisión la variable de salida en el conjunto de entrenamiento, pero fracase a la hora de simular la variable de salida en un conjunto independiente.

Ambos inconvenientes pueden abordarse de diferentes formas, que explicamos e implementamos en los distintos capítulos de la tesis. Cada capítulo añade un nuevo paso a la metodología, con la finalidad de perfeccionar la capacidad de las ANNs para estimar con precisión y fiabilidad la radiación cuando los datos de entrada son totalmente independientes (temporal y/o espacialmente) a los de entrenamiento.

En resumen, el conjunto de datos de entrenamiento se divide en dos o tres subconjuntos, de los cuales uno de ellos, el subconjunto de calibración, está formado por el 70% aleatorio de todo el conjunto. Los pesos iniciales también se fijan al inicio de forma aleatoria. Una vez fijados, el algoritmo de retro-propagación alcanza con facilidad y rapidez el mínimo local. Si repetimos el proceso un número elevado de veces, es fácil observar que los resultados obtenidos por las diferentes ANNs al comparar las estimaciones de la red con datos medidos independientes varían, a veces significativamente. Hay dos motivos principales de fondo que justifican este resultado:

1) Al variar los pesos iniciales numerosas veces, el algoritmo de aprendizaje es capaz de 'caer' en un mínimo relativo mejor, más cercano al mínimo absoluto. De ahí que la red o redes que consigan valores de error más pequeños son mejores candidatas para formar parte del modelo de ANN para estimar la radiación.
2) Las ANNs son muy sensibles a la calidad de los datos de entrenamiento, de forma que al variar numerosas veces el conjunto de datos (cada vez un 70% distinto) se posibilita que la red se entrene con un subconjunto que presente menos ruido o represente mejor la realidad.

Es conocido que la robustez y fiabilidad de los resultados de una ANN se pueden mejorar a veces significativamente combinando apropiadamente varios modelos de redes en un ensamble de ANNs (Sharkey, 1996; Sharkey, 1999). Para que la solución combinada sea óptima, lo importante es que las redes individuales sean lo mejor posible y que las deficiencias de unas (peores resultados en un subconjunto de datos) se vean compensadas o corregidas por las otras. Cada red del conjunto debe ser, por tanto, precisa y diversa de las demás redes.

Con el procedimiento descrito anteriormente, se pueden construir numerosas redes optimizadas, que son buenas candidatas para hacer un combinado de redes también optimizado.

Un punto crítico a la hora de diseñar un modelo de redes neuronales es seleccionar el mejor conjunto de variables de entrada y la estructura óptima de la red. Son mayoría en la literatura los trabajos que hacen uso de un conocimiento *a priori* del fenómeno físico que se quiere modelizar, y fijan de antemano las variables de entrada. Con la misma frecuencia, el número de capas y de neuronas ocultas es fijado después de probar empíricamente varias posibilidades. Así hemos hecho en los capítulos 2, 3 y 4 de la tesis.

En los últimos años se han multiplicado los estudios en los cuales estos elementos constitutivos de las redes se fijan de forma automática y evolutiva. En concreto, con ANNs de tipo MLP, se han desarrollado muchos trabajos con algoritmos genéticos (GA) para optimizar los pesos, la arquitectura de la red o las reglas de aprendizaje, o simplemente para seleccionar óptimamente las variables de entrada (Yao, 1999; Castillo et al., 2000; Cook et al., 2000; Leung et al., 2003; Harpham et al., 2004; Shen and Fan, 2004; Palmes et al., 2005; Trevino and Falciani, 2006; Khazaee et al., 2008; Ding et al., 2011). En el campo de radiación solar, algunos ejemplos significativos de aplicación de redes neuronales evolutivas los encontramos p. ej. en (Kalogirou, 2004; Mellit, 2010; Mellit et al., 2010; Wang et al., 2011; Pedro and Coimbra, 2012; Chu et al., 2013; Mellit and Kalogirou, 2014). Otros trabajos también combinan con éxito GA y un modelo combinado de ANNs (Yao and Liu, 1998; Wang and Alhamdoosh, 2013; Chen et al., 2014).

En el último capítulo de la tesis proponemos un nuevo procedimiento de combinación de redes neuronales evolutivas. Dicho procedimiento es capaz de seleccionar con un algoritmo genético el mejor subconjunto de entradas entre 20 posibles variables candidatas, al mismo tiempo que selecciona un conjunto optimizado de redes neuronales cuya salida agregada resulta ser óptima.

4. Resumen de la tesis

El objetivo de diseñar, implementar y evaluar modelos optimizados de estimación de GHI y DNI ha sido abordado progresivamente. Cada capítulo de la tesis supone un paso adicional en este recorrido, añadiendo una mejora tanto en los objetivos conseguidos hasta ese momento como en la propia metodología.

Capítulo 1: "Generación de datos sintéticos de radiación solar basada en reanálisis ERA-Interim y redes neuronales artificiales"

El objetivo es generar estimaciones diarias de GHI a través de ANNs utilizando como datos de entrada principalmente algunas variables meteorológicas obtenidas de los reanálisis ERA-Interim del Centro Europeo de Previsiones Meteorológicas a Plazo Medio (ECMWF por sus siglas en inglés).

Esta base de datos es el resultado de un reanálisis de la atmósfera global, cubre el periodo de tiempo desde 1989 hasta el presente, y proporciona datos de numerosas variables meteorológicas. El modelo atmosférico que implementa y el sistema de reanálisis están configurados con 60 niveles verticales y una resolución espacial de 0.7º, generando datos cada 6 horas (Simmons et al., 2007).

Utilizar esta base de datos del ERA-Interim puede ser una buena alternativa al uso de imágenes de satélite. La resolución espacial y temporal es peor que en el caso de los satélites, pero tiene la ventaja de ser una base de datos homogénea desde 1989 (los datos de satélite desde 1989 necesitan una previa recalibración para ser comparados con datos actuales), no presenta huecos (a diferencia de las imágenes de satélite) y es fácilmente accesible (http://apps.ecmwf.int/datasets/data/interim-full-daily/). Además, como esta base de datos no genera directamente evaluación de radiación solar, el método propuesto en este capítulo proporciona a los investigadores que utilizan ERA-Interim una herramienta adicional para explotar aún más la información contenida en estos reanálisis.

La zona de estudio para evaluar el modelo ha sido Andalucía (España). Se han utilizado datos de 9 años de 83 estaciones radiométricas distribuidas por toda la región, 18 de las cuáles se han utilizado como subconjunto independiente de validación, el resto de entrenamiento.

Los datos de entrada de los modelos de ANNs han sido 4 variables de ERA-Interim (*total cloud cover, skin temperature, total column water vapour, total column ozone*) junto con la latitud y longitud de cada estación, el día del año y un modelo de cielo despejado.

Como modelo definitivo se ha seleccionado una única ANN, que genera estimaciones diarias de GHI con un 16,4% de RMSE y un coeficiente de correlación del 94%. Los resultados son similares a los reportados en la literatura a escala diaria. Esta red es capaz de generar estimaciones fiables para cualquier localización de Andalucía, con una resolución espacial de 1km.

Capítulo 2: "Ensamble de redes neuronales artificiales para estimar la radiación global a partir de imágenes de satélite Meteosat"

El objetivo es generar estimaciones diarias de GHI a través de imágenes de satélite. Se trata de comparar los resultados de la metodología propuesta con los resultados obtenidos con el modelo anterior a partir del ERA-Interim y con los resultados obtenidos en la literatura.

La novedad del modelo reside en la utilización de todos los canales de 3 km de resolución espacial del satélite Meteosat, de la segunda generación de satélites (MSG) de EUMETSAT. Los modelos de conversión de satélite a radiación en superficie suelen utilizar exclusivamente los canales visibles de satélite. En este estudio, explotamos toda la información contenida también en los canales infrarrojos, que proporcionan datos significativos sobre las nubes, vapor de agua y otros constituyentes atmosféricos.

El área de estudio es la misma que en el capítulo anterior: 83 estaciones dispersadas por toda Andalucía. La evaluación se ha centrado en datos del año 2008. Las variables de entrada utilizadas han sido los 11 canales del satélite Meteosat más un modelo de cielo despejado. El modelo de ANN definitivo es un ensamble de las cinco mejores ANNs de las 1000 construidas. Las estimaciones diarias generadas presentan un 6.74% de RMSE global, y un coeficiente de correlación del 99%. El modelo es capaz de generar estimaciones fiables en toda Andalucía, con la misma resolución espacial que las imágenes de satélite (unos 4.5 km en estas latitudes). La mayor resolución espacial y temporal de los datos de entrada (satélite) respecto a los del estudio anterior (ERA-Interim) se manifiesta en una notable mejoría en las estimaciones.

Capítulo 3: "Método avanzado basado en redes neuronales para estimar radiación solar horaria a partir de imágenes multi-espectrales de MSG"

El objetivo es generar estimaciones horarias de GHI para cualquier localización dentro de un área muy extensa, que incluye latitudes desde 22.79ºN (Tamanrasset, Algeria) a 58.25ºN (Toravere, Estonia) y longitudes desde 16.50ºW (Tenerife) hasta 34.78ºE (Sede Boqer, Israel).

Para entrenar y evaluar el modelo se han utilizado datos de 3 años (2009-2011) de GHI horaria de 28 estaciones radiométricas, 7 de las cuales se han utilizado para calibración. Se han utilizado como datos de entrada imágenes del satélite Meteosat-9 del mismo periodo de tiempo, haciendo uso de sus 11 canales, además de un modelo de cielo despejado.

La mayor precisión requerida por los objetivos (resolución temporal horaria y fiabilidad en la extrapolación espacial sobre un área muy extensa), requiere mejoras en la optimización de los modelos de ANNs. Para el modelo ensamble de ANNs se han construido numerosas redes diversas entre sí y generadas de forma complementaria. Así, se han generado dos modelos ensamble independientes: uno con las diez mejores redes entrenadas con todo el conjunto de entrenamiento, y otro modelo formado por tres redes, cada una entrenada para distintas condiciones de cielo. El modelo definitivo resulta ser una combinación de los dos modelos anteriores, beneficiándose en parte de la información complementaria contenida en ambos.

Las estimaciones horarias de GHI obtenidas del modelo definitivo presentan un RMSE del 13.5% en las estaciones de evaluación independiente, lo que supone una mejora del 21.5% respecto del modelo Heliosat-2, uno de los métodos más utilizados de estimación de radiación a partir de imágenes de satélite. El modelo es aplicable sobre cualquier localización dentro de la extensa área de estudio, partiendo de cualquier imagen de satélite MSG. De hecho, el modelo es utilizado actualmente a tiempo real dentro del grupo MATRAS (Modelización de la Atmósfera y Radiación Solar) de la Universidad de Jaén.

Capítulo 4: "Ensamble de redes neuronales artificiales evolutivas para estimar DNI horaria a partir de imágenes de Meteosat"

El objetivo es generar estimaciones horarias de DNI para cualquier localización dentro de un área muy extensa, que incluye latitudes desde 22.79ºN (Tamanrasset, Algeria) a 58.25ºN (Toravere, Estonia) y longitudes desde 16.50ºW (Tenerife) hasta 34.78ºE (Sede Boqer, Israel).

El área de estudio y la resolución temporal de las estimaciones generadas son las mismas que en el estudio anterior. La principal novedad es utilizar todos los canales de Meteosat para estimar directamente la DNI. Ésta presenta muchas más dificultades para ser estimada que en el caso de la GHI, principalmente porque el número de estaciones en las que se mide esta variable es muy bajo, y porque su variabilidad temporal y espacial es notablemente mayor, siendo especialmente sensible al paso de las nubes y a varios constituyentes atmosféricos, especialmente a los aerosoles.

Los métodos tradicionales para estimar la DNI pasan en su mayoría por calcular en primer lugar la GHI y luego aplicar un modelo de descomposición de la GHI en sus componentes. Un inconveniente es que el error de la estimación de la GHI se suma al error del método de descomposición, por lo que los errores de las estimaciones de DNI suelen ser altos y tienen un amplio margen de mejora.

Algunos de los modelos de conversión de satélite a irradiancias, además de estimar la GHI estiman también directamente la DNI. Otros, primero calculan la GHI y operacionalmente estiman la DNI con uno de los modelos GHI-DNI antes mencionados. El modelo propuesto en este estudio genera estimaciones de DNI directamente de la información contenida en los canales visibles e infrarrojos del satélite Meteosat-9.

El proceso de optimización de las ANNs debe ser más preciso que en estudios anteriores, dada la variabilidad de la magnitud que se desea modelar. En este caso, se ha diseñado un algoritmo evolutivo capaz de seleccionar las mejores entradas posibles entre 20 candidatas, al mismo tiempo que genera un conjunto de redes optimizadas para generar una estimación agregada que sea óptima.

El modelo definitivo genera estimaciones horarias de DNI para cualquier localización dentro de los límites del área de estudio, con un RMSE global del 24.29%, lo que supone una mejora del 35% respecto de las estimaciones obtenidas por los métodos de referencia actuales.

CHAPTER 2

GENERATION OF SYNTHETIC DAILY GLOBAL SOLAR RADIATION DATA BASED ON ERA-INTERIM REANALYSES AND ARTIFICIAL NEURAL NETWORKS

A. Linares-Rodríguez, J.A. Ruiz-Arias, D. Pozo-Vázquez, J. Tovar-Pescador. Generation of synthetic daily global solar radiation data based on era-interim reanalysis and artificial neural networks. Energy, 36 (8) (2011), pp. 5356–5365; doi:10.1016/j.energy.2011.06.044

ABSTRACT

Four variables (total cloud cover, skin temperature, total column water vapour and total column ozone) from meteorological reanalysis were used to generate synthetic daily global solar radiation via artificial neural network (ANN) techniques. The goal of our study was to predict solar radiation values in locations without ground measurements, by using the reanalysis data as an alternative to the use of satellite imagery. The model was validated in Andalusia (Spain), using measured data for nine years from 83 ground stations spread over the region. The geographical location (latitude, longitude), the day of the year, the daily clear sky global radiation, and the four meteorological variables were used as input data, while the daily global solar radiation was the only output of the ANN. Sixty five ground stations were used as training dataset and eighteen stations as independent dataset. The optimum network architecture yielded a root mean square error of 16.4% and a correlation coefficient of 94% for the testing stations. Furthermore, we have successfully tested the forecasting capability of the model with measured radiation values at a later time. These results demonstrate the generalization capability of this approach over unseen data and its ability to produce accurate estimates and forecasts.

CHAPTER 2

GENERATION OF SYNTHETIC DAILY GLOBAL SOLAR RADIATION DATA BASED ON ERA-INTERIM REANALYSES AND ARTIFICIAL NEURAL NETWORKS

1. Introduction

Solar radiation is a required variable for the designers of solar systems. It is often provided as solar radiation maps, which is usually a preferable approach, more efficient and easy to handle. In order to build them, many procedures have been proposed. Most of them require knowing the solar radiation at many points spread wide across the region of interest. In addition, empirical, semi-empirical, physical, neural networks, wavelets, fractals, etc. techniques must be assumed for the spatial prediction.

Unfortunately, solar radiation is still a scarcely sampled variable with respect to other environmental variables as temperature or precipitation, and there is usually a small set of stations with available radiation measurements. This lack of information has been often avoided with satellite imagery (Perez et al., 1997; Perez et al., 2002; Rubio et al., 2005; Şenkal, 2010; Lu et al., 2011).

The method we propose in this study consists in the combination of meteorological reanalyses and artificial intelligence techniques for spatial prediction. It involves a new approach given that these reanalysis do not provide direct information on downward shortwave solar flux. Therefore, this work describe a new form of exploitation of this meteorological dataset and a valid alternative to the use of satellite imagery.

Artificial neural networks (ANN) have been used in diverse applications in control, robotics, pattern recognition, forecasting, medicine, power systems, manufacturing, optimisation, signal processing, and social/psychological sciences. They are particularly useful in system modelling, such as in implementing complex mapping and system identification.

In the last years, neural network methods have been employed for the prediction of global solar radiation both in time and space. Comparative studies of ANNs and traditional regression approaches have been achieved (Reddy, 2003; Tymvios et al., 2005; Elminir et al., 2007; Jiang, 2009), and it has been shown that ANN models are usually more efficient and less time consuming in modelling complex systems. A clear review of ANN applications for renewable energy systems has been reported by Kalogirous (Kalogirou, 2000; Kalogirou, 2001), and Mellit et al. (Mellit and Kalogirou, 2008) for photovoltaic systems.

ANNs have been used in solar radiation modelling works for locations with different latitudes and climates (e.g., Saudi Arabia (Mohandes et al., 1998; Rehman and Mohandes, 2008), Spain (Hontoria et al., 2005; Lopez et al., 2005; Bosch et al., 2008; Siqueira et al., 2010), Turkey (Sozen, 2004b; Sozen et al., 2005; Şenkal and Kuleli, 2009; Şenkal, 2010), Greece (Moustris et al., 2008), China (Lam et al., 2008)), using various internal topologies (e.g. (Mohandes et al., 2000; Dorvlo et al., 2002; Cao and Lin, 2008; Mubiru, 2008a; Siqueira et al., 2010)), different input variables (geographical and climatological, e.g. (Sozen, 2004a; Lopez et al., 2005; Rehman and Mohandes, 2008; Behrang et al., 2010; Rahimikhoob, 2010)), or several time scales (monthly, daily and hourly, e.g. (Bosch et al., 2008; Cao and Lin, 2008; Zervas et al., 2008; Behrang et al., 2010)). Typically, these models were devised to forecast solar radiation (from ground data from earlier time), to estimate values at unsampled locations, or to remove/fill data gaps (e.g. (Mohandes et al., 1998; Dorvlo et al., 2002; Cao and Cao, 2006; Hocaoglu et al., 2008; Mubiru, 2008b; Mellit and Pavan, 2010; Voyant et al., 2011)).

In this work, ANNs with different topologies have been developed for spatial and time prediction of daily global solar radiation in Andalusia (Spain), using measured values at 83 ground stations over the region.

2. Methodology

First, we trained the ANN with measured data at the 65 training stations from 1999/10/01 to 2008/12/31. Following, we tested the results against the measurements at the 18 testing stations. Finally, we also used the ANN to predict the period 2009/01/01-2009/09/30, which is out of the training period.

2.1. Artificial Neural Network architecture

An ANN is characterized by its architecture, training or learning algorithm and activation function. The architecture describes the connections between the neurons. It consists of an input layer, an output layer and generally, one or more hidden layers in-between as depicted in Fig. 1.

The architecture used in this work, shown in Fig. 1, has an input layer with eight inputs, one hidden layer with 25 neurons and a sigmoidal activation function, φ , defined by the logistic function: $\varphi = 1/(1+\exp(-x))$, x being the corresponding input.

For the output layer, a linear activation function ψ was used in the implementation.

The approximating function $\hat{G}$, representing daily global solar radiation, was defined as

$$\hat{G}(\vec{x}) = \psi\left(\sum_{i=1}^{N} y_i \cdot w_2(i) + b_2\right) \qquad \text{(Eq. 1)}$$

where

$$y_i(\vec{x}) = \varphi\left(\sum_{j=1}^{M} x_j \cdot w_1(j,i) + b_1(i)\right) \qquad \text{(Eq. 2)}$$

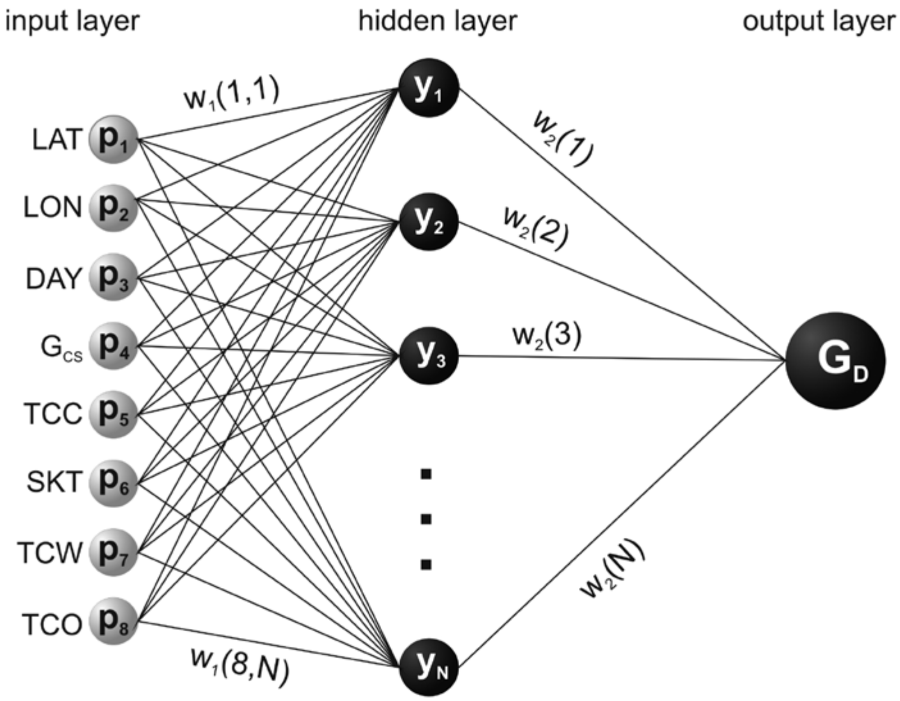

Figure 1. Multilayer perceptron feed-forward neural network used in the study.

For the training process of the ANN, a Bayesian regulation backpropagation algorithm was used. This algorithm is a supervised iterative training method that updates the weights and bias values according to Levenberg-Marquardt optimization (Foresee and Hagan, 1997b). It minimizes a linear combination of squared errors and weights, and then uses Bayesian regularization to determine the correct combination that results in a network that generalizes satisfactorily.

The number of hidden neurons in an ANN is a function of the problem's complexity, the number of input and output parameters, and the number of training cases available. A trial and error process was used to determine the number of hidden neurons. After trying a number of different configurations, and repeating each training process ten times to avoid random errors, it was found that 25 neurons in the hidden layer yielded the best results with a reasonable computational effort.

Before selecting this ANN model (multilayer perceptron feed-forward neural network), we conducted several trials with different networks and architectures, particularly radial basis function neural networks and some sort of ensemble networks. We found no significant improvement in the results, but higher computational cost.

2.2. Selection of ANN input variables

As shown in Fig. 1, the variables selected as ANN inputs were geographical latitude and longitude, day of the year, clear-sky daily radiation, and four variables from ERA-Interim dataset: total cloud cover, skin temperature, total column water vapour and total column ozone. Following, we provide a detailed description of these variables.

2.2.1. Latitude, longitude, day of the year

The first two ANN input variables were geographical variables of the ground stations: latitude and longitude. They would allow us to spatially extrapolate to the entire study region. Altitude of each station was not included as input variable because it was inserted into the clear sky model (section 2.2.2). The third ANN input variable was the day of the year, and it takes into account the seasonal trend.

2.2.2. Clear sky solar radiation model

Daily clear sky global solar radiation plays an important role as input variable because it incorporates the atmospheric optical mass and, consequently the altitude (Batlles et al., 2008; Ruiz-Arias et al., 2009). Other meteorological variables, especially cloud data, were introduced as input variables to take into account all sky conditions.

We used the clear sky model of the European Solar Radiation Atlas (ESRA) (Rigollier et al., 2000), which is based on the turbidity coefficient of Linke. Particularly, this parameter accounts for the climatic aerosols. We used representative averages of monthly Linke turbidity factors for the study region.

The calculations were conducted with the module *r.sun* of the GRASS GIS platform, which also includes additional routines to account for the terrain influence (Hofierka and Súri, 2004). The terrain was modelized with the

SRTMv3 digital elevation model (DEM) (Jarvis et al., 2006) upscaled to 30 arc seconds (approximately 1 km at the study region latitudes).

The grid of this DEM (a 418x788 matrix for the region of our study) was used as support for the subsequent interpolations.

2.2.3. Meteorological reanalyses

The meteorological variables used as inputs in the ANN model were obtained from the ECMWF ERA-Interim dataset (*http://data.ecmwf.int*). It is a reanalysis of the global atmosphere covering the data-rich period since 1989, and continuing in real time. The ERA-Interim data assimilation system contains many improvements both in the forecasting model and analysis methodology relative to ECMWF's previous reanalysis, ERA-40, including the use of 4-dimensional variational analysis, a revised humidity analysis, the use of variational bias correction for satellite data, and other improvements in data handling (Simmons et al., 2007).

The atmospheric model and reanalysis system is configured with 60 levels in the vertical (the top level at 0.1 hPa), a grid spacing of 0.7º (Gaussian grid N128) and data every six hours. However, we retrieved the dataset from the server interpolated at 0.25ºx0.25º (roughly 25 km of grid spacing at the study site latitudes).

ERA-Interim products are already used extensively at ECMWF for research and diagnostic studies, and for many other purposes such as developing the seasonal forecasting system, and providing climatology for operational verification. Reanalysis products are used increasingly in many fields that require an observational record of the state of either the atmosphere or its underlying land and ocean surfaces.

2.2.4. Selection of climatological variables

Among the variety of instantaneous surface and single level parameters saved on the model's Gaussian grid, we selected the following ones:

- TCC: total cloud cover (0-1)
- SKT: skin temperature (K) (i.e. surface temperature)
- TCW: total column water vapour (kg m^{-2})

- TCO: total column ozone (kg m^{-2})

As expected, the most important variable in the performance of the ANN was TCC. The other variables has been used in the literature as input variables for a variety of models (empirical, neural networks, etc. (Mellit and Kalogirou, 2008)), and they also improve the accuracy of this model.

The data cover the period from October 1999 to October 2009. Moreover, the ERA-Interim reanalysis is available in near real time.

2.2.5. Daily averaging

The ERA-Interim data assimilation system produces four analyses per day, at 00, 06, 12 and 18 UTC. In order to obtain a single daily value for each variable, we averaged these four analyses for each day. To take into account the different hourly influence on radiation, we integrated the four values by a weighted sum, according with equation (3) (as variable we have considered TCC, but the same equation was used for the others variables: SKT, TCW and TCO):

$$TCC_{day} = \sum_{k=1}^{4} w_k \cdot TCC_k \qquad \text{(Eq. 3)}$$

where the weights w_k are:

$$w_k = G_{cs,k} \Big/ \sum_{k=1}^{4} G_{cs,k} \qquad \text{(Eq. 4)}$$

The subscript *k* indicates the *k*th time-step (k=1 corresponds to 00 UTC, k=2 to 06 UTC, and so on). Thus, the higher the clear sky radiation ($G_{cs,k}$), the greater the weight of that value. With this method, for instance, the cloudness at 00 UTC is neglected when averaging the TCC over the whole day, because, obviously, it has no influence in the daily global solar radiation.

2.3. ANN output variable

Daily global solar radiation was selected as the only output of the model. Training and testing of the network continued until no improvement in the output was achieved (i.e. minimum error between ANN output values and measured data) or after a predetermined number of epochs, which was set at 1000. In this case, minimum error was achieved before maximum epoch had been reached.

3. Study region and experimental dataset

The study was carried out throughout the region of Andalusia, in the southern part of the Iberian Peninsula, between latitudes 37º and 42º N (Fig. 2). The region comprises the southern-most part of the European continent, in the western facade of the Mediterranean basin. It covers an extension of about 87,000 km^2 with 917 km of coastlines. The region is located in the transition zone from temperate to warm climates. Geographically, Andalusia is in a key region to play an important strategic role in the implementation of renewable energy technology in Europe, as well as providing sufficient energy for its own needs and even exporting such projects to other countries (Ramos Ridao et al., 2007). It is worth mentioning that Spain has the greatest amount of available sunshine of any country in Europe and has a very abundant solar resource (1200–1800 kWh m^{-2} year^{-1}). Furthermore, Spain is one of the largest manufacturers in the world of solar power technology.

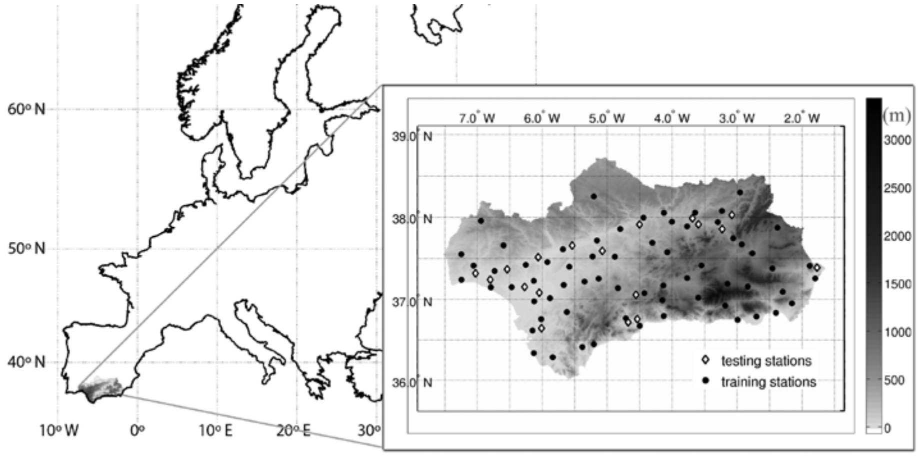

Figure 2. Region of study. The highlighted region shows the digital model of terrain (DEM) used.

3.1. Measured daily global solar radiation data

The Andalusian Regional Office of Agriculture and Fishing records the daily global solar radiation on horizontal surface by means of two different networks: the Alert and Phytosanitary Information Network, with 86 stations, and the Agroclimatic Network, with 102 stations. Data are measured with Kipp & Zonen CM-5 pyranometers. An instrumental error of 5% is expected in the best case. However, despite the stations are regularly maintained and calibrated, typically, it is more realistic to assume a 7%. The networks were deployed to provide information of, mainly, agroclimatical interest. Therefore, the radiometric stations are clustered around the principal agricultural areas of the region. The range of elevations above mean sea level goes from 4 m to 1212 m, with a mean elevation of 345 m. The selected period ranges from 1999/10/01 to 2009/09/30. Due to the long time period used in our work, the number of stations with available data was largely reduced.

3.2. Quality control

The purpose of the data quality control was to eliminate spurious data and inaccurate or inconsistent measurements, caused by cosine response error of the pyranometers, large calibration drifts and other malfunctions.

First, a quality assessment based on physical limits was applied: an upper limit of 0.8 for the atmospheric clearness, calculated as the daily measured solar radiation to the daily potential extraterrestrial, and a lower limit of 0.01 MJm^{-2} Following, the data were undergone to a visual inspection and 14 of the stations were ruled out since they presented suspicious trends. Overall, excluded values did not reach the 2%.

After this quality control procedure, 83 candidate stations remained. However, the stations tend to be clustered around flat areas which, from the methodological point of view, might lead to wrong results by overweighting the areas with higher density of stations. Therefore, 18 of these stations (60,768 records) were carefully extracted, and reserved for independent validation of the results, trying to homogenize the spatial distribution of the stations. The remaining 65 stations were used for training the ANN (219,439 records). Fig. 2 shows the distribution of the training and validation datasets along the study region.

4. Results and discussions

Validation of the results was carried out by using the following statistical scores: mean bias error (MBE), root mean square error (RMSE), relative mean square error (rRMSE) and correlation coefficient (R) between the predicted and the measured values of daily global radiation for training and testing datasets. Where

$$MBE = \frac{1}{n}\sum_{s=1}^{n} G_s - \hat{G}_s \qquad \text{(Eq. 5)}$$

$$RMSE = \sqrt{\sum_{s=1}^{n}\left(G_s - \hat{G}_s\right)^2 \Big/ n} \qquad \text{(Eq. 6)}$$

$$rRMSE = RMSE * 100 / \overline{G} \qquad \text{(Eq. 7)}$$

$$R = \sqrt{\sum\left(\hat{G}_s - \overline{G}\right)^2 \Big/ \sum\left(G_s - \overline{G}\right)^2} \qquad \text{(Eq. 8)}$$

n being the number of input/output patterns.

4.1. Prediction of daily global solar radiation

After successfully trained with data from 1999/10/01 to 2008/12/31, the ANN was ready to perform prediction with new input data. In order to judge its performance, we tested it using the independent dataset. A comparison between the results for training and testing dataset gives us an estimation of the ANN's spatial extrapolating capability. Table 1 shows the error values of the ANN model.

Table 1
Error values of the ANN model

	MBE	**RMSE**		
	MJ·m^{-2}	MJ·m^{-2}	%[a]	R
65 training stations (219,439 values)	-4.11e-07	2.59	14.29	0.95
18 testing stations (60,768 values)	-0.47	2.88	16.41	0.94
all stations (280,207 values)	-0.10	2.65	14.75	0.95

[a] percentages of the mean measured daily global solar radiation value

Fig. 3 shows a comparison between measured and predicted data a) at Baena training station, and b) at Jerez testing station.

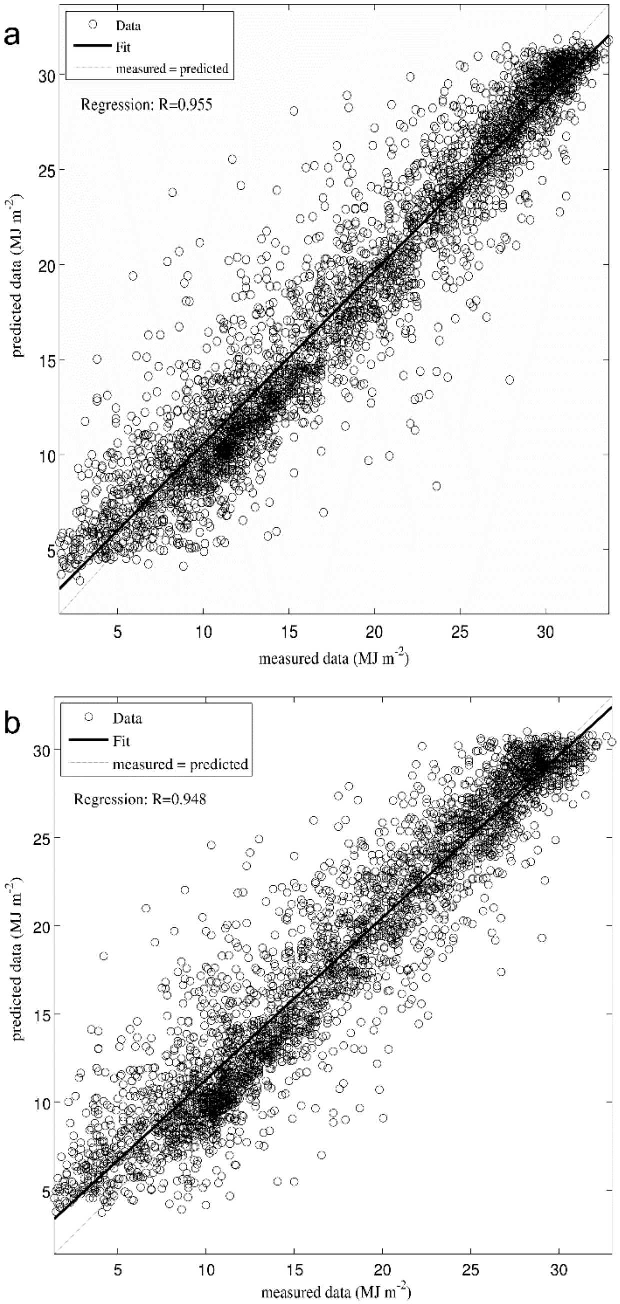

Figure 3. A comparison between measured and predicted data a) at Baena training station, and b) at Jerez testing station.

A first result, as shown in Table 1, was that the estimation of global solar radiation performs with an acceptable accuracy using ECMWF ERA interim dataset. Taking into account the scale of our study area, it's worth noting that the MBE and RMSE values were better or similar to others reported in the literature, and also compared with satellite-derived irradiance models (Perez et al., 2002).

For testing stations, the overall RMSE was found to increase from 14.29% (training stations) to 16.41%. RMSE per each testing station varied from 13.94% to 21.42%. The last one was obtained for the easternmost station and, hence, the station with a greatest relative distance to the whole set of training stations. This result could be explained by the significant dependence of the accuracy with the distance between stations.

4.2. Yearly and seasonal dependence

To further explore the performance of the ANN model, we built nine ANN models, one for each year from 2000 to 2008. Each annual-ANN was trained only with data within a year, e.g. ANN_2002 was trained with data from 2002/01/01 to 2002/12/31. The structure of each annual-ANN was exactly the same than the original ANN. The results for the testing dataset –in terms of MBE and RMSE– are shown in Fig. 4.

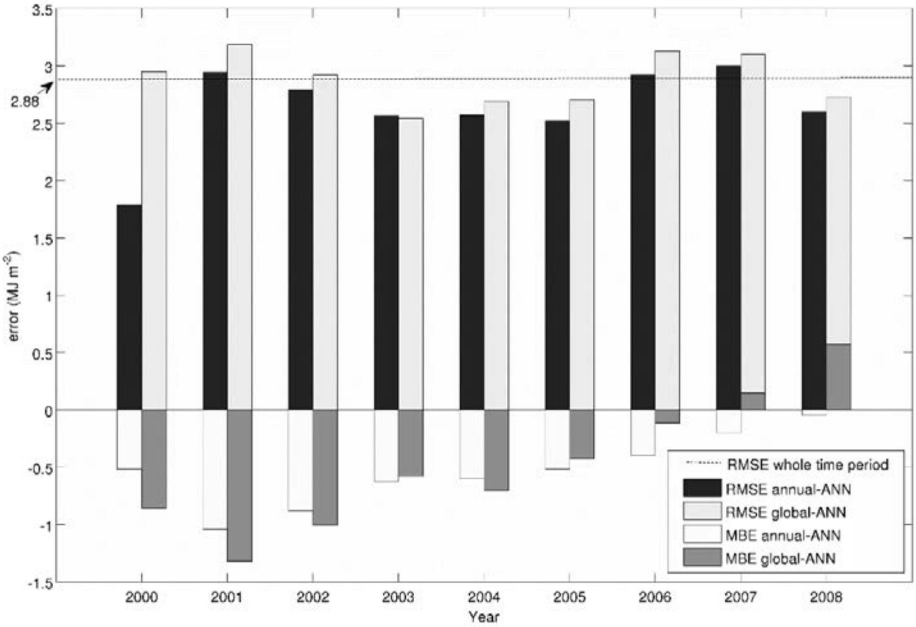

Figure 4 Comparison between results of the ANN trained with the whole dataset (global-ANN) and the ones trained only with data of a year (annual-ANN), focused on the testing dataset.

Overall, the ANN trained with the whole dataset generated worse G_D estimates for every single year than its corresponding annual-ANN model. Each annual-ANN was able to fit the data better for a year, and the climatic differences between years led to a loss of accuracy over the whole time period. On the other hand, each annual model lacked generalization and only generated accurate estimates for the trained year.

In order to use the model to predict G_D for future time periods, ANN should be trained with the whole dataset, because it takes into account all climatic trends over a decade.

We also conducted a monthly evaluation of the ANN along the whole time period, and concluded that the worst estimates were obtained in winter (RMSE=24.52% in December) and the best in summer (8.27% in July). In Andalusia, summer is usually sunny and dry, and winter is cloudy and rainy. Despite using the four meteorological variables from ERA-Interim to train the ANN, and more specifically total cloud fraction (TCC), the model is very sensitive to the presence of clouds. Therefore, we evaluated the ANN model by TCC values (ranged from 0 to 1), dividing dataset into ten subsets according to the TCC value. The results are shown in Table 2:

Table 2
Error values of the ANN model, grouped by TCC values

ANN trained with the whole dataset (from 1999/10/01 to 2008/12/31)										
	training dataset					**testing dataset**				
TCC * 10	number of inputs/outputs	**MBE** MJ·m^{-2}	**RMSE** MJ·m^{-2}	**RMSE** %	R	number of inputs/outputs	**MBE** MJ·m^{-2}	**RMSE** MJ·m^{-2}	**RMSE** %	R
[0,1)	99681 (45.4%)	-0.0083	1.77	7.97	0.97	27963 (46%)	-0.70	2.10	9.81	0.96
[1,2)	14953 (6.8%)	-0.0075	2.52	13.06	0.94	3933 (6.5%)	-0.67	2.88	15.48	0.92
[2,3)	10939 (5%)	0.058	2.76	15.34	0.92	2858 (4.7%)	-0.45	3.18	18.27	0.89
[3,4)	10531 (4.8%)	0.080	2.99	17.61	0.90	2807 (4.6%)	-0.41	3.35	20.48	0.88
[4,5)	11474 (5.2%)	0.017	3.13	19.68	0.89	3098 (5.1%)	-0.29	3.47	22.63	0.87
[5,6)	12100 (5.5%)	-0.050	3.20	20.98	0.88	3349 (5.5%)	-0.28	3.45	22.97	0.85
[6,7)	10694 (4.9%)	-0.038	3.27	22.38	0.88	3052 (5%)	-0.13	3.60	24.89	0.84
[7,8)	9279 (4.2%)	-0.0061	3.35	24.18	0.87	2594 (4.3%)	-0.12	3.61	26.52	0.85
[8,9)	10320 (4.7%)	-0.021	3.51	27.02	0.85	2905 (4.8%)	-0.070	3.66	28.49	0.84
[9,10]	29468 (13.4%)	0.018	3.19	30.88	0.85	8209 (13.5%)	-0.14	3.43	34.10	0.82

As expected, ANN led to highly accurate estimates in clear sky days (9.81% over 46% of the whole dataset), but lost accuracy in cloudy days. It's worth noting that both RMSE and rRMSE presents a well-defined trend, which can be used as an error estimate of the ANN, using the TCC value. Consequently, we fitted the rRMSE (Fig. 5) against TCC (we have used 20 TCC subsets to improve accuracy). The model used for the empirical error is depicted in the figure.

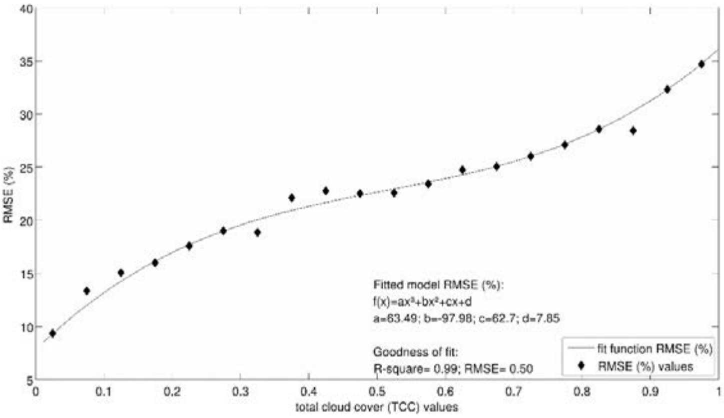

Figure 5 Fitted models for RMSE of the ANN based on TCC values

4.3. Solar radiation maps

Daily global solar radiation maps were generated using the annual-ANN models.

For a given day, a 418x788 matrix for each variable (latitude, longitude, day of the year, daily clear sky global radiation, and four ERA-Interim variables) was used as input variable. Hence, a 418x788 matrix with G_D estimates was generated as output of the model, covering the whole area of Andalusian with a spatial resolution of 30 arc seconds.

Fig. 6 shows a sample of solar radiation maps and its corresponding input maps:

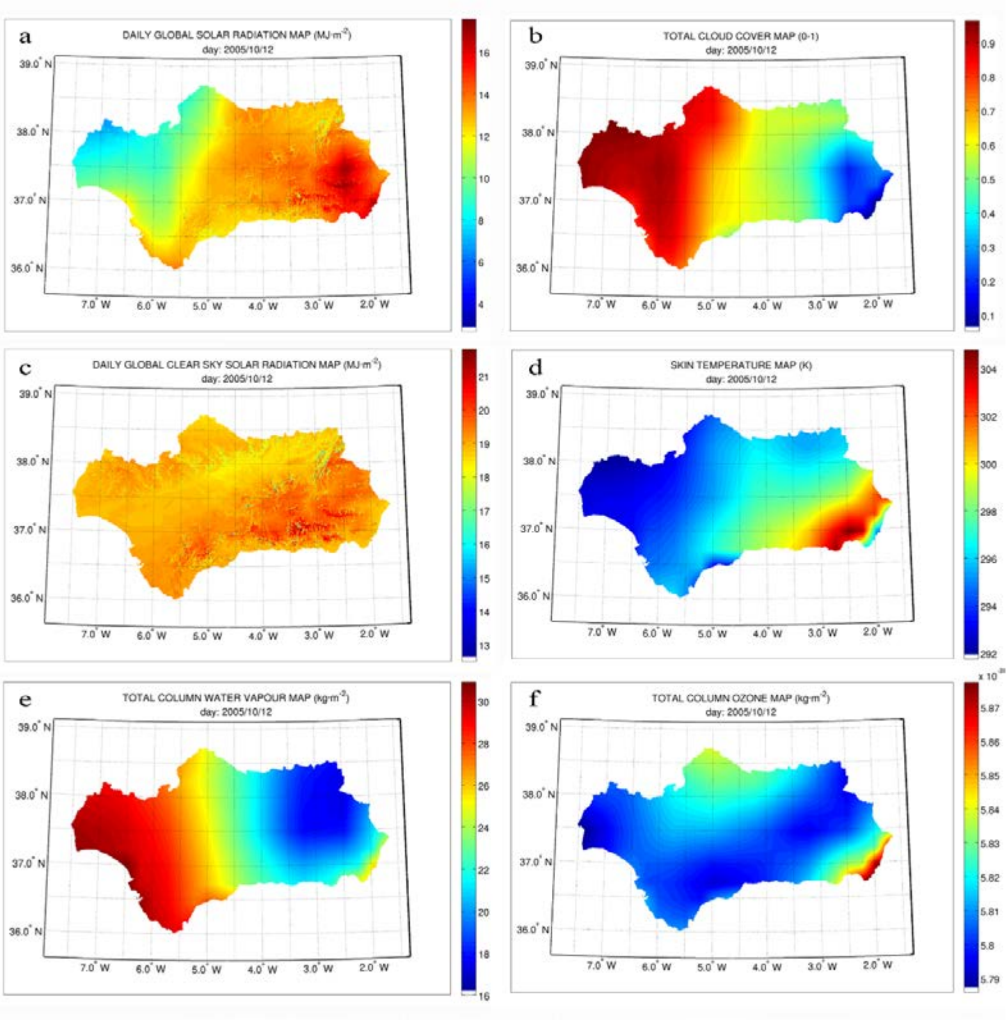

Figure 6. a) daily global solar radiation map generated by ANN model. Next figures show input matrixes for each input variable of the ANN: b) TCC values, c) global clear sky values, d) SKT values, e) TCW values and f) TCO values from ECMWF dataset.

4.4. Forecasting capability

The ANN trained with data from 1999/10/01 to 2008/12/31 was tested with data from 2009/01/01 to 2009/09/30 to evaluate the forecasting capability of the model. The results are shown in Table 3. It's to be noted that the ANN even yields accurate estimates for future time period. It proves that ANN has successfully learnt the complex relationship between input variables and solar radiation, and it can be used to predict G_D for any location within the study region, as there are input data for the entire region, even for future periods.

Fig. 7 shows a comparison between predicted and measured data at one training station (a) and at one testing station (b).

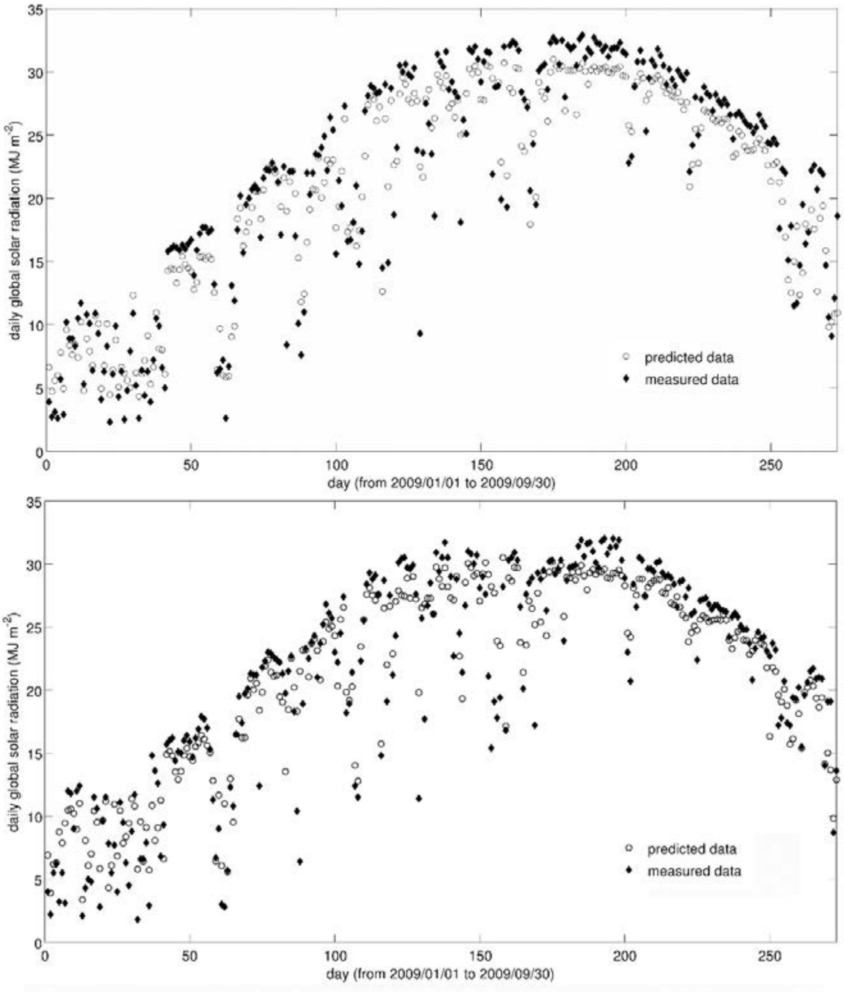

Figure 7. Comparison between measured and predicted data a) for Jaen station (training station n. 42) and b) for Jerez station (testing station n. 2).

Table 3
Forecasting capability of the model. Error values of the ANN model, for data from 2009/01/01 to 2009/09/30

	MBE	**RMSE**		**R**
	MJ·m^{-2}	MJ·m^{-2}	%	
65 training stations (17745 values)	0.14	2.83	13.52	0.94
18 testing stations (4914 values)	0.49	3.02	14.20	0.93
all stations (22659 values)	0.22	2.87	13.67	0.94

These results were a bit better than ones obtained in section 4.1. because the available time period didn't include some of more cloudy months (october-december 2009).

5. Conclusions

The model for generation of synthetic series of solar radiation via ANN presented a good performance, demonstrating the viability of the methodology for generating daily global solar radiation in localities were there only exists meteorological information from ERA Interim reanalysis. RMSE ranged from 13.94% to 21.42%.

Spatial prediction of ANN estimates demonstrates to be distance dependent. If only a few stations are used for training the ANN, or these stations do not cover the whole area of study, the results can't be extrapolated for a long distance. Therefore, solar maps could be generated with a reasonable accuracy only if many stations spread over the study region are available.

Furthermore, ANN model is heavily dependent on presence of clouds. In order to improve the model, further research should be carried out to incorporate, for instance, more detailed cloud information.

Once trained the ANN, its forecasting capability has been evaluated by predicting G_D values for the first nine months of 2009, with a relative RMSE between ANN estimates and observed values ranged from 13.52% (for training stations) to 14.20% (for testing stations).

Acknowledgments

This work was supported by the Spanish Ministry of Science and Technology (Project ENE2007-67849-C02-01) and the Andalusian Ministry of Science and Technology (Project P07-RNM-02872). The data were kindly provided by the regional office of Agriculture and Fishing of Andalusia.

CHAPTER 3

AN ARTIFICIAL NEURAL NETWORK ENSEMBLE MODEL FOR ESTIMATING GLOBAL SOLAR RADIATION FROM METEOSAT SATELLITE IMAGES

A. Linares-Rodríguez, J.A. Ruiz-Arias, D. Pozo-Vázquez, J. Tovar-Pescador. An artificial neural network ensemble model for estimating global solar radiation from Meteosat satellite images." Energy 61 (2013), pp. 636-645; doi:10.1016/j.energy.2013.09.008

ABSTRACT

An optimized artificial neural network ensemble model is built to estimate daily global solar radiation over large areas. The model uses clear-sky estimates and satellite images as input variables. Unlike most studies using satellite imagery based on visible channels, our model also exploits all information within infrared channels of the Meteosat 9 satellite. A genetic algorithm is used to optimize selection of model inputs, for which twelve are selected – eleven 3-km Meteosat 9 channels and one clear-sky term. The model is validated in Andalusia (Spain) from January 2008 through December 2008. Measured data from 83 stations across the region are used, 65 for training and 18 independent ones for testing the model. At the latter stations, the ensemble model yields an overall root mean square error of 6.74% and correlation coefficient of 99%; the generated estimates are relatively accurate and errors spatially uniform. The model yields reliable results even on cloudy days, improving on current models based on satellite imagery.

CHAPTER 3

AN ARTIFICIAL NEURAL NETWORK ENSEMBLE MODEL FOR ESTIMATING GLOBAL SOLAR RADIATION FROM METEOSAT SATELLITE IMAGES

1. Introduction

Despite an abundance of studies for estimating solar radiation over large areas, a major challenge remains to more accurately generate estimates at high spatial and temporal resolution. A well-distributed network of ground solar radiation stations is usually needed to ensure an accurate and reliable interpolation method. However, this is not always possible in many regions, since solar radiation is still rarely sampled compared to other environmental variables.

Traditionally, the issue of spatial estimation of solar radiation has been addressed by three types of scheme:

First, when there are many available solar radiation values, widely dispersed across a study area, simple interpolation methods (nearest-neighbour, inverse distance-weighted, kriging, and others) may give good spatial estimates (e.g., (Alsamamra et al., 2009; Ruiz-Arias et al., 2009; Ruiz-Arias et al., 2011b)).

Second, in the case of a coarser ground station network, radiation may be estimated using other meteorological variables more commonly available in a study area. Numerous relationships have been discovered between radiation at the earth surface and several variables (e.g., sunshine duration, temperature, precipitation, humidity, cloud cover, elevation, and latitude). These relationships can be grouped into physical, empirical and semi-empirical approaches, with Ångström's equation (a relationship with sunshine duration) perhaps the most commonly used in recent decades. These methods produce reliable results, but they depend on availability of other meteorological variables and, to attain spatial estimates over a region, there must be some method of further interpolation. Therefore, the accuracy of radiation maps continues to depend on the density of meteorological measurements.

The third type of scheme has been the use of global meteorological or climatological datasets derived from satellite imagery, numerical models or reanalysis products, which cover the entire globe or extensive areas. They may provide continuous time series of data at pixels, with high spatial and temporal resolutions. Among these methods, satellite imagery has been more frequently exploited in recent decades, taking advantage of the high spatiotemporal resolution of geostationary satellites. This makes satellite approaches the best option for constructing accurate maps, especially over large areas.

Satellite-derived irradiances can be calculated from each image every 15 minutes, with as much as ~1-km spatial resolution in some regions. In general, satellite count-to-irradiance models can be grouped into physical and empirical models, but hybrid models are the most extensively used. These models take advantage of both the former two types. That is, they have the robustness of a physical approach (usually based on radiative transfer models that explicitly describe scattering and absorption processes operating in the earth-atmosphere system), but simplify certain equations with empirical regressions. There have been extensive reviews of these models (Noia et al., 1993a; Noia et al., 1993b; Pinker et al., 1995). Among the most used, we refer to Heliosat method (Cano et al., 1986; Rigollier et al., 2004; Zarzalejo et al., 2009) and Perez model (Perez et al., 1997; Ineichen and Perez, 1999; Perez et al., 2002; Cebecauer, 2010; Perez et al., 2010b) and their variations, some of which combine both model types. Although they retain some degree of fitting to observations, their physical underpinnings guarantee suitability for generalization.

It has been shown that these satellite-based approaches generate more accurate solar radiation estimates than classical interpolation methods, at locations outside the vicinity of a ground station (Zelenka et al., 1992; Perez et al., 1997; Zelenka et al., 1999). Examples of solar radiation maps built with satellite data are found in (Janjai et al., 2005; Janjai et al., 2011).

In a previous work (Linares-Rodriguez et al., 2011), we proposed a novel method within the third type of scheme. It estimates daily solar radiation at unobserved locations, using reanalysis data from ECMWF (European Centre for Medium-Range Weather Forecasts) (Simmons et al., 2007) as an alternative to satellite imagery. Despite the use of coarse spatial-resolution ERA (ECMWF Reanalysis)-Interim data (0.7º, about 70 km in the study region (Simmons et al., 2007)), the method produced valid estimates of daily radiation, even better on a monthly basis.

The aim of this work is to design a new method for spatial estimation of daily solar irradiation via artificial neural networks and satellite-derived irradiances, toward improving results in the current literature on daily global solar radiation (e.g., RMSE (root mean square error) between 9% and 16% on a daily basis, as cited in Rigollier et al., 2004; Benghanem et al., 2009; Lu et at., 2011).

Two main improvements are achieved herein: 1) An optimization procedure of an ANN (artificial neural network) ensemble model, and 2) use of additional information contained in Meteosat channels other than the two visible ones, which are the most used in these methods.

In recent years, ANN models have received increased scientific attention as a method for estimating solar radiation across large areas. These models for deriving solar radiation through ANNs use a variety of meteorological variables as inputs. It has been shown that ANN models outperform traditional regression approaches (Reddy, 2003; Tymvios et al., 2005; Elminir et al., 2007; Jiang, 2009), and hence have been used in numerous papers (see a brief review in Linares-Rodriguez et al., 2011). We refer to Kalogirou's reviews of ANN applications for renewable energy systems (Kalogirou, 2000; Kalogirou, 2001), and Mellit et al. (Mellit and Kalogirou, 2008) for photovoltaic systems. All these can be classified as empirical approaches, within the second type of scheme explained above.

In recent years, there have also been some works in global solar radiation estimation using ANNs and satellite data (e.g., for monthly (Şenkal, 2010), daily (Lu et al., 2011), and hourly (Zarzalejo, 2005) estimates). Usually, in these types of methods, satellite visible channels are used for model inputs. Only a few studies have used other satellite channels. Perez et al. (2010b) suggested a method to improve the performance of satellite-to-irradiance models using satellite infrared sensors. Lu et al. (2011) used instead all channels of a Multifunctional Transport Satellite of the Japan Meteorological Agency for daily global solar estimation, in an effort to fully exploit information contained in both visible and infrared channels. They achieved estimates with RMSE around 20%.

In our study, Meteosat all-channel observations and a clear sky model were used as ANN inputs. The extra information from infrared channels significantly improves the derivation of solar radiation and yields more accurate estimates, outperforming other physical or semi-empirical approaches.

The remainder of the paper is organized as follows. The ”Region and data” section describes the study area and data, with special reference to Meteosat images. Detailed description of the method is provided in the following section, including neural network architecture and input selection. The ”Results and Discussion” section deals with assessment of various ANN models. Finally, conclusions are given.

2. Region and data

2.1. Region of study and ground measurement dataset

The study region is Andalusia, which covers about 87,000 km^2 in the southern Iberian Peninsula. The experimental dataset is the same used in a previous work (Linares-Rodriguez et al., 2011). Here, we consider data from the year 2008. We used 83 solar radiation ground stations across the region. The stations are owned and maintained by the Andalusian regional government, and are part of the Agricultural and Environmental monitoring network. Two different pyranometers are used in this network: CMP3 (Kipp & Zonen), and SP1110 from Campbell Scientific (manufactured by Skye Instruments). Overall, an instrumental error about 5% can be assumed (Alsamamra et al., 2009; Ruiz-Arias et al., 2011b).

Daily solar radiation values were carefully filtered to eliminate spurious data, and inaccurate or inconsistent measurements (Polo et al., 2006). Several quality control procedures were performed at this stage. Particularly, a quality assessment based upon physical limits was applied: an upper limit of 0.8 for the atmospheric clearness, calculated as the daily measured solar radiation to the daily potential extraterrestrial, and a lower limit of 0.01 MJ/m^2 (Iqbal, 1983).

As a first step, 65 stations were selected for the training dataset, and the remaining 18 were used as an independent testing dataset. Figure 1 shows the distribution of the training and validation stations within the study region. Next, 133 suspicious data were eliminated from the training dataset. Ultimately, 23,592 daily global solar radiation values were used as the training dataset, and 6,570 as the testing dataset, corresponding to daily horizontal global solar irradiation observations from 2008/01/01 to 2008/12/31 at 65 training stations (23,592 = 65 stations x 365 days – 133 suspicious data) and 18 testing stations (6,570 = 18 stations x 365 days).

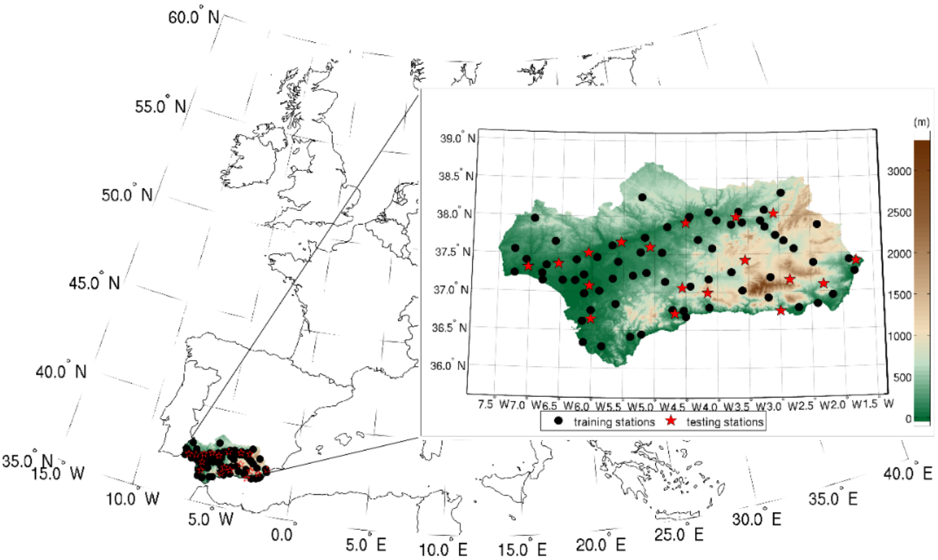

Figure 1 Study region. Highlighted region shows digital model of terrain (DEM) used.

2.2. Meteosat dataset

2.2.1. Meteosat Second Generation (MSG) satellite series

The MSG satellite series, with its Spinning Enhanced Visible and Infrared Imager (SEVIRI), scans the complete disk of the earth four times per hour and has 12 spectral channels. These are three solar channels (0.6, 0.8 and 1.6 µm), eight infrared channels (3.9, 6.2, 7.3, 8.7, 9.7, 10.8, 12.0 and 13.4 µm), and one high-resolution broadband visible channel (0.3–0.7 µm). The nadir spatial resolution of SEVIRI is 1×1 km^2 for the high-resolution channel, and 3×3 km^2 for all other channels (EUMETSAT, 2005; EUMETSAT, 2008). Raw data are internally managed via a radiometric process, in four main steps (EUMETSAT, 2005): a) linearization, b) conversion into radiances, c) calibration, and d) linear scaling. The last step ensures that the necessary dynamic range falls into the available interval [0, 1023], through two linear coefficients: "Cal_Slope" and "Cal_Offset". Both are constants provided for each image by the satellite sensors. Finally, effective radiances for each channel are fully defined by the relationship (EUMETSAT, 2007a; EUMETSAT, 2007b; EUMETSAT, 2008):

$$\textit{effective radiances} = \textit{Cal\_Offset} + (\textit{Cal\_Slope} \times \textit{Pixel Count}), \qquad \text{(Eq. 1)}$$

We only considered the first eleven Meteosat-9 channels, with 3-km nadir spatial resolution (approximately 4.5 km at study area latitudes). For these channels, a complete image, that is, the full disk of the earth, nominally consists of 3712 x 3712 pixels. The potential information contained in each channel may be summarized as follows (Schmetz et al., 2002):

- Channels 1–2 (VIS0.6 and VIS0.8): These are the visible channels, essential for cloud detection, cloud tracking, scene identification, aerosol, and land surface and vegetation monitoring.
- Channel 3 (NIR1.6): It can discriminate between snow and cloud, ice and water clouds, and provides aerosol information.
- Channel 4 (IR3.9): Primarily for low cloud and fog detection. Also supports measurement of land and sea surface temperature at night, and increases low-level wind coverage from cloud tracking. For MSG, the spectral band has been broadened to longer wavelengths for improving signal-to-noise ratio.
- Channels 5–6 (WV6.2 and WV7.3): Channel for observing water vapor and winds. Enhanced to two channels peaking at different levels in the troposphere. Also supports height allocation of semitransparent clouds.
- Channel 7 (IR8.7): Provides quantitative information on thin cirrus clouds and supports discrimination between ice and water clouds.
- Channel 8 (IR9.7): Ozone radiances may be used as input to numerical weather prediction. Temporal evolution of the total ozone field can also be monitored.
- Channels 9–10 (IR10.8 and IR12.0): Well-known, split-window channels. Essential for measuring sea and land surface and cloud-top temperatures.
- Channel 11 (IR13.4): The CO_2 absorption channel. In cloud-free areas, it may contribute temperature information from the lower troposphere that can be used for estimating static instability.

2.2.2. Effective radiance dataset

Meteosat satellite products are available online via the EOP (Earth Observation Portal) from the website of the EUMETSAT (European Organisation for the Exploitation of Meteorological Satellites) (*https://eoportal.eumetsat.int*). The EUMETSAT Data Centre provides a long-term archive of data and generated products from EUMETSAT, which can be ordered online. Before ordering products, users have to be registered in the EOP and signed up for the Data Centre service.

Among the collections of satellite product types from the various EUMETSAT-operated satellites, the EUMETSAT archive supplies images and derived meteorological products from geostationary Meteosat satellites since 1981, which are positioned over Europe as well as the Indian Ocean.

Meteosat 9 High Rate SEVIRI Level 1.5 images from 2008/01/01 to 2008/12/31 were collected in HDF5 format, and all data mining were performed within the Matlab environment. We used the *nctoolbox* library, (*http://code.google.com/p/nctoolbox/*), a Matlab toolbox that provides read-only access to common data model datasets and allows to access many file formats and services using the same API.

Each satellite image was trimmed to the study region. Then, pixels containing ground station locations were selected and effective radiances calculated via Eq. (1), for each pixel every 15 minutes in 2008. Some missing values (a small percentage, <1%) were filled by Meteosat-8 images, or by interpolating previous/next values. Daily effective radiances were obtained by summing all values each day.

Finally, radiances at each station location were arranged in matrix form, for use as ANN candidate inputs: 11 channels x 23592 radiance values for training, and 11 x 6570 values for testing.

3. Methodology

3.1. ANN design

An ANN is characterized by its architecture, training or learning algorithm, and its activation function. The ANN models constructed here are of the MLP (multilayer perceptron) type. Architecture of the ANN models used (a visual scheme is shown in Fig. 2) consists of the following: An input layer with twelve inputs (M=12, the eleven Meteosat channels plus a clear-sky term); one hidden layer with twenty-five neurons (N=25); and an activation function φ, defined by the hyperbolic tangent function $\varphi = \tanh(x) = (\exp(2x)$

–1)/(exp(2x) + 1), x being the corresponding input. According to this function, inputs are standardized to the range [–1,1]. For the output layer, a linear activation function ψ was used in the implementation.

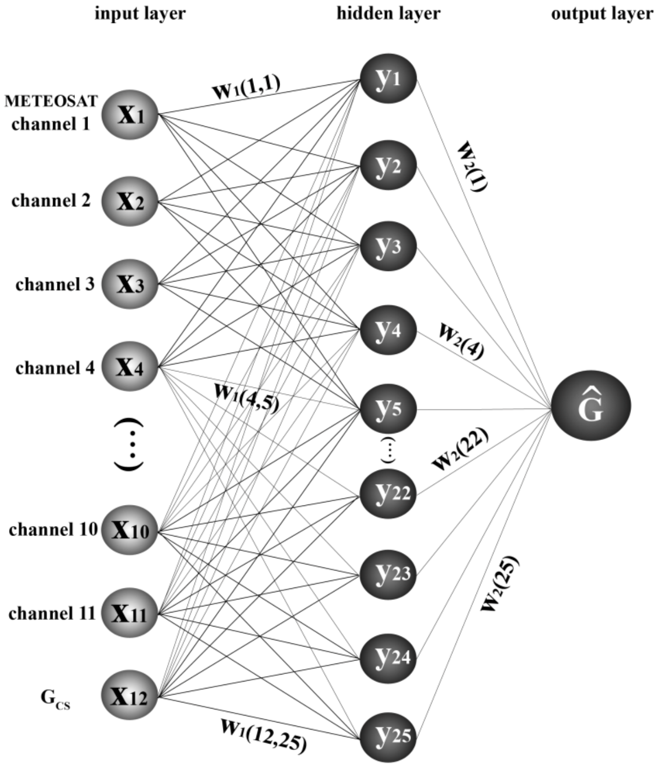

Figure 2 Multilayer perceptron, feed-forward neural network.

The approximating function $\hat{G}$, representing daily global solar radiation, was defined as

$$\widehat{G}(\vec{x}) = \psi\left(\sum_{i=1}^{N} y_i \cdot w_2(i) + b_2\right) \tag{Eq. 2}$$

where

$$y_i(\vec{x}) = \phi\left(\sum_{j=1}^{M} x_j \cdot w_1(j,i) + b_1(i)\right) \tag{Eq. 3}$$

(see Nomenclature for symbol definitions).

In order to improve the generalization capabilities of the ANN models, there are two widely used training methods known as early stopping and Bayesian regularization (Bishop, 1995). The former method requires a validation set besides the calibration and test sets. The latter method, which is used here, minimizes the over-fitting problem by taking into account the goodness-of-fit as well as the network architecture.

The Matlab Neural Network Toolbox was used for the implementation of the ANNs. For the training of the neural networks, the algorithm ‘trainbr’ was used. The algorithm is a supervised iterative training method that updates weights and bias values according to Levenberg-Marquardt optimization (Linares-Rodriguez et al., 2011). It minimizes a linear combination of squared errors and weights, via gradient descent with a momentum algorithm suitable to avoid falling to a local minimum (Hagan et al., 1996). It then uses Bayesian regularization to determine the correct combination of errors and weights, resulting in a network that generalizes satisfactorily (MacKay, 1992; Foresee and Hagan, 1997a; Dorvlo et al., 2002). Moreover, the training function ‘trainbr’ also minimizes the number of effective network parameters (weights and biases) used by the network.

The number of hidden neurons in an ANN is a function of problem complexity, number of input and output parameters, and number of available training cases. A trial-and-error process determines the number of hidden neurons. It is common in environmental modelling to seek a more parsimonious model, with the smallest number of inputs and parameters possible, to avoid over-parameterisation problems. After trying a number of different configurations, we found that the best architecture contained twenty-five hidden neurons.

Daily global solar radiation was selected as the only model output. Training and testing of the network continued until there was no improvement in output (i.e., minimum square error between ANN output values and measured data) or after a predetermined number of epochs, set to 500. In this case, minimum error was achieved before reaching the maximum epoch.

3.2. Selection of inputs

One of the more critical steps in ANN modelling is selection of an appropriate set of input variables (Lopez et al., 2005; Behrang et al., 2010; Koca et al., 2011). If relevant inputs are omitted, the model is unable to capture the desired input-output relationships. On the other hand, too many inputs can produce over-parameterization problems, as cited above. Usually, a set of candidate input variables is found via *a priori* knowledge of the system being modelled.

In this work, the candidate inputs were a clear-sky solar radiation estimate and the eleven 3-km Meteosat channels. These satellite observations provide useful information of scattering, absorption and reflection processes affecting solar radiation passing through the atmosphere.

3.2.1. Clear-sky solar radiation model

We used the clear-sky model of the ESRA (European Solar Radiation Atlas) (Rigollier et al., 2000), which is based on the turbidity coefficient of Linke. In particular, this parameter accounts for climatic aerosols. Daily clear-sky global solar radiation plays an important role as an input variable because it incorporates seasonal dependence, atmospheric optical mass and consequently altitude (Batlles et al., 2008; Ruiz-Arias et al., 2009). We used representative averages of monthly Linke turbidity factors for the study region. Calculations were similar to the previous work (Linares-Rodriguez et al., 2011). It has been shown (Ineichen, 2006) that ESRA clear sky model yields accurate estimates, with an overall RMSE of about 5% on daily basis.

3.2.2. Optimized input combination

Each of the twelve ANN inputs seems a priori to contain relevant information regarding solar radiation. In cases of more input variables, a selection method to rule out any of them should be conducted, as the Bayesian method called automatic relevance determination (Lopez et al., 2005; Bosch et al., 2008; Yacef et al., 2012). It has been shown that irrelevant variables can deteriorate the model performance (Yacef et al., 2012).

In our study, we conducted a simpler method to determine the best combination of inputs. We executed a multivariate variable selection procedure. Although the expected input-output relationship should show nonlinearity, this procedure may give some idea of the existence of negligible inputs. We used the *glmulti* R package for selection of the best input combination (Calcagno and de Mazancourt, 2010). Whether a candidate input is rejected by *glmulti* algorithm would mean that variable input contains superfluous or redundant information.

From the list of the explanatory variables, i.e., the clear-sky solar radiation term and eleven Meteosat channels, the function *glmulti* builds all possible unique combinations involving these variables. It explores the candidate set with a genetic algorithm (GA), which can readily find optimum combinations without fitting all possible models, and ranks candidate combinations according to an information criterion. This is the AIC (Akaike information criterion) in the present work (Akaike, 1974).

By exploring only a subset of all possible models, randomly but with a bias towards better models thanks to selection, it makes computation much faster. Genetic algorithms are very efficient at exploring highly discrete state spaces, and have been used successfully in related optimization problems. The GA procedure starts from a random population of models and evolves good local solutions by mimicking the process of natural selection using mechanisms such as higher rate of replication of the more effective variable subsets (chromosomes), mutation to generate variants and crossover to improve combinations (Goldberg, 1989; Trevino and Falciani, 2006).

After algorithm convergence, there are two combinations with lowest AIC scores. The first is built with all the Meteosat channels and clear- sky term, and the second with all possible inputs except channel 7, which is the term with lowest relative importance. Table 1 shows all relative importances of terms, computed as the sum of relative evidence weights of all possible combinations in which the term appears. Despite similar AIC scores of the two best input combinations, the *glmulti* algorithm gives a very different relative weight to each candidate. Ranked relative evidence weights of the models are computed as exp(ΔAIC/2), where ΔAIC is the difference of AIC between a model and the best model. These weights are normalized so that their sum is one; they can be interpreted as probabilities of each model being the best in the set (Calcagno and de Mazancourt, 2010). The relative weight computed for the first combination (all possible inputs) is 90.3%, against 9.70% for the other combination (all inputs except channel 7). Hence, the best combination was one built with all possible candidate inputs, i.e., with no input neglected.

Table 1
Relative importance of terms

channel7	0.9029585
channel4	0.9999977
channel2	0.9999999
channel1	1.0000000
channel3	1.0000000
channel5	1.0000000
channel6	1.0000000
channel8	1.0000000
channel9	1.0000000
channel10	1.0000000
channel11	1.0000000
G_{cs}	1.0000000

3.3. Model optimization procedures

3.3.1. Data division

A common practice in ANN modelling to guarantee its generalization capability (i.e., a model should yield reliable estimates outside the range of trained data) is to separate input data into appropriate calibration and validation sets. The ANN is trained only with the first dataset and the last is used to validate performance of a trained ANN. We use this splitting method for the training dataset (23,592 input/output patterns), according to the proportions 75% and 25% for calibration and validation sets, respectively.

Another independent set was selected outside the training dataset (6,570 input/output patterns from independent ground stations dataset) to verify that the network correctly learned the relationship between inputs and outputs, so could therefore be used to generate reliable global solar radiation estimates at ”untrained” locations.

3.3.2. Monte Carlo simulations

The calibration and validation subsets of the training dataset were sampled randomly. ANN weights and biases were also initialized randomly. To attain robustness in the model and prevent randomness problems, we followed a procedure similar to Monte Carlo simulations and repeated the overall ANN model development 1000 times, leaving parameter initialization and data division as random. We selected the first five ANNs that achieved optimum results as ANN ensemble model inputs (see next subsection).

This procedure represents a computationally expensive effort but, once the resulting ANN has been successfully trained and selected, solar radiation estimates are obtained immediately and training is no longer needed.

There are two major assumptions behind this procedure: (1) By varying the initial parameters, the training algorithm is enabled to search other parts of the parameter space, increasing overall chances of finding a global error minimum; (2) since measured data are affected by noise and an ANN is too sensitive to calibration data quality, a cleaner choice of training dataset should better reflect real relationships between inputs and output, thereby obtaining more reliable results.

3.3.3. ANN ensemble model

It has been shown (e.g. (Sharkey, 1999)) that the robustness and reliability of an ANN can be often significantly improved by appropriately combining several ANN models into an ANN ensemble. The construction of such an ensemble requires two main steps. The first is to create individual ensemble members, and the second is to find the appropriate combination of outputs from those members for producing the unique ensemble output.

Here, we compare results of the five best models selected in the previous stage with outputs of an ANN-E (ensemble model) built with those five individual ANN models. Ensemble output was constructed by averaging the five individual ANN outputs.

4. Results and discussion

Results were validated using the following statistical scores: MBE (mean bias error), RMSE, rRMSE (relative root mean square error) and correlation coefficient (R), between predicted and measured values of daily global radiation for training and testing datasets:

$$MBE = \frac{1}{n}\sum_{d=1}^{n}(G_d - \widehat{G}_d) \qquad \text{(Eq. 4)}$$

$$RMSE = \sqrt{\sum_{d=1}^{n}\left(G_d - \widehat{G}_d\right)^2 \Big/ n} \qquad \text{(Eq. 5)}$$

$$rRMSE = RMSE * 100 / \overline{G} \qquad \text{(Eq. 6)}$$

$$R = \sqrt{\sum\left(\widehat{G}_s - \overline{G}\right)^2 \Big/ \sum\left(G_s - \overline{G}\right)^2}\ , \qquad \text{(Eq. 7)}$$

where *n* is the number of input/output patterns.

4.1. Estimation of daily global solar radiation

As explained in the previous section, the ANN training procedure was repeated 1000 times and the best five models selected. Statistical scores of the results are shown in Table 2.

Table 2

Error values of the ANN models.

ANN-Model	Training period			Independent period		
	MBE (MJ/m²)	RMSE (MJ/m²)	R	MBE (MJ/m²)	RMSE (MJ/m²)	R
ANN-2008[a]	−4.2E−005	2.2603 (12.16%)	0.96	−0.0684	2.5796 (13.84%)	0.95
ANN-1	0.0066	1.2535 (6.73%)	0.99	−0.0296	1.2646 (6.83%)	0.99
ANN-2	0.0241	1.2619 (6.78%)	0.99	−0.0232	1.2573 (6.79%)	0.99
ANN-3	−0.0014	1.2527 (6.73%)	0.99	−0.0339	1.2688 (6.85%)	0.99
ANN-4	8.00E−004	1.2530 (6.73%)	0.99	−0.0491	1.2709 (6.87%)	0.99
ANN-5	−0.028	1.2503 (6.72%)	0.99	−0.0386	1.2633 (6.82%)	0.99
ANN-E	**0.0055**	**1.2364 (6.64%)**	**0.99**	**−0.0349**	**1.2473 (6.74%)**	**0.99**

Bold values correspond to ensemble model, which is the selected model.

[a] ANN reference model used in a previous work (Linares-Rodriguez et al., 2011), built with ERA-Interim reanalysis data from European Centre for Medium-Range Weather Forecasts.

According to Table 2, of the five best models, the ANN-E model yields the most accurate daily global solar radiation estimates. MBE and RMSE values are better than those reported in the literature for a daily basis (see Introduction section), and are near the assumed experimental/instrumental error of 5% (Estévez et al., 2011; Ruiz-Arias et al., 2011b). The low MBE values suggest the ANN-E model to be unbiased, although the model slightly overestimates solar radiation relative to the independent dataset (negative values).

The new ANN-E model outperforms the previous ANN-2008 model (Linares-Rodriguez et al., 2011), which was used in the present work as a benchmark. In that work, we built an ANN model with eight inputs: geographical latitude and longitude of the ground stations, day of the year, clear-sky daily radiation, and four meteorological variables from ERA-Interim dataset (Simmons et al., 2007): total cloud cover, skin temperature, total column water vapour and total column ozone. The model was trained and validated with measured data from the same experimental dataset of this study, and for year 2008 yielded estimates with an overall RMSE of 13.84% for the testing stations, as depicted in table 2.

The improvement of ANN-E against that ANN-2008 model was expected, since the most relevant input variables to ANN-2008 were derived from ERA-Interim analysis, with original spatial resolution 70 km. Spatial resolution of the Meteosat imagery is about 4.5 km in the study region. Figure 3 shows a scatter plot between measured and predicted solar radiation values at the independent set of stations.

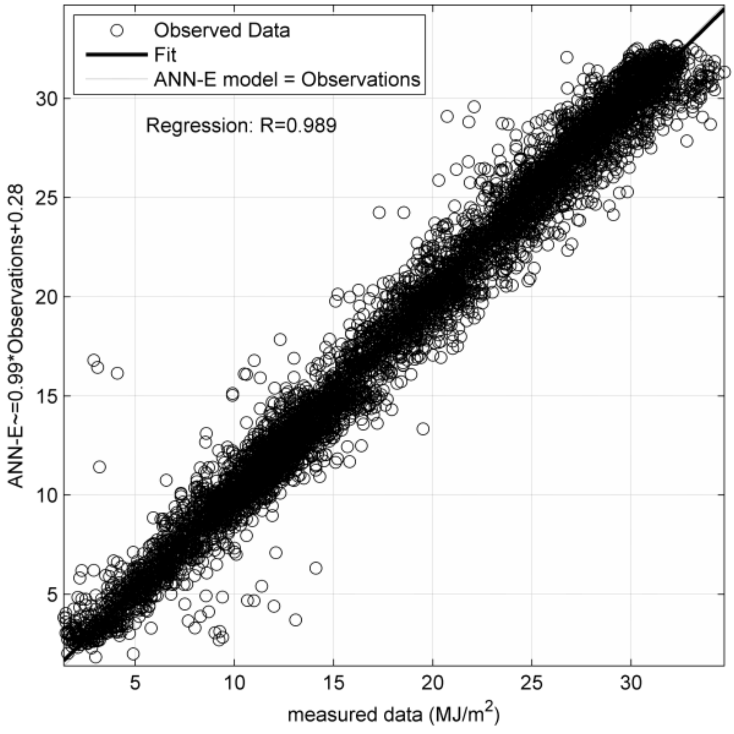

Figure 3. Scatterplot of ANN-E predicted solar radiation values against measured data at testing stations

The favourable results from the ANN-E model validate the initial premise of a real relationship between surface solar radiation and satellite radiances. Once the ANN is trained, the model can predict solar radiation values for any location in the study region, and for any day within the training period. Estimates outside these ranges are not reliable. The model can be used, for example, for filling missing daily solar radiation values at ground stations, and for predicting solar radiation at unobserved locations. The latter represents a spatial interpolation method and approach for generating accurate solar radiation maps. The ANN model even works with missing values from a given day, a great advantage compared to other interpolation techniques such as kriging, which always requires real values.

To certify the spatial interpolation capability of the ANN-E model, we checked the accuracy of estimates at each station. Figures 4 and 5 show statistical scores of radiation estimates at each of the ground training and independent stations, respectively. Nearly all the stations have relative RMSE values between 4–9%. A boxplot (Figure 6) shows overall scores. Within each box, the central mark is the median of all the error values, and box edges denote the 25th and 75th percentiles. Whiskers extend to the most extreme data points not considered outliers, and outliers are plotted individually.

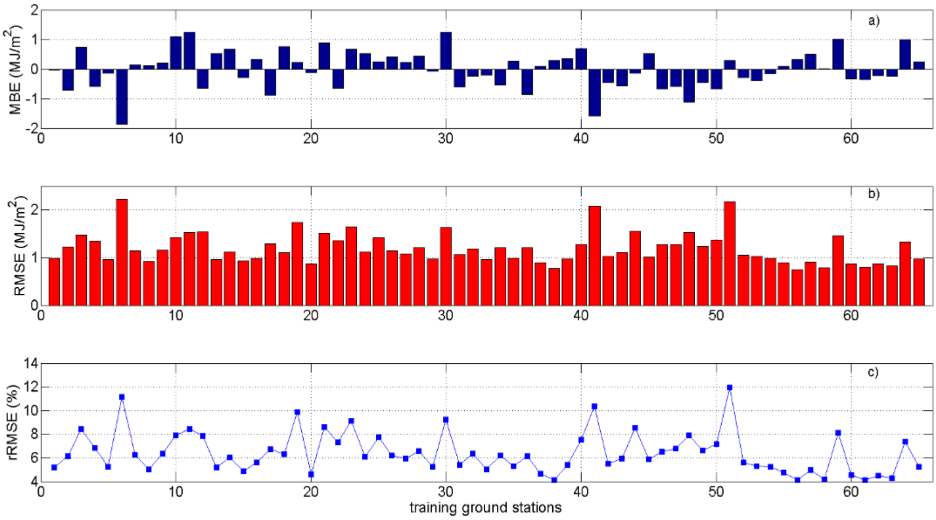

Figure 4. Comparison between measured and predicted radiation values, grouped by training stations.

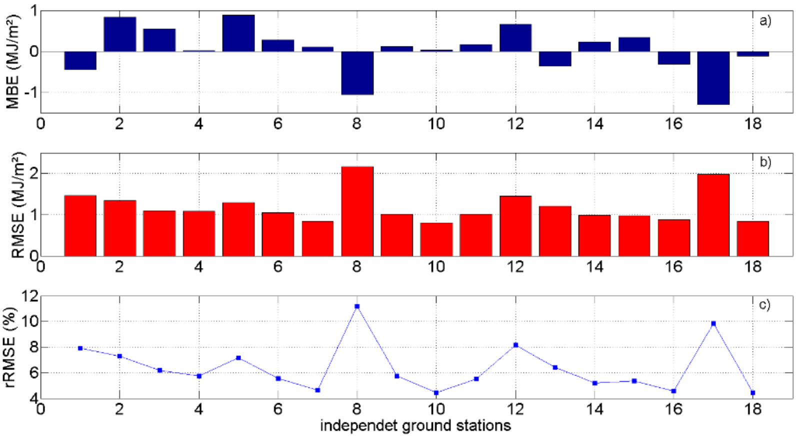

Figure 5. Comparison between measured and predicted radiation values, grouped by testing stations.

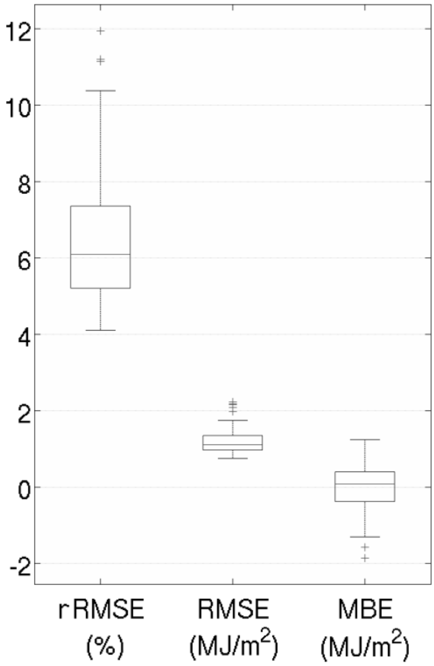

Figure 6. Boxplot of overall errors

These results confirm that the ANN-E model gave reliable results over the entire study region, with accurate estimates and spatially uniform errors. Only three training stations of the 65 (6th station: La Mojonera-Almería; 41st: Huesa-Jaén, and 51st: Estepona-Málaga) and one independent station of the 18 (17th: Puebla del Río-Sevilla) had slightly worse error estimates than other stations. This fact demonstrates the generalization capability of the model, and allows use of the ANN-E model to generate reliable estimates at any unobserved point within the study region, thereby generating accurate daily solar radiation maps.

4.2. Dependence on sky conditions

Fig. 7 shows error values of estimates grouped in quarters of a year. In Andalusia, summer is usually sunny and dry, and winter is cloudy and rainy. Hence, from April through September there are frequent clear-sky days, and the ANN-E model yields more accurate estimates than those from rainy months.

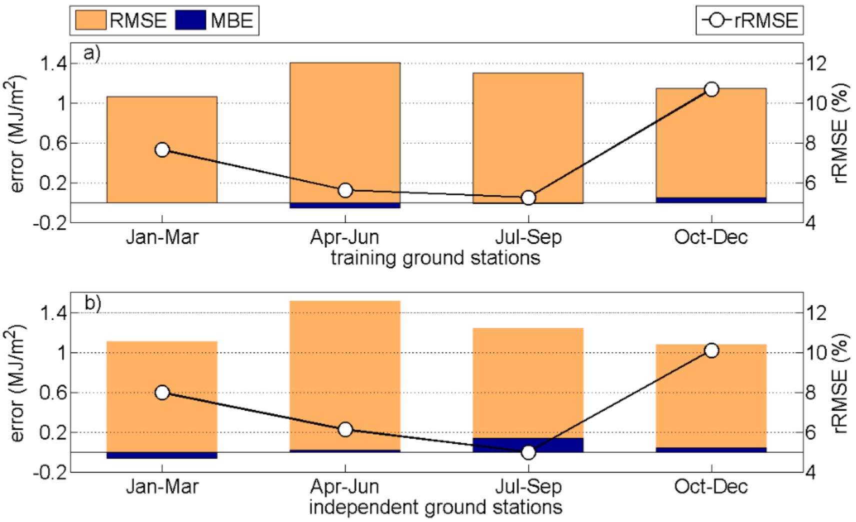

Figure 7. Error values of estimates grouped in quarters of a year, for a) training and b) testing stations.

To better evaluate the model for cloudy days, we calculated a clear-sky index K_C. It is defined as the ratio of measured global irradiance G_D to that received under clear-sky conditions, G_{CS}, which is estimated with the ESRA clear-sky solar radiation model (Section 3.2.1.) (Rigollier et al., 2004). Small K_C values mean that incoming radiation is much less than that expected under clear-sky conditions, i.e., they correspond to overcast conditions. High K_C values (near 1 or even greater) relate to clear-sky conditions. Figure 8 shows a histogram of K_C values for the training dataset. A nearly identical histogram was obtained for testing stations. The histogram reveals the high percentage of clear-sky days in Andalusia over a year.

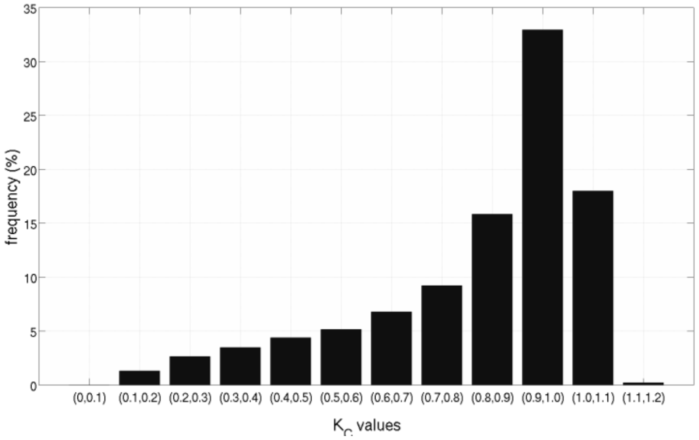

Figure 8. Histogram of K_C values

Results are listed in Table 3. Solar radiation estimates are sorted into three sets: $K_C<0.5$, $0.5\leq K_C \leq0.8$ and $K_C>0.8$, corresponding to overcast, intermediate and clear sky conditions, respectively.

Table 3
Error values of ANN-E model, grouped by clear-sky index values.

	Training stations			Testing stations		
	$K_C<0.5$	$0.5\leq K_C \leq0.8$	$K_C>0.8$	$K_C<0.5$	$0.5\leq K_C \leq0.8$	$K_C>0.8$
Num. of Values	2,789	4,993	15,810	782	1,349	4,439
MBE (MJ/m^2)	0.39	0.36	-0.19	0.35	0.36	-0.12
RMSE (MJ/m^2)	1.14	1.55	11.07	1.33	1.53	1.12
rRMSE	17.69%	11.07%	5.12%	21.2%	10.96%	5.13%

As expected, ANN-E generated the poorest solar radiation estimates in overcast conditions – rRMSE of 21.2%, against 5.13% for clear-sky days. Nevertheless, these errors for the least favourable sky conditions are superior to ones reported in the literature even under all sky conditions (e.g., Rigollier et al., 2004; Mefti et al., 2008; Bosch et al., 2010; Linares-Rodriguez et al., 2011; Lu et al., 2011; Roerink et al., 2012).

5. Summary and conclusions

A new approach for estimating daily global solar radiation through satellite-derived irradiances was formulated, via an optimized ANN ensemble model. The approach takes advantage of the high temporal and spatial resolution of Meteosat satellite images. Unlike most methods for deriving solar radiation from satellite imagery that use only visible channels, our model exploits all the information contained in the infrared channels of Meteosat 9.

The ANN model was constructed as an ensemble of five optimized, MLP feed-forward neural networks. The ANN inputs were the eleven Meteosat-9 channels, with 3-km nadir spatial resolution (approximately 4.5 km at study region latitudes), and an ESRA clear-sky term.

The five ANN models were calibrated with 75% of solar radiation observations at 65 training stations across the entire Andalusian region during 2008. As an independent validation dataset, we used 10% of observations in these calibration sets and a complete year of observations at an independent set of 18 stations across the region. The resulting ensemble ANN model produced accurate estimates of daily solar radiation at training and testing stations, which were virtually unbiased and had RMSEs between 4 and 9%. Overall RMSE at independent stations was 6.74%. The model outperformed previous solar radiation estimates on a daily basis, for both cloudy days and clear-sky conditions.

Homogeneity of RMSE and MBE values at nearly all the ground stations confirms that the ANN-E successfully learned the complex relationship between input variables and solar radiation, and it can be used to predict G_D at any location within the study region. Therefore, it can be used to generate accurate solar radiation maps region-wide, at the same spatial resolution as Meteosat images (4.5 km at the latitudes of the study region), that could play a strategic role in the location of solar energy applications in the study region.

Future work will focus on improving the temporal resolution of estimates, taking advantage of the high temporal sampling of satellite imagery (15 minutes). The aim is to continue improving methods to obtain more accurate solar radiation estimates every 15 minutes, by using all information contained in Meteosat channels.

Acknowledgments

This work was supported by the Spanish Ministry of Science and Technology (Project CGL2011-30377-C02-01). The data were kindly provided by the regional office of Agriculture and Fishing of Andalusia.

CHAPTER

4

AN ADVANCED ANN-BASED METHOD TO ESTIMATE HOURLY SOLAR RADIATION FROM MULTI-SPECTRAL MSG IMAGERY

S. Quesada-Ruiz, **A. Linares-Rodríguez**, J.A. Ruiz-Arias, D. Pozo-Vázquez, J. Tovar-Pescador. An advanced ANN-based method to estimate hourly solar radiation from multi-spectral MSG imagery. Solar Energy 115 (2015), pp. 494-504; doi:10.1016/j.solener.2015.03.014

ABSTRACT

In this work, a new method to derive hourly global horizontal irradiance (GHI) estimates from Meteosat Second Generation (MSG) imagery is presented. The method is based on an optimized Artificial Neural Network (ANN) ensemble model using a selection of the best ANN models identified from an initial ensemble that discerns between different sky conditions and an additional ensemble that con- siders all sky conditions together. For benchmarking purposes, hourly GHI estimates computed with the Heliosat-2 method, accounting for the diurnal variability of ground albedo, are used. Data collected during the 3-year period from 2009 to 2011 at 28 radiometric stations located in northern Africa, Middle East and Europe, are used in the procedure. From these stations, 7 are used to train the ANN models and the other 21 for independent validation. Results obtained with the proposed ANN ensemble model reduced the RMSE value of the Heliosat-2 model a 22% for all-sky conditions and a 42% for overcast conditions.

CHAPTER 4

AN ADVANCED ANN-BASED METHOD TO ESTIMATE HOURLY SOLAR RADIATION FROM MULTI-SPECTRAL MSG IMAGERY

1. Introduction

The sustainability of the current energy system is a major global concern. The global energy demand is rising and the production is based at a large extent on the use of fossil fuels, which are being depleted and are contributing decisively to the acceleration of Climate Change. Therefore, a great effort is being put on the research and development of alternative renewable sources for electricity generation. Solar and wind resources are large enough to sustain the worldwide-growing energy demand foreseen for the next few decades (Jacobson and Delucchi, 2011).

Knowledge of the spatial distribution of global horizontal irradiance (GHI) at the surface is important to determine the solar energy potential. However, the spatial distribution of GHI is of interest not only for energy applications but also in fields such as agriculture, hydrology, ecology or meteorology (Bojanowski et al., 2013). Different methodologies can be applied to obtain the regional and local distribution of GHI such as geostatistical techniques applied to ground irradiance observations (Alsamamra et al., 2009; Ruiz-Arias et al., 2011b), solar radiation models integrated in Geographical Information

Systems (GIS) (Ruiz-Arias et al., 2009), weather models that describe the evolution of the coupled land–atmosphere system (Ruiz-Arias et al., 2011a; Lara-Fanego et al., 2012), or models based on satellite imagery (Perez et al., 2002; Rigollier et al., 2004).

Observations gathered at radiometric sites are regarded as the most reliable source of solar radiation data. Nonetheless, the availability of such measurements is usually scarce and the use of geostationary meteorological satellites such as the Meteosat Second Generation (MSG) to derive solar irradiance over broad regions is accepted as the best alternative (Cano et al., 1986; Perez et al., 2002; Hammer et al., 2003; Mueller et al., 2004; Rigollier et al., 2004; Lefèvre et al., 2007; Moradi et al., 2009; Wahab et al., 2009; Polo et al., 2011; Linares-Rodriguez et al., 2013; Posselt et al., 2014). In fact, site-specific satellite-derived hourly irradiance values have proved that they can be more accurate than local ground observations if the distance from the location exceeds about 30 km (Perez et al., 1997; Zelenka et al., 1999). One of the most widely utilized methods to derive solar irradiance at the ground surface from the observations of geostationary meteorological satellites is the Heliosat-2 method (Rigollier et al., 2004). Heliosat-2 was originally developed for images of the MFG (Meteosat First Generation), but it has also been extensively used with the MSG (Meteosat Second Generation) imagery (Eissa et al., 2012; Ineichen, 2014).

Satellite data is also used for short-term solar radiation forecasting (up to 6 h). The common approach is based on cloud advection techniques such as cloud-motion vectors (Hammer et al., 1999), particle image velocimetry (PIV) (Marquez and Coimbra, 2013) or sector method (Quesada-Ruiz et al., 2014). Part of the solar forecasting error is explained by the satellite-to-irradiance estimation error. Therefore, any improvement in the reliability of the satellite GHI estimates will also reduce the solar forecasting error.

In the last decades, Artificial Neural Networks (ANNs) have extensively been used as a data-based alternative to physical modeling of complex problems in several fields of application, including meteorology (Kovordányi and Roy, 2009) and energy (Kalogirou, 2000; Kalogirou, 2001; Mellit and Kalogirou, 2008). Particularly, ANN models have been used in numerous studies as a method for estimating solar radiation components across large areas, using a variety of meteorological variables (Linares-Rodriguez et al., 2011) or information derived from satellite spectral channels (Zarzalejo, 2005; Perez et al., 2010b; Şenkal, 2010; Lu et al., 2011; Linares-Rodriguez et al., 2013) as inputs. It has been shown that ANN models may also outperform traditional regression approaches under some circumstances (Reddy, 2003; Tymvios et al., 2005; Elminir et al., 2007; Jiang, 2009).

In this paper, a new multi-spectral approach to derive hourly GHI values from the MSG imagery based on artificial intelligence techniques is presented. It exploits the relevant information for the atmospheric radiative transfer processes that is contained in the MSG spectral channels. The method consists of an optimized ANN ensemble model using a selection of the best ANN models identified from an initial ensemble that discerns between different sky conditions and an additional ensemble that considers all sky conditions together. All the ANN models make use of the eleven MSG spectral channels along with a clear- sky GHI model. Furthermore, hourly GHI estimates computed with the Heliosat-2 method, in which a procedure to account for the diurnal variability of ground albedo is introduced, are used for benchmarking. The ANN model has been calibrated with data from 7 radiometric sites and independently evaluated at other 21 radiometric sites during a 3-year period (2009–2011). These stations cover a vast region, from northern Europe to northern Africa (Fig. 1).

Section 2 describes the experimental dataset, including satellite and ground observations. In Section 3, the proposed method is described in detail. The reliability of the methodology is evaluated and the results obtained are presented in Section 4. Finally, in Section 5 the main conclusions and future work are outlined.

2. Data

Three different data sources have been used: reflectance images from the MSG imagery, which are used to represent the spatial distribution of clouds; clear-sky solar radiation model estimates, which are required as ancillary data; and solar radiation measurements from ground-based stations, which are needed to calibrate the model and to evaluate its performance.

2.1. MSG images

Images taken by the Meteosat-9 satellite during the 3- year study period, from 2009 to 2011, have been used. The Meteosat-9, which is the second MSG satellite –thus also referred to as MSG-2–, operates in a geostationary orbit over the equatorial plane (0º latitude) at 35,786-km above the earth's surface. During the study period, MSG-2 was located in its geostationary orbit at 0º longitude and operated in full-disk scanning mode. It carries onboard the Spinning Enhanced Visible and Infrared Imager (SEVIRI) instrument, that allows to take full disk earth's pictures every 15 min with a spatial resolution of 3 km at nadir (Schmetz et al., 2002) and at 11 different spectral channels (see Table 1, spectral channels 1–11), all used in the method proposed here. At this spatial resolution, a complete full disk image of the earth consists of 3712 x 3712 pixels, but for computing cost reduction a 1100x1700 pixels region, covering all the training and validation stations, was selected. In addition, SEVIRI offers a 1-km spatial resolution visible channel (spectral channel 12 in Table 1) that is not used here in order to maintain the spatial homogeneity with respect to the rest of spectral channels.

Table 1

Meteosat Second Generation (MSG) channels (Schmetz et al., 2002).

Channel number	Channel name	Spectral band (μm)	Pixel resolution at nadir (km)
01	VIS0.6	0.56–0.71	3
02	VIS0.8	0.74–0.88	3
03	NIR1.6	1.50–1.78	3
04	IR3.9	3.48–4.36	3
05	WV6.2	5.35–7.15	3
06	WV7.3	6.85–7.85	3
07	IR8.7	8.30–9.10	3
08	IR9.7	9.38–9.94	3
09	IR10.8	9.80–11.80	3
10	IR12.0	11.00–13.00	3
11	IR13.4	12.40–14.40	3
12	HRV	0.4–1.1	1

Specifically, Meteosat 9 High Rate SEVIRI Level 1.5 images for spectral channels 1 to 11 (Table 1) and corresponding to the period 01/01/2009 to 31/12/2011 were used and processed as described in Linares-Rodriguez et al. (2013).

2.2. Ground-measured GHI data

Hourly GHI ground observations have been gathered at 28 different sites from two different radiometric networks. Twenty of the sites belong to the Spanish National Radiometric Network (*http://www.aemet.es/en/idi/medio_ambiente/vigilancia*) of the Spanish National Weather Service (also referred to as AEMET), and the remaining ones belong to the Baseline Surface Radiation Network (BSRN) (Ohmura et al., 1998). Table 2 shows, for each radiometric site, the name, geographical location, altitude and number of hourly observations taken during the 3-year study period (2009 to 2011). For most of the stations, available measurements covered the whole study period, except IZA (Spain), CNR (Spain) and PAY (Switzerland) where missing values were found. Therefore, these three stations have been included in the training group. The spatial distribution of the selected stations is shown in Fig. 1. The range of latitudes spanned by the experimental sites is broad, going from 22.79° at TAM (Algeria) to 58.25° at TOR (Estonia). The altitudes go from sea level at CAB (The Netherlands) to 2373 m at IZA (Spain). The range of climatic characteristics covered by the stations is also notable, going from dry and warm conditions in the desert to humid and cold conditions in northern Europe. Therefore, the spatial and climate characteristics covered by the data ensure a broad applicability of the model.

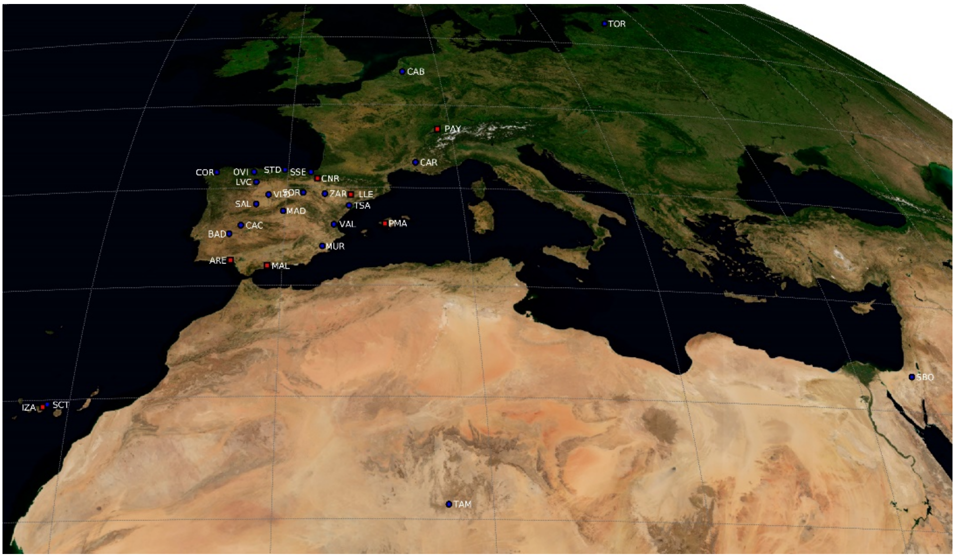

Figure 1. Geographical location of the radiometric sites used in this study from the BSRN and AEMET networks. Stations used to train the ANN models are marked with red squares; blue circles identify stations used for validation.

The radiometric stations of the AEMET are equipped with Kipp & Zonen CM11 and CM21 thermopile pyranometers, which undergo to biannual calibration traceable to the World Radiometric Reference. The solar radiation is registered every minute and standard quality control tests, such as control of equipment biases caused by tracking or shading issues, power outages, soiling and removal of unphysical values –e.g., closure issues (Michalsky et al., 1999; Gueymard and Myers, 2007)– are conducted before they are averaged to hourly values. The hourly GHI values at the BSRN sites are obtained by averaging the 1-min time-step observations.

From these 28 stations, only seven stations, identified in bold in Table 2 and marked with red squares in Fig. 1, were used for training the ANN models. The 21 remaining stations were used to independently validate the proposed models. The selection of the training and validation stations was conducted keeping the spatial representativeness of both datasets.

Table 2
Description of the radiometric sites used in this study from the BSRN and AEMET networks. Stations in bold are used to train the ANN models, while the remaining ones are used for validation.

SN	Id	Area name	Lat	Lon	Elev	Network	N. Obs.
1	TOR	Toravere (Estonia)	58.254	26.462	70	BSRN	7011
2	CAB	Cabauw (The Netherlands)	51.971	4.927	0	BSRN	7753
3	PAY	Payerne (Switzerland)	46.815	6.944	491	BSRN	2204
4	CAR	Carpentras (France)	44.083	5.059	100	BSRN	8819
5	STD	Santander (Spain)	43.491	-3.801	52	AEMET	8848
6	COR	La Coruña (Spain)	43.366	-8.421	58	AEMET	8889
7	OVI	Oviedo (Spain)	43.353	-5.874	336	AEMET	8679
8	SSE	San Sebastian (Spain)	43.306	-2.041	251	AEMET	8504
9	CNR	Navarra (Spain)	42.816	-1.601	471	BSRN	7400
10	LVC	La Virgen del Camino (Spain)	42.588	-5.651	916	AEMET	8820
11	SOR	Soria (Spain)	41.775	-2.483	1082	AEMET	8687
12	ZAR	Zaragoza (Spain)	41.679	-1.073	252	AEMET	8856
13	VLD	Valladolid (Spain)	41.641	-4.754	735	AEMET	8828
14	LLE	Lleida (Spain)	41.628	0.596	190	AEMET	8181
15	SAL	Salamanca (Spain)	40.959	-5.498	790	AEMET	8728
16	TSA	Tortosa (Spain)	40.820	0.493	47	AEMET	8931
17	MAD	Madrid (Spain)	40.452	-3.724	664	AEMET	9106
18	PMA	Palma de Mallorca (Spain)	39.561	2.737	8	AEMET	6745
19	VAL	Valencia (Spain)	39.485	-0.474	69	AEMET	9207
20	CAC	Cáceres (Spain)	39.471	-6.339	394	AEMET	8397
21	BAD	Badajoz (Spain)	38.886	-7.012	175	AEMET	9052
22	MUR	Murcia (Spain)	38.002	-1.171	61	AEMET	9239
23	ARE	El Arenosillo (Spain)	37.102	-6.738	41	AEMET	8929
24	MAL	Malaga (Spain)	36.719	-4.480	60	AEMET	9108
25	SBO	Sede Boqer (Israel)	30.860	34.779	500	BSRN	9609
26	SCT	Sta. Cruz Tenerife (Spain)	28.463	-16.255	35	AEMET	9142
27	IZA	Tenerife (Spain)	28.309	-16.499	2373	BSRN	8732
28	TAM	Tamanrasset (Algeria)	22.790	5.5292	1385	BSRN	9640

1.1. *Clear-sky solar radiation model*

GHI under clear-skies (G_c) is derived using the European Solar Radiation Atlas (ESRA) clear-sky solar irradiance model (Rigollier et al., 2000), following the original implementation of the Heliosat-2 method (Rigollier et al., 2004). In the ESRA clear-sky solar radiation model, atmospheric turbidity is represented by means of the Linke turbidity parameter, TL. The worldwide monthly climatology proposed by (Remund et al., 2003), freely available at http://www.soda-is.com, is used here.

3. Methodology

This section describes the proposed ANN ensemble model for deriving hourly GHI estimates (hereinafter referred to as *eANN*). As part of the validation process, the *eANN* model has been benchmarked against the well-known Heliosat-2 model (Rigollier et al., 2004). For the latter, hereinafter referred to as *H*2, the ground albedo has been evaluated independently for each diurnal time slot (Polo et al., 2012; Kleissl, 2013; Polo et al., 2013). The chain of algorithms used in the *H*2 method is briefly introduced in Section 3.1. The *eANN* model is described in Section 3.2. Finally, the statistics used to evaluate the results are presented in Section 3.3.

3.1. The Heliosat-2 method

The methodology for deriving GHI from satellite images is based on the generation of the cloud index, n, computed as

$$n = \frac{\rho_a - \rho_g}{\rho_{cloud} - \rho_g} \qquad \text{(Eq. 1)}$$

where ρ_α is the reflectance observed by the satellite sensor without considering the atmosphere contribution (apparent albedo), ρ_g is the apparent reflectance coming from the ground under clear-sky conditions (ground albedo), and ρ_{cloud} is the albedo of the most reflective clouds. Cloud index is related to the clear-sky index, K_c, which is defined as the ratio between GHI –also referred to as G– and its clear-sky modeled value –G_c, see Section 2.3, following Rigollier et al. (2004). Therefore, GHI estimates are obtained as $G=K_cG_c$.

The apparent albedo, ρ_α, represents the reflectance of the clouds and the earth's surface, while the observed albedo ρ includes also the contribution of the atmosphere (ρ_{atm}), and the additional attenuation of the solar radiation through the atmosphere, by means of the global downward transmittance, $T(\theta)$, and the global upward transmittance, $T(\theta_{sat})$ (Rigollier et al., 2000):

$$\rho_a = \frac{\rho - \rho_{\mathrm{atm}}}{T(\theta)T(\theta_{sat})} \qquad \text{(Eq. 2)}$$

The atmospheric albedo, ρ_{atm}, represents the atmospheric backscattered radiation received by the sensor, due to the dispersion of the incident and reflected solar radiation, and is computed by using Eq. (3) but with the atmospheric radiance (L_{atm}) (Rigollier et al., 2004) and the satellite zenith angle (θ_{sat}) instead. The cosine theorem has been used to derive θ_{sat}, considering a triangle with the following vertices: the earth center (C), the satellite (S) and the point of interest over the earth surface (*P*). Then, $h^2=r_e^2+r_s^2-2r_er_s\cos\beta$, and $\theta_{sat} = \pi - \cos^{-1}\left(\frac{h^2-r_e^2+r_s^2}{-2r_er_s}\right)$, where r_e, r_s, and h have been obtained following (Wolf and Just, 1999). Under clear-sky conditions, the albedo observed by the satellite sensor, ρ, is computed as

$$\rho = \frac{\pi - L}{I_{0met}\ \varepsilon\ cos\ \theta} \qquad \text{(Eq. 3)}$$

where L is the observed radiance, and I_{0met} = 693.17 Wm^{-2} is the total irradiance measured in the visible channel of the Meteosat-7 satellite (Rigollier et al., 2002). However, Meteosat-9 has two narrower visible channels – channels 1 and 2, centered at 0.6 and 0.8μm respectively– which have been combined to simulate the broadband visible channel radiances of the MFG (Cros et al., 2006), considering that there are no remarkable differences among broadband simulated radiances from Meteosat-8 and Meteosat-9 narrow visible bands.

$$L = 1.0605\ (4.49459L_{vis1} + 2.36764L_{vis2}) + 0.5909 \qquad \text{(Eq. 4)}$$

$$L_{vis1} = \frac{(L_\lambda)_1 I_{vis1}}{I_{m1}} \qquad L_{vis1} = \frac{(L_\lambda)_2 I_{vis2}}{I_{m2}} \qquad \text{(Eq. 5)}$$

where I_{vis1} = 120.45 Wm^{-2}, and I_{vis2} = 63.46 Wm^{-2}, are the maximum irradiances observed by channels 01 and 02 of Meteosat-9, respectively; and I_{m1} = 65.2065 mWm^{-2} cm; I_{m2} = 73.1869 mWm^{-2} cm, are the equivalent integrated irradiances of channels 01 and 02 of Meteosat-9, respectively.

3.1.1. Diurnal ground albedo

Ground albedo, ρ_g, represents the reflectance measured by the satellite sensor coming exclusively from the ground. The Heliosat-2 method (Lefèvre et al., 2004; Rigollier et al., 2004) uses one unique ground albedo value for each month. Thus, it does not take into account the ground albedo's diurnal variability, which is caused by solar-geometry effects that make ρ_g to change depending on the Sun-satellite angle (Kleissl, 2013). This variability may be relevant for hourly GHI derived from the MSG imagery.

Hence, the computation of a new ground albedo to be used with the Heliosat-2 method is proposed. In the Heliosat-2 method, ground albedo is inferred from the minima values of 1-month-length time series of apparent albedo values. In order to explicitly consider the diurnal variability of ground albedo, this process is here repeated independently for each time step at which satellite imagery is available during the day –that is solar elevation angles greater than 5º. Therefore, the variability of ground albedo within the day is described every month with up to 96 values corresponding to each time step, one every 15 min. For each time step, the second minimum of the series of apparent albedo (ρ_α) values is selected as estimate of the ground albedo value, but only if it exists and it is lower than the mean value of the series of apparent albedos for the particular time step. Otherwise, the first minimum is selected.

3.2. ANN ensemble model

It has been shown (e.g. Sharkey, 1999) that the robustness and reliability of an ANN can be often significantly improved by appropriately combining several ANN models into an ANN ensemble model. Here, four optimized ANN ensemble models were built from individual ANN models with similar characteristics. The first one ($eANN_{K_c}$) was used to classify the sky condition into three different groups. Classification is based on the clear-sky index (K_c), and ranges from overcast ($K_c < 0.4$) to intermediate ($0.4 \leq K_c < 0.8$) and clear-sky ($K_c \geq 0.8$) conditions. The second one ($eANN_{sky}$) is a set of three ANN models meant to estimate hourly GHI values for each sky condition. The third one ($eANN_{all}$) is a global ANN ensemble model meant to derive hourly GHI under all-sky conditions. Finally, the fourth ANN ensemble ($eANN$) is a combination of the ensemble $eANN_{sky}$ and the $eANN_{all}$ models ensemble models.

All the individual ANN models used here are multilayer perceptron, with one input layer, one hidden layer and one output layer. The architecture and optimization procedures are similar to those proposed in (Linares-Rodriguez et al., 2013). Fig. 2 sketches the structure of the ANN models used here.

The first eleven Meteosat-9 channels (Table 1) and the ESRA clear-sky model (Section 2.3) were used as input variables for all the ANN models. Therefore, the total number of input variables is 12 ($M = 12$). The effective radiance for each channel is obtained from the digital counts by means of the corresponding cal_{slope} and cal_{offset} coefficients. These variables have already shown to provide useful information to estimate solar radiation on a daily basis (Linares-Rodriguez et al., 2013). In this study, hourly input series were generated by averaging 15-min time-step input values.

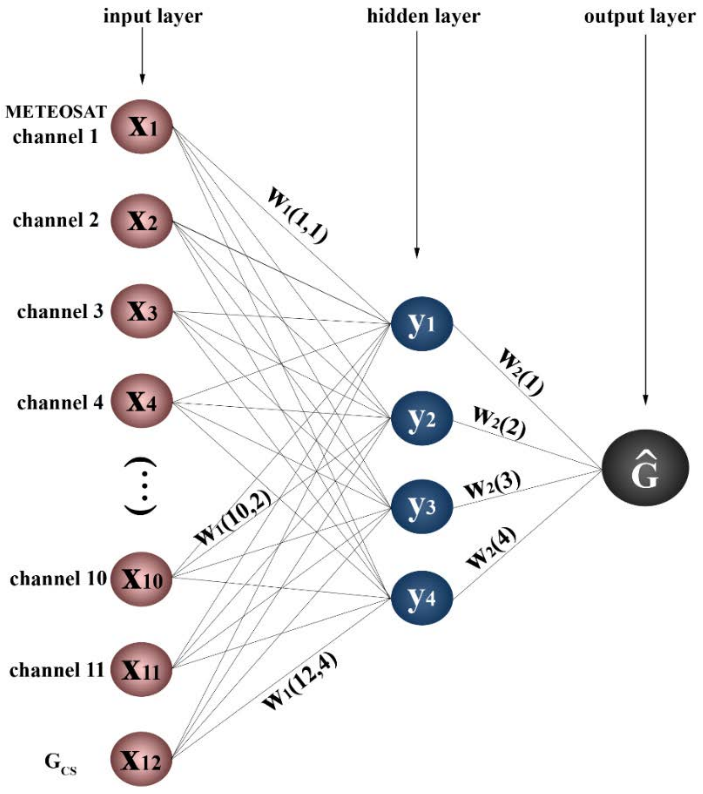

Figure 2. Multilayer perceptron feed-forward neural network used

In the $eANN_{Kc}$ ensemble model, the hidden layer consists of ten hidden neurons (N = 10), selected by a trial-and-error process, being their activation function (ψ) the hyperbolic tangent function $\psi = \tanh(x) = (\exp(2x) - 1)/(\exp(2x) + 1)$. For the training process of the ANNs, a Bayesian regulation backpropagation algorithm was used (Linares-Rodriguez et al., 2011). The clear-sky index values used for the ANN training process are generated using ground-based observations of hourly GHI values and the ESRA clear-sky model. For these ANNs, the clear-sky index ($\widehat{K}_c$) is the only model output, defined similarly to Eq. (6). As explained above, this $eANN_{Kc}$ ensemble model is used to split the input data into three groups depending on sky conditions. Then, three *eANN_{sky}* ensemble models are built by training over each of the three splitted groups: clear, intermediate and overcast sky.

In the $eANN_{sky}$, $eANN_{all}$, and *eANN* ensemble models, only four hidden neurons ($N = 4$) are used. In these ANNs, hourly global solar radiation ($\widehat{G}$) is the only model output, which is defined as

$$\widehat{G}(\vec{x})=\sum_{i=1}^{N}\psi\left(\sum_{j=1}^{M}x_j w_i(j,i)+b_1(i)\right)w_2(i)+b_2 \qquad \text{(Eq. 6)}$$

The four ANN ensemble models were trained, using all the available data together from the seven training stations (see Table 2). The individual ANN models were trained with the data for the years 2009 and 2010, with a 15% random selection of this dataset saved for calibration purposes. The training process was repeated 1000 times with random initial parameters. The selection of the best 10 members out of these 1000 individual ANN models was based on a validation conducted over the observed data during 2011.

The training procedure resulted in 50 optimized ANN models: 10 ANN_{Kc} models, 30 ANN_{sky} models, and 10 ANN_{all} models. The classifier ANN ensemble model ($eANN_{Kc}$) is built as the average of the 10 optimized ANN_{Kc} outputs. The $eANN_{sky}$ is built by averaging the 10 optimized ANN_{sky} outputs for each of the three sky conditions. The $eANN_{all}$ is built by averaging the 10 optimized ANN_{all} outputs. Finally, the *eANN* is generated by averaging the 10 optimized outputs for each of the three sky conditions from $eANN_{sky}$ and the 10 optimized outputs from $eANN_{all}$.

The reliability of the ensemble models was checked using independent data from the 21 validation stations throughout all the study period (2009–2011).

3.3. Evaluation of the results

The accuracy of the GHI estimates is assessed using the usual root mean squared error (RMSE) and mean bias error (MBE) statistics defined as follows:

$$\mathrm{RMSE}=\sqrt{\frac{1}{n}\sum_{\mathrm{h}=1}^{n}\left(\widehat{\mathrm{G}}_{\mathrm{h}}-\mathrm{G}_{\mathrm{h}}\right)^2} \qquad \text{(Eq. 7)}$$

$$\mathrm{MBE}=\frac{1}{\mathrm{n}}\sum_{\mathrm{h}=1}^{\mathrm{n}}\left(\widehat{\mathrm{G}}_{\mathrm{h}}-\mathrm{G}_{\mathrm{h}}\right) \qquad \text{(Eq. 8)}$$

where *n* is the number of sample points, $\widehat{G}_h$ is the hourly GHI estimates, and G_h is the corresponding measured values.

The relative improvement of the *eANN* model over the *H*2 model is evaluated with the RMSE skill score (s_{eANN}), defined as:

$$s_{eANN}=\left(1-\frac{RMSE_{eANN}}{RMSE_{H2}}\right)x100 \qquad \text{(Eq. 9)}$$

where $RMSE_{eANN}$ is the *eANN* model's RMSE and $RMSE_{H2}$ is the *H*2 model's RMSE.

4. Results

4.1. Heliosat-2

The hourly GHI estimates obtained with the Heliosat-2 model (*H*2) have been compared to the hourly GHI observations available at the 28 radiometric sites (Section 2.2). In average, the RMSE obtained with the *H*2 model over the entire validation dataset is 17% (similarly to the results showed in Table 3), consistent with the multi-model validation studies conducted by Ineichen (2011a; 2014) for Europe and northern Africa. These works reported RMSE values ranging from 16% to 24%. Hereinafter, the Heliosat-2 model (*H*2) will be considered as a reference for the ANN ensemble model (*eANN*).

4.2. ANN ensemble model

The hourly GHI estimates provided by the *eANN* model are based on the GHI estimates of two additional ANN ensemble models, namely, the $eANN_{sky}$, which discerns between three different sky conditions (overcast, intermediate, clear-sky), and the $eANN_{all}$, which provides GHI estimates for all-sky conditions indistinctly. In particular, the $eANN_{sky}$ ensemble model uses a previous ANN classifier ($eANN_{Kc}$) to decide the current sky condition. It reduces by 22% the misclassification error obtained when only the clear-sky index from *H*2 is used to discern the sky type. Table 4 shows an assessment of the hit rate of the ANN classifier model for each sky condition. As expected, the highest classification errors occur under intermediate skies. In this case, up to 19% of intermediate cases are classified as clear-sky and up to 8.5% are classified as overcast. However, overall, it provides the correct sky type in 87% of the cases.

Table 3
RMSE values for each validation station (Table 2) for the three ANN ensemble models (*eANNsky*; *eANNall*; *eANN*) and the Heliosat-2 model (*H2*). The last column shows the *eANN* RMSE skill score (Eq. (9)). The last row shows the validation results for the composite of all stations. Values are given in Wm-2 and in percentage, in parenthesis.

Station	$eANN_{sky}$	$eANN_{all}$	$eANN$	$H2$	s_{eANN}
TOR	88.6 (24.7%)	103.3 (28.8%)	91.7 (25.5%)	98.5 (27.4%)	6.9%
CAB	61.9 (16.9%)	57.8 (15.8%)	57.2 (15.6%)	90.4 (24.7%)	36.8%
CAR	56.2 (11.4%)	56.0 (11.3%)	55.0 (11.1%)	71.5 (14.4%)	22.9%
STD	85.1 (20.1%)	79.7 (18.8%)	81.2 (19.2%)	107.9 (25.5%)	24.7%
COR	67.3 (16.5%)	61.9 (15.1%)	62.8 (15.4%)	79.4 (19.4%)	20.6%
OVI	68.1 (17.6%)	64.9 (16.8%)	64.5 (16.7%)	101.9 (26.3%)	36.5%
SSE	76.0 (19.3%)	71.9 (18.3%)	72.3 (18.3%)	109.9 (27.9%)	34.4%
LVC	67.3 (13.1%)	66.2 (12.9%)	65.6 (12.8%)	82.1 (16.0%)	20.0%
SOR	79.3 (16.0%)	76.3 (15.4%)	76.6 (15.5%)	94.1 (19.0%)	18.4%
ZAR	55.6 (10.9%)	54.1 (10.6%)	53.1 (10.4%)	72.9 (14.3%)	27.3%
VLD	64.8 (12.6%)	61.2 (11.9%)	61.7 (12.0%)	83.0 (16.2%)	25.9%
SAL	60.4 (11.6%)	56.0 (10.7%)	56.6 (10.8%)	77.3 (14.8%)	27.0%
TSA	64.2 (13.3%)	62.3 (12.9%)	62.0 (12.9%)	84.7 (17.5%)	26.3%
MAD	62.7 (12.1%)	59.3 (11.5%)	59.9 (11.6%)	73.8 (14.3%)	18.9%
VAL	61.5 (12.5%)	59.3 (12.0%)	59.2 (12.0%)	74.2 (15.0%)	20.0%
CAC	59.6 (10.9%)	56.2 (10.3%)	56.7 (10.4%)	74.5 (13.7%)	24.1%
BAD	58.9 (11.1%)	55.2 (10.4%)	55.7 (10.5%)	72.4 (13.6%)	22.8%
MUR	56.9 (10.8%)	54.6 (10.3%)	54.5 (10.3%)	74.6 (14.1%)	27.0%
SBO	81.0 (13.2%)	103.9 (16.9%)	84.7 (13.8%)	89.2 (14.5%)	4.8%
SCT	89.1 (15.3%)	87.6 (15.1%)	85.5 (14.7%)	85.4 (14.7%)	0.0%
TAM	76.6 (11.3%)	78.6 (11.6%)	74.9 (11.0%)	85.4 (12.6%)	12.7%
Total	69.3 (14.0%)	69.4 (14.0%)	67.1 (13.5%)	85.4 (17.2%)	21.5%

Table 3 shows the RMSE values for the $eANN_{sky}$, $eANN_{all}$, $eANN$ and $H2$ models at each validation site (excluding the training sites) for the entire 3-year study period. The $eANN_{sky}$ and $eANN_{all}$ models show similar RMSE values, except in the TOR and SBO sites, where the $eANN_{sky}$ model provides smaller RMSE values. The overall MBE value of $eANNs_{ky}$ (-0.4%) is slightly lower than the one of $eANN_{all}$ (-1.4%). In average, the $eANN_{sky}$ model provides GHI estimates with lower RMSE than $eANN_{all}$ for each sky condition separately (not shown here). However, when the sky-type misclassification error is considered, the overall errors of the $eANN_{sky}$ and the $eANN_{all}$ models are similar. Nonetheless, as it has already been commented, the sky classification approach outperforms the $eANN_{all}$ model at some sites such as TOR and SBO that are characterized by highly reflective surfaces. Thus, the use of $eANN_{sky}$ and $eANN_{all}$ in $eANN$ results in overall benefits. The *eANN* model presents an overall mean RMSE value of 13.5% and a negligible MBE (-0.9%).

Table 4
Assessment of the sky classifier *eANNKc* ensemble model. Cases in the main diagonal are the correctly classified. Last rows show the hit rate for each sky condition and the overall value.

		Real		
		Overcast	Intermediate	Clear-sky
eANN$_{Kc}$	Overcast	22452	3382	85
	Intermediate	5112	28666	7676
	Clear-sky	150	7540	109052
	Hits (%):	81.0%	72.4%	93.4%
	Total:	87.0%		

The *eANN* model outperforms the *H*2 model at all the validation sites. In particular, the overall *eANN* RMSE improvement is 21.5%, reaching more than 36% for the CAB and OVI sites (Table 3). The comparative performance of the *eANN* and H2 models for different GHI regimes is illustrated in Fig. 3, that shows the scatterplots of observed values vis-à-vis modeled values for the *eANN* model (Fig. 3a) and the H2 model (Fig. 3b). The latter presents a general underestimation over the whole range of GHI values. The *eANN* model clearly reduces this under-estimation regardless the range of GHI values, but particularly for very low GHI values. Note that these low GHI values are usually coincident with high solar zenith angles and/or overcast conditions. The poor performance of the *H*2 model for large GHI values is probably related with limitations of the clear-sky model (Section 2.3).

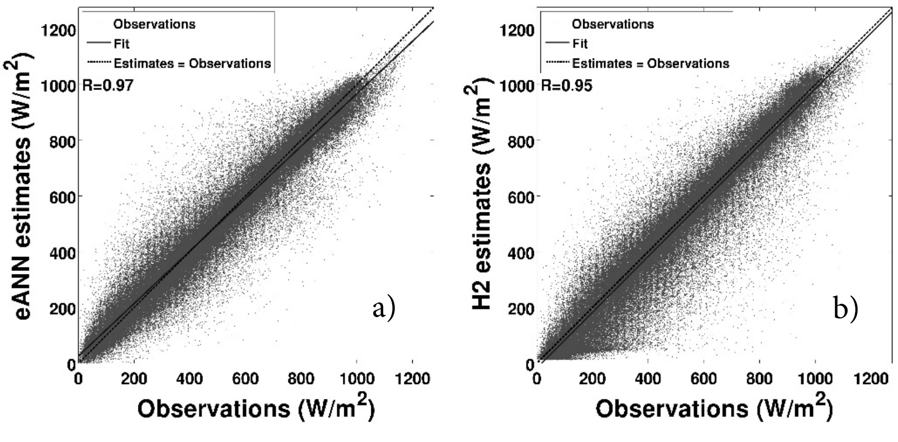

Figure 3. Modeled versus measured hourly GHI values for 21 validation stations, using the *eANN* ensemble model (a) and the *H*2 model (b).

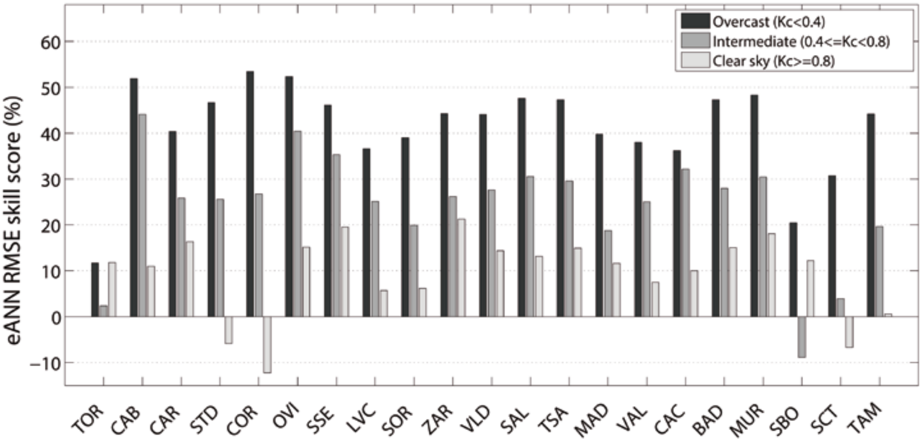

Figure 4. *eANN* RMSE skill score as defined in Eq. (9). Results are shown for each sky condition and the entire 3-year study period for the 21 validation stations.

Table 3 also shows that the RMSE of the *eANN* model ranges from about a 10% in sites dominated by clear-sky conditions, such as in CAC (southern Spain), to about a 19% in sites dominated by overcast conditions, such as in STD (northern Spain). This result suggests a relationship between the prevailing sky conditions and the overall GHI estimation error, such that in sites dominated by clear-sky conditions the overall RMSE is smaller than in sites dominated by overcast skies. Therefore, an analysis of the error based on the sky type, as defined in the classifier *eANN*$_{Kc}$ model, was carried out. In particular, the *eANN* model's performance has been analyzed for three different sky conditions: overcast ($K_c < 0.4$), intermediate ($0.4 \leq K_c < 0.8$) and clear-sky ($K_c \geq 0.8$).

Fig. 4 shows for each validation site the *eANN* RMSE skill score with respect to the *H*2 method for the three sky conditions separately. The *eANN* model outperforms the *H*2 model at all sites and all sky conditions except, very slightly, at three sites (STD, COR, and SCT) for clear skies and at SBO for intermediate conditions. Thus, the improvement in the reliability of the GHI attained with the *eANN* model is not constrained to a particular sky condition nor a particular area in the study region. The RMSE reduction achieved with the *eANN* model increases as the cloudiness increases. In particular, as can be seen in Table 5, the mean RMSE reduction under clear, intermediate and overcast skies is about 9%, 24% and 42%, respectively. For this particular sky classification, the RMSE over all the validation sites is 9%, 26% and 41% for clear, intermediate and overcast sky conditions, respectively.

Table 5
RMSE values in Wm^{-2} and in percentage in parenthesis, and RMSE skill score values of the *eANN* ensemble model in percentage, by sky type for each station separately, and all together (last row).

	Overcast (K_c<0.4)		**Intermediate** ($0.4 \leq K_c < 0.8$)		**Clear-sky** ($K_c \geq 0.8$)	
Station	**RMSE**	S_{eANN}	**RMSE**	S_{eANN}	**RMSE**	S_{eANN}
TOR	79.0 (60.7%)	11.7%	109.5 (34.9%)	2.4%	77.9 (15.4%)	11.8%
CAB	42.7 (33.3%)	51.9%	67.5 (20.5%)	44.1%	56.0 (10.9%)	11.0%
CAR	48.6 (41.2%)	40.4%	78.4 (23.3%)	25.8%	49.4 (8.3%)	16.4%
STD	62.3 (42.1%)	46.7%	107.3 (28.2%)	25.6%	71.4 (11.5%)	-5.8%
COR	43.2 (31.3%)	53.4%	70.5 (21.1%)	26.7%	65.8 (11.3%)	-12.2%
OVI	48.7 (36.4%)	52.4%	80.9 (24.1%)	40.4%	61.6 (10.7%)	15.1%
SSE	56.4 (44.0%)	46.1%	99.5 (28.3%)	35.3%	61.1 (10.3%)	19.5%
LVC	62.9 (45.6%)	36.6%	98.5 (26.8%)	25.1%	53.1 (8.5%)	5.7%
SOR	67.9 (42.4%)	39.0%	105.5 (28.3%)	19.9%	62.2 (10.0%)	6.2%
ZAR	51.6 (35.8%)	44.2%	80.5 (22.0%)	26.2%	42.9 (7.0%)	21.3%
VLD	53.1 (35.4%)	44.1%	91.2 (24.3%)	27.6%	48.1 (7.6%)	14.4%
SAL	50.0 (33.7%)	47.6%	81.0 (22.3%)	30.6%	46.5 (7.3%)	13.2%
TSA	52.5 (38.1%)	47.3%	93.1 (26.4%)	29.6%	52.9 (9.0%)	15.0%
MAD	53.5 (38.9%)	39.8%	91.0 (24.7%)	18.7%	48.6 (7.9%)	11.7%
VAL	58.7 (41.9%)	38.0%	85.0 (23.2%)	25.0%	50.2 (8.5%)	7.5%
CAC	70.1 (48.4%)	36.2%	79.0 (22.0%)	32.2%	47.8 (7.5%)	10.0%
BAD	42.2 (31.6%)	47.3%	73.7 (20.7%)	28.0%	51.6 (8.1%)	15.1%
MUR	45.9 (33.6%)	48.3%	80.1 (21.6%)	30.5%	46.8 (7.5%)	18.1%
SBO	141.8 (55.3%)	20.5%	139.8 (31.2%)	-8.9%	60.9 (9.1%)	12.2%
SCT	68.6 (42.2%)	30.7%	110.4 (29.3%)	3.9%	76.0 (11.2%)	-6.7%
TAM	80.7 (41.2%)	44.2%	111.7 (24.2%)	19.6%	64.4 (8.6%)	0.6%
Total	58.4 (41.4%)	42.1%	94.2 (25.9%)	23.7%	57.4 (9.2%)	8.9%

5. Conclusions

A new method to derive hourly GHI estimates from MSG imagery has been proposed and evaluated. The method (referred to as *eANN*) is based on the use of multiple ANN models. Each of these ANN models uses as inputs a clear-sky GHI model and the information of 11 spectral channels from the MSG satellite. Four different ensembles of ANN models were tested. The first one was meant to firstly classify the sky conditions based on the clear-sky index ($eANN_{Kc}$). The second one was meant to estimate the GHI based on the previous classification ($eANN_{sky}$). The third was meant to estimate the GHI directly under all sky conditions ($eANN_{all}$). Finally, an ensemble of the previous models was also evaluated (*eANN*).

In addition, a methodology to specifically account for the diurnal variability of the ground albedo has been pro- posed for the Heliosat-2 model (referred to as *H2*), which has been used as a skill reference for the *eANN* model. The *eANN* and *H*2 model estimates have been evaluated against hourly observations of GHI gathered from northern Africa to northern Europe, at 21 independent ground stations which cover a wide range of latitudes, climatic conditions and altitudes. The study period spans the years 2009, 2010 and 2011 at all the validation sites.

Results showed firstly, that the *eANN* ensemble model improved overall a 22% the RMSE value of the hourly GHI estimations using the *H*2. Secondly, results also proved the robustness and stability of the *eANN* ensemble model meaning that it can be used in locations distant from the training sites without significant loss of performance.

The $eANN_{sky}$ model showed a better performance than the $eANN_{all}$ when applied to cases where the sky conditions were correctly classified. But when considering the whole database, performance of these two ensemble models were similar. The combination of both model, the *eANN* ensemble, showed better performance than any of the previous ones. Notably, the *eANN* model showed a negligible MBE, and a relative RMSE ranging from 10% to 19%, which is lower than the ones from previous works (Zarzalejo et al., 2009; Eissa et al., 2012; Eissa et al., 2013; Ineichen, 2014). It was observed that the adverse weather conditions at high latitudes can lead to higher RMSE values, as founded in TOR (Estonia).

The analysis of the results revealed a relationship between the sky conditions and the GHI estimates error. In particular, RMSE is greater in overcast conditions stations for both *eANN* and *H*2 models. Nevertheless, the proposed *eANN* ensemble model showed a significant improvement for all sky conditions, when compared to the *H*2 model. This improvement is particularly outstanding for overcast conditions.

The $eANN_{Kc}$ ensemble model showed a misclassification error of the sky condition of 13%, which represents a reduction of 22% compared to error obtained using the clear-sky index (K_c) from Heliosat-2. However, this sky-condition misclassification error is an important contribution to optimize the accuracy of the *eANN* GHI estimates. Therefore, improvements in the sky-condition classification method should be considered in future works.

Acknowledgements

J.A. Ruiz-Arias is funded by the EU through a Marie Curie Action under the Project PIOF-GA-2010-273648 within the 7th European Community

Framework Programme. We acknowledge financial support given by the FPU Program of the Spanish Ministry of Education through a Grant to S. Quesada-Ruiz. The Spanish Ministry of Science and Innovation (Project CGL2011- 30377-C02-01), the Junta de Andalucia (research group TEP-220) and FEDER funds financed this research. We are grateful to the Spanish National Weather Service (AEMET) for providing the radiometric data.

CHAPTER 5

AN EVOLUTIONARY ARTIFICIAL NEURAL NETWORK ENSEMBLE MODEL FOR ESTIMATING HOURLY DIRECT NORMAL IRRADIANCES FROM METEOSAT IMAGERY

A. Linares-Rodríguez, S. Quesada-Ruiz, D. Pozo-Vázquez, J. Tovar-Pescador. An evolutionary artificial neural network ensemble model for estimating hourly direct normal irradiances from Meteosat imagery. Energy (2015). (Submitted)

ABSTRACT

A new evolutionary design of an ANN ensemble model is developed to generate hourly direct normal irradiance (DNI) estimates. The procedure combines a genetic algorithm for selecting the best inputs with an ANN ensemble method. The ensemble model was calibrated and evaluated using three years of Meteosat-9 images and data measured at 28 high-quality ground stations over an extensive area, mainly in Europe. The most valuable inputs for DNI estimation are shown to be the following: all Meteosat-9 channels except *ch08* and *ch11*; relative air mass m, integral Rayleigh optical thickness δ_r, extraterrestrial global irradiance G_0, beam clear-sky index B_{cs}, and the cosine of zenith angle θ. No additional atmospheric information such as turbidity, aerosol optical depth or water vapor content are required for the model. Ensemble estimates were nearly unbiased (MBE = 1.98%) and overall RMSE was 24.29% across an independent spatial and temporal dataset. This represents an improvement of 35% over other common methods for estimating DNI. The estimates were reasonably reliable in all seasons, and were more accurate in clear-sky conditions.

CHAPTER 5

AN EVOLUTIONARY ARTIFICIAL NEURAL NETWORK ENSEMBLE MODEL FOR ESTIMATING HOURLY DIRECT NORMAL IRRADIANCES FROM METEOSAT IMAGERY

1. Introduction

Solar power is acknowledged as one of the fastest-growing energy industries in the world (Kleissl, 2013). The design, performance analysis, and financial evaluation of solar power systems usually require accurate long-term resource projections. In particular, accurate time series (sometimes supplied as solar maps) of direct normal irradiance (DNI) estimates, i.e., direct irradiance received on a plane normal to the sun, provide very valuable information to developers of concentrated solar technologies, including concentrating solar thermal plants and photovoltaic tracking systems. Evaluation of location-specific DNI variability is also important for the solar energy sector, owing to steep ramp rates associated with cloud effects (Nonnenmacher et al., 2014). Moreover, real-time DNI estimates and DNI short-term forecasts are critical for improving plant operation performance (Quesada-Ruiz et al., 2014).

However, DNI estimation is not a trivial issue, mainly because (1) spatial and temporal availability of ground DNI measurements is currently too sparse, and (2) DNI is very sensitive to various atmospheric constituents (particularly aerosols) (Gueymard, 2012; Gueymard and Ruiz-Arias, 2015) and is strongly affected by clouds covering the sun. The latter causes DNI to vary greatly, much more so than global horizontal irradiance (GHI), making it more difficult to model.

Satellite data in conjunction with clear-sky irradiance models are commonly used to estimate DNI where ground measurements do not exist. Several satellite-to-irradiance models have been developed, including the SUNY model (Perez et al., 2002), Heliosat-2 model (Rigollier et al., 2004), the DLR-SOLEMI method (Schillings et al., 2004a) and their variations. Some of these models (e.g., SUNY) derive DNI and GHI estimates through satellite-based cloud index values and additional inputs, such as aerosol optical depth, sun elevation, ozone and water vapor concentration data. Other models only generate GHI estimates, so a global-to-beam decomposition model is needed to derive DNI.

The above decomposition models are widely used to derive DNI from GHI measurements (the latter being much more available than DNI measurements) and are based on empirical correlations between solar radiation components. The overall root mean square error (RMSE) of DNI values estimated by these methods using actual GHI measurements as inputs is about 20% (Bertrand et al., 2015). Therefore, if there are no ground GHI measurements, error will be increased by intrinsic error of GHI estimates.

In the present study, we use as reference the DIRINDEX global-to-beam method (Perez et al., 2002; Ineichen, 2008), because it has been proven accurate (Ineichen, 2008; Zhang et al., 2014). The DIRINDEX model is based on the DIRINT model (Perez et al., 1992), but specifically modified to consider atmospheric turbidity.

Studies over the last decade have generates reliable estimates of DNI on an hourly basis (Schillings et al., 2004b; Vignola et al., 2007; Ineichen, 2011b; Djebbar et al., 2012; Eissa et al., 2013; Ineichen, 2014; Nonnenmacher et al., 2014; Polo et al., 2014; Zhang et al., 2014; Bertrand et al., 2015). Table 1 shows a brief summary of some such studies. Some works directly estimate DNI, whereas others first estimate GHI and then apply a global-to-beam model.

Table 1 shows that at present, a favorable RMSE of DNI satellite-based estimates would be ~35%. With a few exceptions (e.g., RMSE = 21.67% at Merced station in Nonnenmacher's work, possibly because of predominantly clear-sky conditions), the only method achieving RMSE < 30% was based on an artificial neural network (ANN) ensemble with Meteosat Second Generation (MSG) satellite imagery as inputs (Eissa et al., 2013). The authors of the latter work developed an ANN model using six thermal channels from MSG for predicting GHI, DNI and diffuse horizontal irradiances over the United Arab Emirates. Relative RMSEs for DNI were 23.6% and 42.4% for the cloud-free and cloudy sky test datasets, respectively, and 26.10% for all sky conditions.

Table 1
Summary of representative studies regarding hourly DNI estimation

Publications [Ref]	**Validation dataset**	**Location / sites**	**Method**	**Best overall RMSE** (Wm^{-2} / %)
Bertrand et al. 2015	2011	Brussels, Belgium 1 site	RMI MAGIC/Heliosat-2 GHI and 10 global-to-beam models	54.5 33.4%
Ineichen 2014	2004-2011	Mainly Europe 14 sites	Six satellite-based models	119 – 174 34% – 49%
Zhang et al. 2014	2000-2005	Worldwide 39 sites	3-h NASA GEWEX SRB GHI and DIRINDEX global-to-beam model	209.6 50.6%
Nonnenmacher et al. 2014	Jan2011-Sep2012	California 4 sites	SUNY v2.0 GHI	137.9 − 161.9 21.67%−42.24%
Polo et al. 2014	2011-2012	Almería, Spain 1 site	Modified Heliosat-2 GHI and Louche global-to-beam model	182.43 –
Eissa et al. 2013	2009	United Arab Emirates 2 sites	ANN ensemble model and Meteosat imagery	– 26.10%
Djebbar et al. 2012	2004-2008	Canada 3 sites	SUNY v3.0 GHI	133.7 67.2%
Ineichen 2011	2006	Europe 10 sites	Five satellite-based models	– 35% − 54%
Vignola et al. 2007	2002	Kimberly, Idaho, 1 site	SUNY GHI	200 40.9%
Schilling et al. 2004	2000	Saudi Arabia 12 sites	DLR-SOLEMI GHI	166.9 36.1%

The aim of the present study was to build a model for obtaining accurate hourly DNI estimates over an extensive area using all MSG spectral channels. In a previous work (Quesada-Ruiz et al., 2015), we built an ANN ensemble model to estimate hourly GHI, using 11 MSG channels and a clear-sky model as ANN inputs. We attempted here to achieve similarly favorable results but for DNI estimates, by extracting all useful information contained in the visible and infrared channels.

To attain generalization, we used measured data from 2009 to 2011 at 28 ground stations over a large area for training and evaluating the models. Figure 1 shows geographic locations of these stations.

Because of their great variability, DNI time series are more complicated to estimate than GHI series, so additional data is presumably required to realize better models for DNI (Marquez and Coimbra, 2011). Thus, in addition to the 11 MSG channels, some variables used by other satellite-based approaches were added to the set of input variables (Rigollier et al., 2004; Quesada-Ruiz et al., 2015). This set was then as follows: MSG channels 1–11, observed albedo ρ, atmospheric albedo ρ_{atm}, apparent albedo ρ_a, cloud albedo ρ_{cloud}, relative air mass m, integral Rayleigh optical thickness δ_r, extraterrestrial global irradiance G_0, beam clear sky index B_{cs} and cosine of the zenith angle θ. Definitions of these variables are discussed in Section 2.3.

With this set of 20 candidate inputs, a new evolutionary design of an ANN ensemble model was developed to generate DNI estimates. The evolutionary procedure has two advantages: 1) the capability of a genetic algorithm (GA) to find optimal global solutions; 2) the fact that an ANN ensemble model outperforms a single such model, especially in complex cases (Hansen and Salamon, 1990; Sharkey, 1996; Sharkey, 1999).

The proposed algorithm is fully described in Section 3.3. Since there is no a priori information on the contribution of each input variable, a GA is used to select the best inputs, because redundant information can worsen the ANN estimates. The procedure is able to select the optimal combination of inputs while generating ANN samples optimized for an ensemble. After executing the evolutionary algorithm, a pool of 100 optimized ANNs is obtained, and aggregate estimates are constructed by averaging all their outputs.

Since the 1990s, GA and ANN have been used together in many works (Koehn, 1994; Yao, 1999). GA is extensively used for optimizing weights, network architecture or learning rules, or simply for selecting input variables (Yao, 1999; Castillo et al., 2000; Cook et al., 2000; Leung et al., 2003; Harpham et al., 2004; Shen and Fan, 2004; Palmes et al., 2005; Trevino and Falciani, 2006; Khazaee et al., 2008; Ding et al., 2011). In the solar radiation field, evolutionary ANNs have also been widely used (e.g., (e.g. (Kalogirou, 2004; Mellit, 2010; Mellit et al., 2010; Wang et al., 2011; Pedro and Coimbra, 2012; Chu et al., 2013; Mellit and Kalogirou, 2014)). Some works have successfully combined GA and ANN ensembles (Yao and Liu, 1998; Wang and Alhamdoosh, 2013; Chen et al., 2014).

This paper is organized as follows. In Section 2 we discuss the study area and data. We give details of the evolutionary procedure in Section 3, including the GA input selection method, development of the ANN ensemble, and test procedures to assess model performance. Results are discussed in Section 4 and conclusions presented in Section 5.

2. Data

2.1. Measured data

Hourly DNI measurements from 28 high-quality ground stations were collected to train and validate the models. Twenty of the sites belong to AEMET (the Spanish national weather service) (AEMET) and the remaining ones to the Baseline Surface Radiation Network (BSRN) (Ohmura et al., 1998). The sites cover latitudes from 22.79°N at Tamanrasset (Algeria) to 58.25°N at Toravere (Estonia), and longitudes 16.50°W at Tenerife (Spain) to 34.78°E at Sede Boqer (Israel). Site altitudes are from sea level to 2,373 m and they span a great variety of climates. Table 2 gives information on the 28 radiometric stations used, and Figure 1 shows their geographic locations.

We followed the same quality control procedure as in (Quesada-Ruiz et al., 2015). AEMET measurements are provided as hourly data, and 1-min BSRN data are averaged to obtain hourly time series. We used only data with zenith angle below 75°.

Only seven stations, tagged as *trainANN* in Table 2 and marked by red squares in Figure 1, were selected to train the models. These were selected considering either few available ground data or spatial representativeness of the entire dataset. Four stations, tagged as *trainENS* in Table 2 and marked by blue circles in Figure 1, were used as a validation set to build the evolutionary ensemble models. The 17 remaining stations, tagged as *test* in Table 2 and marked by filled black triangles in Figure 1, were used to check the reliability of the proposed ensemble models over an extensive independent dataset.

Table 2
Description of radiometric sites used, from BSRN and AEMET networks

N	Id	Area name	Dataset	Lat	Lon	Elev	Network	N.Obs.
1	TOR	Toravere (Estonia)	*test*	58.254	26.462	70	BSRN	7011
2	CAB	Cabauw (The Netherlands)	*test*	51.971	4.927	0	BSRN	7753
3	PAY	Payerne (Switzerland)	*trainANN*	46.815	6.944	491	BSRN	2204
4	CAR	Carpentras (France)	*test*	44.083	5.059	100	BSRN	8819
5	STD	Santander (Spain)	*test*	43.491	-3.801	52	AEMET	8848
6	COR	La Coruña (Spain)	*trainENS*	43.366	-8.421	58	AEMET	8889
7	OVI	Oviedo (Spain)	*trainENS*	43.353	-5.874	336	AEMET	8679
8	SSE	San Sebastian (Spain)	*trainENS*	43.306	-2.041	251	AEMET	8504
9	CNR	Navarra (Spain)	*trainANN*	42.816	-1.601	471	BSRN	7400
10	LVC	La Virgen del Camino (Sp)	*trainENS*	42.588	-5.651	916	AEMET	8820
11	SOR	Soria (Spain)	*test*	41.775	-2.483	1082	AEMET	8687
12	ZAR	Zaragoza (Spain)	*test*	41.679	-1.073	252	AEMET	8856
13	VLD	Valladolid (Spain)	*test*	41.641	-4.754	735	AEMET	8828
14	LLE	Lleida (Spain)	*trainANN*	41.628	0.596	190	AEMET	8181
15	SAL	Salamanca (Spain)	*test*	40.959	-5.498	790	AEMET	8728
16	TSA	Tortosa (Spain)	*test*	40.820	0.493	47	AEMET	8931
17	MAD	Madrid (Spain)	*test*	40.452	-3.724	664	AEMET	9106
18	PMA	Palma de Mallorca (Spain)	*trainANN*	39.561	2.737	8	AEMET	6745
19	VAL	Valencia (Spain)	*test*	39.485	-0.474	69	AEMET	9207
20	CAC	Caceres (Spain)	*test*	39.471	-6.339	394	AEMET	8397
21	BAD	Badajoz (Spain)	*test*	38.886	-7.012	175	AEMET	9052
22	MUR	Murcia (Spain)	*test*	38.002	-1.171	61	AEMET	9239
23	ARE	El Arenosillo (Spain)	*trainANN*	37.102	-6.738	41	AEMET	8929
24	MAL	Malaga (Spain)	*trainANN*	36.719	-4.480	60	AEMET	9108
25	SBO	Sede Boqer (Israel)	*test*	30.860	34.779	500	BSRN	9609
26	SCT	Sta. Cruz Tenerife (Spain)	*test*	28.463	-16.255	35	AEMET	9142
27	IZA	Tenerife (Spain)	*trainANN*	28.309	-16.499	2373	BSRN	8732
28	TAM	Tamanrasset (Algeria)	*test*	22.790	5.5292	1385	BSRN	9640

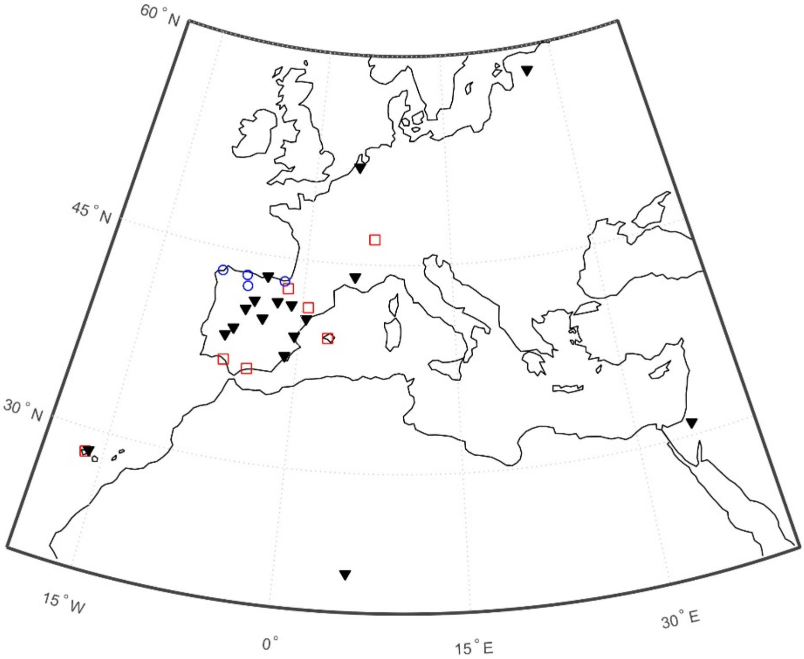

Figure 1. Geographic locations of ground stations used: *trainANN* stations are marked by red squares, *trainENS* stations by blue circles, and *test* stations by filled black triangles.

2.2. Meteosat-9 (MSG) images

Meteosat-9 images covering the period 1 January 2009 to 31 December 2011 were collected. Fifteen-minute satellite raw data were averaged and converted into hourly effective radiances following a procedure in the previous work (Quesada-Ruiz et al., 2015). Only the eleven 3-km channels were used in the present study. After applying a data quality filter, time series for each pixel containing ground station locations were extracted. The last column in Table 2 shows the number of valid records of for each station.

We refer to (Linares-Rodriguez et al., 2013) for a detailed description of MSG data acquisition and manipulation, as well as for potential information contained in each MSG channel.

2.3. Input variables

The set of input variables were the following: the 11 MSG channels, ρ, ρ_{atm}, ρ_a, ρ_{cloud}, m, δ_r, G_0, B_{cs} and $\cos\theta$. We followed the definitions of variables and data processing method in (Quesada-Ruiz et al., 2015). Refer to (Rigollier et al., 2004) for a detailed description of the definitions.

ρ observed by the spaceborne sensor is defined as

$$\rho = \frac{\pi L}{I_{0met}\, \varepsilon \cos\theta} \qquad \text{(Eq. 1)}$$

where L is the combined radiance observed by the two MSG visible channels (Cros et al., 2006), I_{0met}=693.17 Wm^{-2}, ε is the eccentricity correction factor of the earth's orbit, and θ is the sun zenith angle.

ρ_{atm} represents reflectance of the atmosphere toward the sensor, attributed to the scattering of incident and upward radiation toward that sensor:

$$\rho_{atm} = \frac{\pi L_{sat}}{I_{0met}\, \varepsilon \cos\theta_{sat}} \qquad \text{(Eq. 2)}$$

where L_{atm} is atmospheric radiance (dependent on the Linke turbidity factor) and θ_{sat} the satellite zenith angle.

ρ_a is the apparent albedo observed by the spaceborne sensor without considering the atmosphere contribution:

$$\rho_a = \frac{\rho - \rho_{atm}}{T(\theta)\, T(\theta_{sat})} \qquad \text{(Eq. 3)}$$

where $T(\theta)$ is global downward transmittance and $T(\theta_{sat})$ global upward transmittance, each being the sum of their beam and diffuse components.

ρ_{cloud} is the apparent albedo observed by the spaceborne sensor over the brightest clouds:

$$\rho_{cloud} = \frac{\rho_{eff} - \rho_{atm}}{T(\theta)\, T(\theta_{sat})} \qquad \text{(Eq. 4)}$$

where $\rho_{eff} = 0.78 - 0.13\,(1 - e^{4\cos^5\theta})$ (Eq. 1)

For G_0, we used the Iqbal definition (Iqbal, 1983). The formulations of m and δ_r are taken from (Rigollier et al., 2004) with modifications in (Geiger et al., 2002).

B_{cs} is a clear-sky beam index, defined as European Solar Radiation Atlas (ESRA) beam normal clear-sky irradiance (Rigollier et al., 2000) but without atmospheric turbidity, i.e., the Linke turbidity factor was set to 1 so that

$$B_{cs}=I_0 \cdot \varepsilon \cdot \exp(-0.8662 \cdot m \cdot \delta_r) \qquad \text{(Eq. 6)}$$

where I_0 is the solar constant (1,367 Wm^{-2}).

We selected candidate input variables requiring a minimum number of exogenous data. In most models, atmospheric data such as turbidity, aerosol optical depth or water vapor content are required to estimate solar radiation. In many situations, it is exceedingly difficult to acquire accurate atmospheric data at required temporal or spatial resolutions. Under such circumstances, reliable models requiring only satellite data are desirable.

In our study, only the 11 MSG channels and a monthly Linke turbidity factor (needed for deriving ρ_{atm}) were used as external data for building the model, leaving the ANN total freedom to extract other atmospheric information directly from the MSG channels (Linares-Rodriguez et al., 2011). In fact, we demonstrated that inputs depending on Linke turbidity may be discarded without compromising model reliability.

3. Methodology

Two evolutionary ANN ensemble models, called hereafter *EANNe* (evolutionary ANN ensemble) and *SEANNe* (simplified evolutionary ANN ensemble), were developed to estimate hourly DNI values. Both models were constructed as an ensemble of an optimized set of individual ANNs. All the ANN used have a similar topology, i.e., all are of the multilayer perceptron type, with one hidden layer, the same number of hidden neurons (M=5), one output layer, the hyperbolic tangent activation function, and a backpropagation learning scheme. The Matlab Neural Network Toolbox algorithm “trainlm” is used for training the ANNs (MATLAB), which updates weight and bias values according to Levenberg-Marquardt optimization. The training data are split into three subsets (calibration, validation and test) and the well-known early stopping method is used to avoid overfitting problems.

In the present study, the only ANN output consisted of the normalized DNI values K_N, defined as the ratio between DNI measured data and beam-normal clear-sky irradiance B_{cs}, defined above (Eq. 6).

To achieve generalization, i.e., to ensure that the trained ANNs can produce reliable estimates for both independent temporal and spatial datasets distinct from the training dataset, an additional data division was made as shown in Table 3, i.e., ground stations were split into three groups, *trainANN*, *trainENS* and *test* stations.

The method may be separated into two stages. First, large numbers of ANNs are trained with data from *trainANN* stations and then ranked and selected according to best scores of a GA fitness function against data from *trainENS* stations. Second, the optimized population of ANNs obtained in the first stage is aggregated to construct an accurate ensemble model, which is evaluated by independent data from *test* stations.

Table 3
Data division of training and validation sets to ensure temporal and spatial generalization capability for all the ANN-based models

Stations group	Ground stations	Year	No. Obs	Training ANN	Ranking ensemble candidates	Test model
trainANN	3, 9, 14, 18, 23, 24, 27	2009	14569	X	–	–
		2010	15849	X	–	–
		2011	16525	–	X	–
trainENS	6, 7, 8, 10	2009	11360	–	X	–
		2010	11413	–	–	X
		2011	11578	–	–	X
test	1-2, 4-5, 11-13, 15-17, 19-22, 25-26, 28	2009	48331	–	–	X
		2010	47328	–	–	X
		2011	49117	–	–	X

In the following subsections, the evolutionary design of the ensemble models is described.

3.1. Genetic algorithm for input selection

The GA is an iterative process that scans individuals in the search space to find the global optimum. The process is driven by the fitness of each individual. Problem states in a GA are denoted as chromosomes. The three principal genetic operators are selection, crossover and mutation (Goldberg, 1989).

We first used the GA to find best inputs from the 20 candidate variables. Therefore, GA chromosome length was fixed to the number of possible ANN inputs (*l* = 20). The genes are binary and determined whether an input variable was selected (gene value equal to 1) or not (gene value equal to 0) as ANN input. The algorithm began with a random set of N individuals that uniformly covered the search space. That is, a Nx*l* matrix (named *pool_1*) was initialized randomly with zeros and ones. We set N to 200.

The objective function is the mean square error between measured and estimated data over an independent dataset distinct from the training set.

Initially, 200 ANNs were created by decoding the genotype, i.e., each individual ANN was built with a reduced subset of input variables depending on its chromosome, and were then classified according the objective function; the best were selected as parents for the following generation individuals that were created through cross-over and mutation.

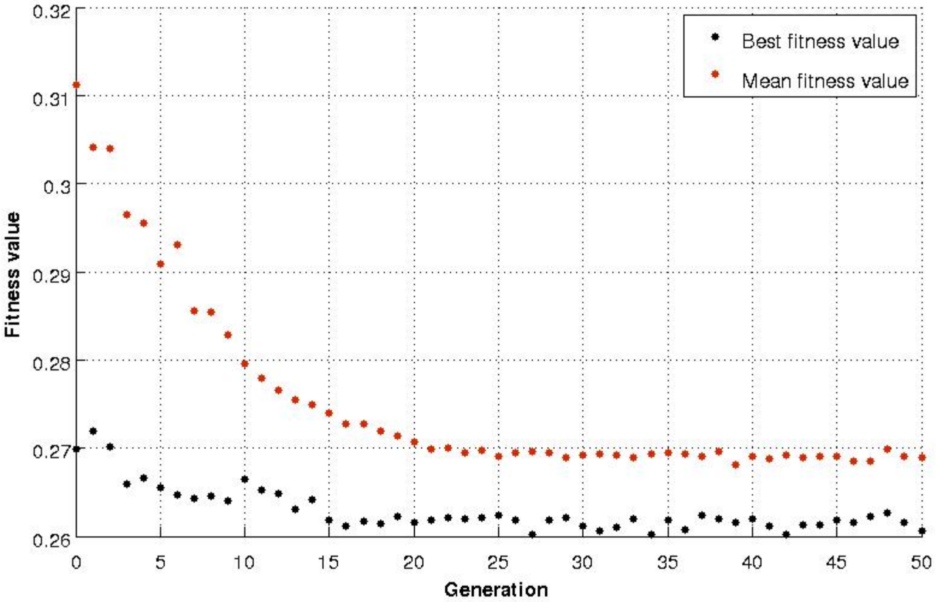

Figure 2. Genetic algorithm fitness values per each generation. Mean fitness values converge on best fitness values but do not reach them.

Usually, the iterative process continued until fitness of the best individual converged on average fitness of the entire population *pool_1*, or a maximum number of generations was reached. In our case, ANNs with identical architecture could attain different estimates, because the backpropagation algorithm may settle into a different relative minimum. For that reason, GA converged on average fitness of *pool_1* but failed to reach it. Figure 2 shows a typical convergence graph of a GA-ANN with backpropagation and random initial weights. This issue is important for the evolutionary design of the ANN ensemble (see Section 3.3).

3.2. ANN ensemble

It is well known that an ANN ensemble model outperforms an individual ANN model, provided that the ensemble members generalize differently (Sharkey, 1999; Chen et al., 2014). Indeed, the greater the diversity of the members, the better the aggregate estimate.

The most common methods to create useful ensemble members are bagging (Breiman, 1996) and boosting (Schapire, 1989). Both methods create those members by varying the training dataset, but in different ways. Bagging randomly resamples replicates from a given training dataset, whereas boosting sequentially resamples that dataset based on a misclassification probability distribution calculated from previous learned models. Other ensemble methods focus on creating diverse members by manipulating the initial weights, topology, learning algorithm, or input space (Sharkey, 1999; Akhand and Murase, 2010; Akhand and Murase, 2012; Alhamdoosh and Wang, 2014). All search to enhance diversity and accuracy among ensemble members.

Our proposed genetic-based ensemble optimizer (Section 3.3) generates ANN ensemble members by combining several methods (Akhand and Murase, 2010). In particular, diversity is achieved by randomly varying the initial weights, randomly picking 70% of the training set to train the nets and genetically manipulate the input variables.

Once the ensemble pool has been created, the aggregate estimates are built using the simplest method, i.e., averaging the outputs of the ensemble members.

3.3. Evolutionary ANN ensemble design

Here, we describe the proposed algorithm that can select the optimum set of ANN inputs while creating a new pool of optimized ensemble members.

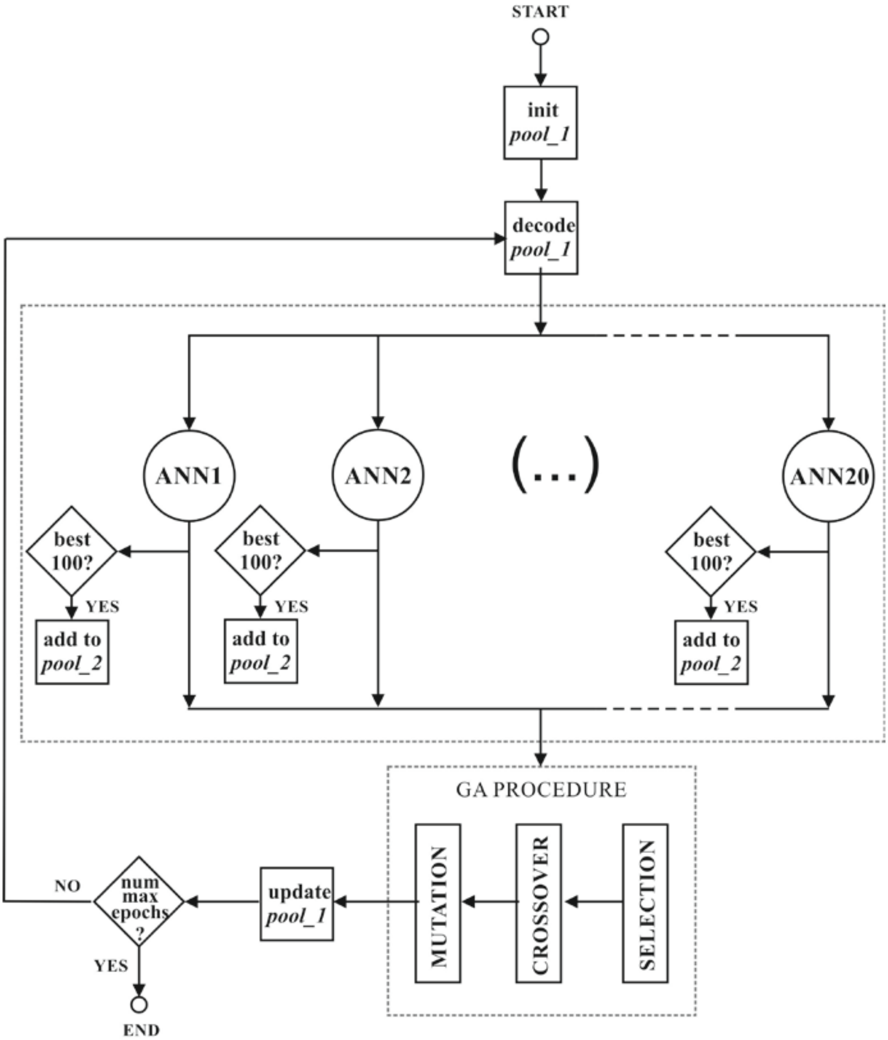

Figure 3. Flowchart of the evolutionary ANN ensemble design

Major steps of the algorithm are described in Figure 3 and explained further as follows.

(1) Randomly generate an initial population *pool_1* of N = 200 chromosomes of length 20. The *i*th gene (over 20 genes of each chromosome) represents whether the *i*th input variable is used as ANN input.
(2) Create 200 ANNs by decoding the chromosomes, i.e., by using the corresponding subset of inputs.
(3) Evaluate and rank the ANNs according to their fitness function value.
(4) If any of the ANNs achieve one of the 100 best fitness values, that ANN is selected and added to a pool of ANNs, *pool_2*.
(5) Apply the GA operators (selection, crossover, mutation) to the ANN population to produce offspring; *pool_1* is actualized.
(6) Repeat steps 2 through 5 until the maximum number of generations is reached (30 generations in the present study).

All ANNs created in step (2) have identical architecture, except for the number of inputs (decoded chromosome), initial weights (random), and learning dataset (random 70% of the training dataset).

Step (4) does not disturb GA evolution. While the GA is evolving the population *pool_1*, the 100 ANNs achieving best scores are stored in *pool_2*.

Both *pool_1* and *pool_2* contain useful information. In particular, the most valuable input variables for estimating DNI through neural networks may be extracted from the final population *pool_1*. Further, the ANNs stored in *pool_2* are assumed optimal for use as ensemble members, owing to greater diversity of its members (Yao and Liu, 1998). Since *pool_1* (200 chromosomes) is twice as large as *pool_2* (100 ANNs), we reduce *pool_1* to the best 100 chromosomes.

Two different ANN ensemble models were constructed using the information contained in *pool_1* and *pool_2*. *EANNe* was built by averaging outputs of all 100 members from pool_2, and was assumed to be the best model. A simplified version of this model, *SEANNe*, was constructed using only the minimum optimal number of inputs according to information contained in both *pool_1* and *pool_2*. The aim of this new model was to develop the simplest model that achieved reasonable accuracy.

4. Results and discussion

Results were validated using the well-known MBE (mean bias error) and RMSE statistics, between predicted and measured values of hourly DNI for the training and test datasets. Relative values were calculated by dividing by the average of measured data.

Accuracy and reliability of both evolutionary models (*EANNe* and *SEANNe*) were checked against three models used as benchmarks, *H2_dirindex*, *ANN_dni* and *ANN_dirindex*. Relative improvement of the evolutionary ANN ensemble model over the other models was evaluated with the RMSE skill score *sEANN*, defined as

$$\text{skill}_{EANNe}=\left(1-\frac{\text{RMSE}_{EANNe}}{\text{RMSE}_{benchmark}}\right)\text{x}100 \qquad \text{(Eq. 7)}$$

where RMSE_{EANNe} is the *EANNe* model's RMSE and $\text{RMSE}_{benchmark}$ is the RMSE of one of the models used as benchmark.

H2_dirindex was built by generating GHI estimates via the *Heliosat-2* method and then obtaining DNI values via the *dirindex* method. The other two models use results of a previous work (Quesada-Ruiz et al., 2015). In that work, an ANN ensemble model was developed using 11 visible and infrared MSG channels and clear-sky estimates as ANN inputs. The ensemble aggregate achieved accurate results. *ANN_dni* was constructed using the same set of inputs (11 MSG channels and clear-sky estimates) without any evolutionary optimization procedure, and *ANN_dirindex* was constructed by obtaining the direct normal component of the GHI estimates from the previous work via the *dirindex* method.

4.1. *SEANNe* (simplified evolutionary ANN ensemble) design

Figure 4 shows the frequency of each input variable in the final population *pool_1* and "ensemble" population *pool_2*. A new index, called *input_index*, was computed as the product of *pool_1* and *pool_2* frequencies. For each candidate input variable, the higher its *input_index* score, the more valuable it is for estimating DNI. Candidate inputs with *input_index* smaller than 50% were rejected. According to this new score, the inputs selected for the simplified model *SEANNe* were channels 1–7 and 9–10, m, δ_r, G_0, B_{cs}, and $\cos\theta$.

Two important facts should be mentioned here: 1) the albedo variables derived from MSG radiances may be neglected, so there was no need of any turbidity factor (used by L_{atm} in Eq. 2); 2) channels 8 and 11 have a negligible influence on the DNI estimates, which reduced the MSG data needed for model development.

Table 4

Brief description of two proposed evolutionary models and three benchmark models

Model	**ANN inputs / description**	**Num. of inputs**
EANNe	Channels 1-11, ρ, ρ_{atm}, ρ_{a}, ρ_{cloud}, m, δ_r, G_0, B_{cs}, $\cos\theta$	20
SEANNe	Channels 1-7,9-10; m, δ_r, G_0, B_{cs}, $\cos\theta$	14
H2_dirindex	Heliosat-2 inputs + dirindex	
ANN_dni	Channels 1-11, ESRA clear sky estimates	12
ANN_dirindex	Channels 1-11, ESRA clear sky estimates + dirindex	12

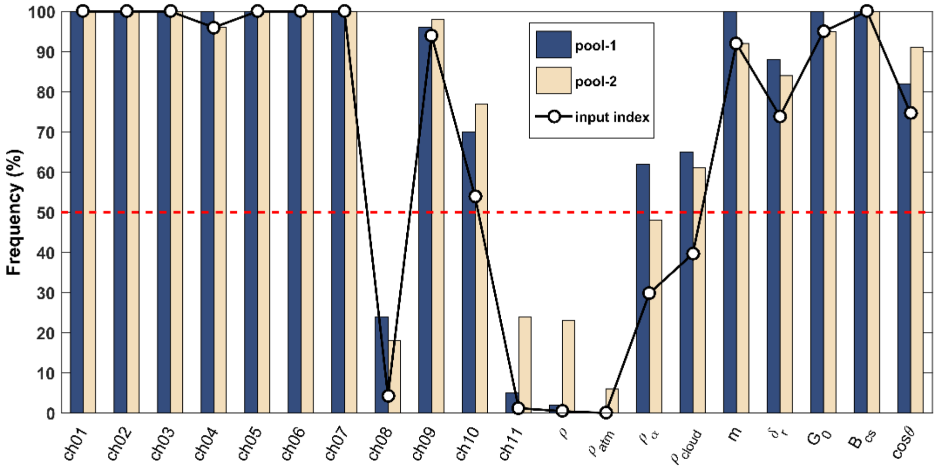

Figure 4. GA final population analysis for model input selection. High frequency of inclusion (*input_index* > 50%) indicates a variable useful for estimating DNI. *Ch01* denotes MSG channel number 01

4.2. Models assessment

According to Table 3, hourly measured DNI data collected at *trainENS* stations from 2010 to 2011 and at *test* stations from 2009 to 2011 were used to evaluate the five models. Table 4 shows the five models with their inputs, and Table 5 shows a summary of the major statistical scores of the models. Data from station TOR were excluded from this statistic for reasons explained later.

The first major result is that the *SEANNe* model achieved overall scores similar to *EANNe*. Although *EANNe* gave slightly better estimates, the fewer number of inputs makes *SEANNe* more attractive. For this reason, $skill_{EANNe}$, defined in Eq. 7, was evaluated using RMSE of *SEANNe* instead of the *EANNe*, and is displayed in the last column of Table 5. $skill_{EANNe}$ attained large values for the *H2_dirindex* and *ANN_dirindex* models (35.4% and 31.57%, respectively), indicating great improvement. Both models executing a *dirindex* method yielded an RMSE with the same order of magnitude as those listed in Table 1. Thus, the evolutionary ANN-based models reduced the overall RMSE of hourly DNI estimates from ~35% to ~24%.

The *ANN_dni* model produced accurate estimates but worse than those of the evolutionary models. One interpretation for this is that the relative improvement between conducting the evolutionary procedure and fixing the number of inputs is ~7.5%.

A box plot (Figure 5) shows errors between estimated and measured DNIs over the test dataset (172,117 hourly data). Within each box, the central mark shows the median of all error values, and box edges denote the 25th and 75th percentiles. Whiskers extend to the most extreme data points not considered outliers, and outliers are plotted individually. The *EANNe*, *SEANNe* and *ANN_dni* models, the three models without the *dirindex* procedure, have narrower boxes, meaning more reliable estimates.

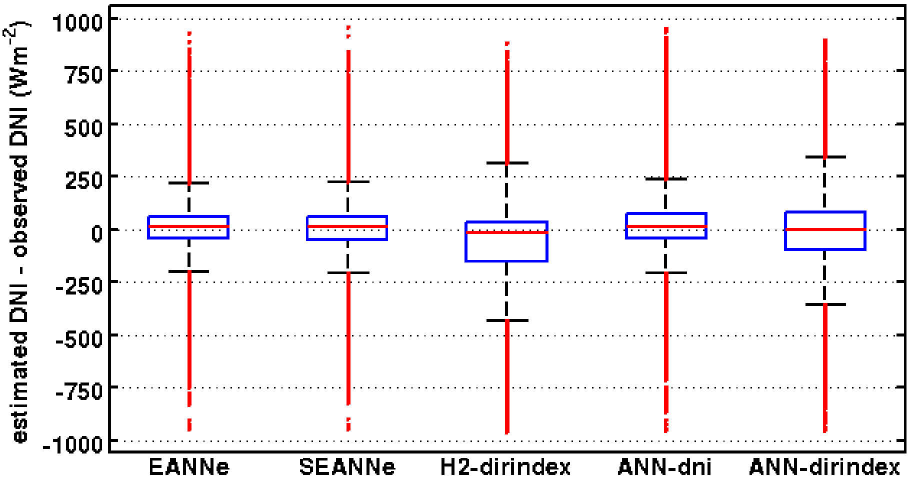

Figure 5. Box plots of errors of the five models

Table 5
Error values of the five models

DNI **Model**	**MBE** MW^{-2} (%)	**MAE** MW^{-2} (%)	**RMSE** MW^{-2} (%)	***skill**$_{SEANNe}$*
EANNe	12.06 (2.47%)	80.99 (16.56%)	118.49 (24.23%)	−0.24%
SEANNe	9.68 (1.98%)	81.8 (16.73%)	118.77 (24.29%)	−
H2_dirindex	−50.11 (−10.25%)	131.14 (26.82%)	183.86 (37.6%)	35.4%
ANN_dni	20.52 (4.2%)	86.59 (17.71%)	128.4 (26.26%)	7.5%
ANN_dirindex	−6.99 (−1.43%)	122.59 (25.07%)	173.56 (35.49%)	31.57%

Table 6
RMSE for each test station for the five models. Last column shows *SEANNe* skill RMSE score relative to *H2_dirindex* model used as benchmark

Sta-tion	***H2_dirindex***		***ANN_dirindex***		***ANN_dni***		***SEANNe***		***EANNe***		**% Skill**
	Wm^{-2}	**%**	**Wm^{-2}**	**%**	**Wm^{-2}**	**%**	**Wm^{-2}**	**%**	**Wm^{-2}**	**%**	**SEANNE**
TOR	181.41	54.77	198.95	60.07	174.95	52.82	199.39	60.2	182.07	54.97	-9.91
CAB	148.88	51.47	145.21	50.2	107.32	37.1	93.36	32.28	93.27	32.25	37.29
CAR	165.81	30.78	160.96	29.88	101.64	18.87	98.48	18.28	97.23	18.05	40.61
STD	163.93	46.69	154.96	44.14	119.18	33.95	114.37	32.58	115.74	32.96	30.23
SOR	178.2	36.58	178.63	36.66	137.48	28.22	137.02	28.12	136.3	27.98	23.11
ZAR	183.05	35.25	155.62	29.97	109.75	21.13	106.28	20.47	104.61	20.14	41.94
VLD	180.33	35.49	170.23	33.5	113.93	22.42	111.11	21.86	109.12	21.47	38.39
SAL	192.23	36.12	176.08	33.09	117.65	22.11	114.48	21.51	113.85	21.39	40.45
TSA	186.09	39.02	161.43	33.85	130.87	27.44	119.82	25.12	116.59	24.45	35.61
MAD	191.77	33.74	186.79	32.87	119.19	20.97	114.65	20.17	113.93	20.05	40.21
VAL	196.8	39.79	177.21	35.83	121.22	24.51	111.82	22.61	109.26	22.09	43.18
CAC	166.11	28.86	160.59	27.9	101.83	17.69	100.01	17.38	98.86	17.18	39.79
BAD	156.92	28.15	152.83	27.41	96.89	17.38	91.85	16.48	91.88	16.48	41.47
MUR	173.7	33.47	167.84	32.34	113.42	21.85	101.12	19.48	98.89	19.05	41.78
SBO	267.25	40.21	241.19	36.29	145.14	21.84	165.92	24.96	161.33	24.27	37.92
SCT	185.66	37.5	202.31	40.86	173.66	35.08	136.46	27.56	132.49	26.76	26.50
TAM	219.87	35.44	211.78	34.13	198.57	32	155.82	25.12	170.16	27.43	29.13

4.3. Location dependence of the estimates

The models were evaluated at each *test* station to check spatial reliability of the estimates. Table 6 shows RMSE values for each station and the two evolutionary models and three benchmark models. The last column shows the *SEANNe* RMSE skill score relative to the *H2_dirindex* model. As stated above, *EANNe* and *SEANNe* gave similar estimates. RMSE values for the *SEANNe* model were from 16.48% to 32.58%, except for the TOR station. All models produced poor results for this location, especially *SEANNe*. The range of RMSE values for the remaining stations (not shown in Table 6) was similar to that for the test stations, so we believe that the poor result at TOR is a unique case. Future work may explain this anomaly; perhaps it owes to adverse weather at high latitudes or the presence of snow. The poorer estimates were from the period October–March (Table 7), and snowfall is common in winter months at nearby Letonia (Latvian Meteorology Centre; *http://www.meteo.lv/en*). Moreover, the coarser spatial resolution of MSG images at high latitudes may lead to worse estimates. Therefore, we excluded TOR results from further model assessment.

$skill_{EANNe}$ values were large for all the remaining test stations (23.11% to 43.18%), indicating great improvement relative to the *H2_dirindex* model.

4.4. Seasonal dependence of the estimates

Table 6 also shows that RMSE of the *SEANNe* model ranged from ~17% at sites dominated by clear-sky conditions, such as BAD and CAC (southern Spain), to ~32% at sites dominated by overcast conditions, such as STD (northern Spain) or CAB (The Netherlands). This result suggests a relationship between prevailing sky conditions and overall DNI estimation error, with greater RMSE in clear sky conditions than in intermediate or overcast conditions. Therefore, a monthly error analysis was done to evaluate reliability of the *SEANNe* model in all seasons.

Table 7 shows RMSE values (%) and $skill_{SEANNe}$ of the *SEANNe* model for each month and *test* station. Monthly RMSEs were calculated using all available data for each station and month, and percentages were determined by averaging those RMSEs by mean DNIs over the same dataset.

As expected, in most cases the more accurate estimates (smaller RMSE) were achieved in summer months, with their greater number of sunny days. We have highlighted (bold) data in Table 7 as examples: BAD, CAC and MAD with July RMSEs of 9.15%, 10.97% and 12.82%, respectively, and CAR with August RMSE of 13.77%. In these cases, the $skill_{SEANNe}$ value is very large (48.22% to 59.37% at the four highlighted stations), indicating that the *SEANNe* model accurately estimated DNI under clear-sky conditions.

A contrasting result was obtained for station TAM (Algeria), also highlighted by bold data in Table 7. The number of clear-sky days is high year-round in Algeria, but it is known that dust loading across the Sahara peaks during the summer months (Banks et al., 2013). This may be why RMSE at TAM was ~10% in December (clear sky but less dust loading) but much greater in June (47.8%).

Table 7

RMSE (top of rows) and $skill_{SEANNE}$ relative to *H2_dirindex* model (bottom) for each test station and month. Last row shows overall RMSE and $skill_{SEANNE}$ for all stations and months. Data in **bold** explained in text

Station	JAN	FEB	MAR	APR	MAY	JUN	JUL	AUG	SEP	OCT	NOV	DEC
TOR*	–	147.92	136.69	51.77	44.22	44.16	45.82	50.09	61	71.47	83.65	–
	–	−57.15	−40.28	−13.72	−6.45	4.94	7.26	17.86	1.92	−17.38	−9.66	–
CAB	**58.59**	**84.32**	29.7	26.56	27.37	27.01	31.59	38.41	36.71	31.72	50.46	**87.88**
	15.83	32.4	43.49	28.97	40.31	36.77	36.22	39.65	35.5	47.6	35.51	24.44
CAR	22.87	24.3	21.13	18.73	18.1	18.21	14.67	**13.77**	16.3	19.68	25.88	27.14
	38.17	35.19	50.94	38.59	40.54	32.99	39.93	48.22	43.92	35.15	34.41	37.19
STD	43.46	34.66	27.14	31.87	41.3	34.33	32.69	32.69	25.6	27.48	31.8	38.63
	26.66	26.62	21.62	31.4	25.09	28.17	30.69	30.17	37.64	33.64	38.25	35.55
SOR	**55.46**	33.51	24.13	31.54	25.81	32.16	21.87	20.86	26.14	20.62	38.09	39.49
	22.49	23.56	35.63	17.45	33.75	15.25	22.72	20.98	14.79	24.71	21.95	25.27
ZAR	32.32	26.81	21.54	21.84	15.96	21.59	17.16	16.44	15.77	19.04	33.66	29.58
	35.26	35.07	42.25	37.79	48.96	43.13	28.67	44.34	48.48	50.95	40.51	36.02
VLD	**53.06**	26.27	20.53	28.14	21.83	20.89	13.06	15.19	18.4	22.4	57.94	36.24
	21.19	25.21	36.3	33.28	37.44	43.88	48.47	49.27	40.97	37.83	16.17	30.35
SAL	44.54	19.9	22	28.8	20.73	20.68	13.58	17.62	17.14	22.73	45.65	35.71
	28.54	52.47	38.19	28.67	42.51	39.95	51.44	36.75	50.28	40.22	28.34	29.31
TSA	26.21	32.12	26.65	31.16	20.73	24.95	24.69	24.74	24.23	21.12	25.27	21.9
	43.16	17.05	30.82	24.76	39.14	39.75	39.31	33.42	34.95	40.53	33.89	48.95
MAD	39.99	23.42	23.13	24.63	20.97	20.04	**12.82**	14.3	15.59	16.14	33.56	30.43
	17.47	32.88	34.27	36.74	29.53	40.53	54.94	53.56	49.41	49.76	28.56	24.51
VAL	25.04	24.74	24	29.26	22.23	18.36	21.78	25.7	18.36	19.31	20.87	22.81
	42.09	42.55	41.18	40.83	47.43	49	39	28.57	47.65	46.96	41.7	54.71
CAC	32.3	21.33	17.7	18.55	14.01	15.63	**10.97**	15.16	15.86	20.86	28.46	32.97
	31.32	29.79	45.2	39.37	53.91	38.8	52.61	33.41	42.83	28.49	32.53	24.04
BAD	33.57	18.46	18.27	18.43	15.88	14.11	**9.15**	14.47	14.43	16.06	32.32	26.69
	31.83	39.64	42.32	43.6	37.28	41.42	59.37	39.83	39.54	40.28	31.54	37.5
MUR	27.46	19.36	20.88	24.76	20.64	18.66	19.55	15.85	15.87	16.18	17.77	21.4
	33.26	44.47	42.22	38.91	38.3	48.18	26.25	42.17	47.92	47.96	47.17	47.48
SBO	29.32	34.06	30.71	30.11	28.52	21.09	18.18	15.98	22.48	25.49	25.96	26.66
	46.46	34.4	38.03	30.64	36.51	24.59	40.23	46.05	38.41	43.76	38.83	32.65
SCT	37.52	22.89	36.76	30.37	26.06	21.56	20.76	21.46	25.1	27.14	35.48	40.19
	12.87	34.76	24.79	30.87	29.26	25.32	29.75	26.85	33.13	32.41	20.18	11.92
TAM	11.86	15.7	30.84	25.57	36.04	**47.80**	34.64	30.38	21.32	26.97	14.48	**10.04**
	54.8	33.91	19.17	26.5	13.48	16.95	21.19	18.63	40.24	26.5	49.73	65.85
ALL	**32.72**	**26.23**	**26.47**	**27.25**	**24.77**	**24.09**	**20.06**	**20.82**	**21.15**	**22.92**	**30.24**	**28.81**
	34.62	**34.88**	**34.39**	**31.49**	**35.31**	**34.39**	**37.18**	**35.49**	**39.05**	**37.33**	**33.71**	**36.23**

* There is no available data (zenith angle below 75º) for TOR station in January and December. Some representative results are highlighted in bold and explained in the manuscript.

5. Conclusions

Two evolutionary ANN ensemble models, *EANNe* and *SEANNe*, were developed to estimate hourly DNI, and were evaluated using three years of measured data from 28 high-quality ground stations across an extensive area, mainly in Europe. The aim of the GA-based ensemble optimizer was twofold: (1) to select a small number of ANN input variables; and (2) to create optimized ensemble members achieving more accurate aggregate estimates.

Extracting information on final populations of the evolutionary design, we proved that in this case study, the simplified ensemble model *SEANNe*, i.e., the model built with an optimum minimum number of input variables, produced results very similar to the full ensemble model *EANNe*. The evaluation dataset was specifically selected to guarantee temporal and spatial reliability of the estimates.

The optimal set of input variables for the model were the following: all MSG channels except *ch08* and *ch11*; relative air mass *m*, integral Rayleigh optical thickness δ_r, extraterrestrial global irradiance G_0, beam clear sky index B_{cs} and cosine of the zenith angle θ. All albedo satellite-based variables were discarded. An important consequence of this action was that the *SEANNe* model was able to produce accurate hourly DNI estimates using only the MSG channels as exogenous data, i.e., no additional atmospheric information such as turbidity, aerosol optical depth or water vapor content were required for that estimation. This may be a substantial advantage for solar energy developers, because in many situations it is difficult to acquire accurate atmospheric data at required temporal or spatial resolutions.

The *SEANNe* DNI estimates were nearly unbiased (MBE = 1.98%) and overall RMSE was 24.29% for the entire independent dataset. This signifies relative improvement of 35.2% over the *H2_dirindex* method, considered here as a benchmark.

The *SEANNe* model gave accurate estimates at all ground stations except TOR (Letonia, Estonia), with RMSEs 16.48%–32.58%. Future work may explain the TOR anomaly, which may be attributable to high-latitude adverse weather or the presence of snow.

SEANNe estimates show a dependence on sky conditions, with great accuracy in clear-sky situations. After a *SEANNe* monthly assessment, we concluded that *SEANNe* output estimates superior to those of *H2_dirindex* in all months ($skill_{SEANNe}$ > 30% for all months). However, the ground stations used herein are mostly in dry or temperate/mesothermal climates according to the Köppen-Geiger climate classification. Thus, the *SEANNe* model may generate reliable estimates for an extensive area but may fail in "critical" areas, such as at latitudes greater than 60° (spatial resolution of MSG images is 3 km at nadir, but much coarser at high latitudes), high altitude, and in severe climates (e.g., tropical rainfall, presence of snow, and others). *SEANNe* should be evaluated in such critical areas, and it is likely that the entire evolutionary procedure must be repeated using training data from those areas.

Acknowledgements

This work was supported by the Spanish Ministry of Science and Technology (Project CGL2011-30377-C02-01). We are grateful to AEMET and BSRN for providing the radiometric data.

CHAPTER 6

CONCLUSIONES

1. Introducción

Para los desarrolladores y promotores de proyectos de energía solar, ya sea fotovoltaica o termosolar de concentración solar, hay dos cuestiones que son actualmente de vital importancia para asegurar la fiabilidad de los proyectos: 1) disponer de una evaluación precisa del recurso solar, tanto GHI como DNI (habitualmente en una amplia zona geográfica y a lo largo de decenas de años) y su variabilidad temporal, así como la producción eléctrica asociada a dicho recurso; y 2) disponer de pronósticos fiables de recurso solar y de producción eléctrica a corto y medio plazo.

La evaluación del recurso solar suele suministrarse como series temporales históricas en un punto o en una zona de estudio, a veces en forma de mapas de radiación. La situación ideal sería poder contar con una red densa de instrumentos de medida radiométricos, de forma que el mapa solar generado fuera lo más preciso posible. Lamentablemente la realidad difiere bastante de esta situación ideal, debido al escaso número de estaciones de tierra que midan la radiación en comparación con el número de estaciones que miden otras variables meteorológicas. Además, la mayor parte de esas estaciones radiométricas tan solo miden la radiación global horizontal, de forma que es aún más difícil conseguir mapas de DNI precisos a partir de tan escasos valores observados.

La tesis se ha centrado en proponer y evaluar diversos procedimientos para estimar tanto la GHI como la DNI, de forma que se pueda evaluar el recurso solar con mayor precisión.

Una mejora en la evaluación del recurso ayudará especialmente a los profesionales del sector de la energía solar a la hora de acometer nuevos proyectos solares, tanto en su fase de diseño como en la propia operatividad del sistema. De hecho, algunos de los métodos de pronóstico del recurso solar dependen previamente de la precisión en la estimación de los mapas del recurso; de esta forma, al mejorar la calidad de los mapas de DNI y GHI también se estarán mejorando dichos sistemas de pronóstico.

2. Resumen de los capítulos

El objetivo de obtener estimaciones de radiación solar de alta precisión se ha abordado gradualmente a lo largo de los capítulos de la tesis, mejorando progresivamente tanto la resolución espacial y temporal de los mismos como la propia metodología de los modelos. De esta forma, los últimos capítulos son los que proponen modelos más avanzados que generan estimaciones de GHI y DNI más precisas.

CAPÍTULO 2

El capítulo 2 se ha centrado en proponer y evaluar un modelo de redes neuronales artificiales (ANN por sus siglas en inglés) capaz de estimar la GHI diaria en Andalucía a partir de datos de los reanálisis *ERA-Interim* del Centro Europeo de Predicción a Plazo Medio. Estos reanálisis suministran –desde 1989 y de forma continua– una completísima base de datos meteorológicos que proporcionan un estado de la atmósfera a nivel global, con hasta 60 niveles de elevación vertical. Entre esos datos meteorológicos no se encuentra la radiación solar que llega a la superficie de la tierra. De esta forma, el modelo propuesto dota a esta base de datos –muy utilizada en numerosos artículos de investigación de diferentes campos científicos– de una nueva herramienta capaz de explotar aún más su valor meteorológico, ya que con sólo cuatro de sus múltiples variables es posible estimar con razonable precisión la radiación solar.

Como modelo se ha seleccionado una sola ANN optimizada, entrenada con datos diarios de casi diez años (desde 01/10/1999 a 31/12/2008) de 65 estaciones distribuidas por toda Andalucía, evaluada en 18 estaciones independientes durante el mismo periodo de tiempo y también durante un periodo posterior (todo el año 2009), verificando que los buenos resultados obtenidos son extrapolables sin pérdida de calidad a periodos de tiempo futuros.

Los resultados son similares (incluso mejoran) a los obtenidos en otros trabajos de estimación de GHI diaria: el RMSE global en las estaciones de test en el periodo 1999-2008 es del 16.41%, variando entre el 13.94% y el 21.42% dependiendo de las estaciones. El RMSE global en 2009 –periodo fuera del conjunto de entrenamiento– es semejante, en torno al 14.2%, lo que ratifica que el modelo ANN ha encontrado correctamente las relaciones entre las entradas y las salidas y genera estimaciones fiables.

El estudio espacial y estacional del modelo lleva a concluir que las estimaciones obtenidas con el modelo ANN dependen de dos factores: la distancia y, sobre todo, las condiciones de cielo:

1. Las estimaciones obtenidas son fiables en Andalucía, área cubierta por el conjunto de entrenamiento. Para obtener estimaciones en puntos fuera de esa zona habría que entrenar de nuevo la red neuronal, siendo el procedimiento igualmente válido.
2. En cielos nubosos la precisión de las estimaciones empeora: del 9.8% en cielos despejados al 34% en cielos totalmente cubiertos (datos sobre el periodo 1999-2008).

Como apuntábamos antes, estos resultados son razonablemente buenos, similares a otros encontrados en la literatura. Su precisión está limitada por las características intrínsecas de los reanálisis de *ERA-Interim*: resolución espacial de 0.7º (unos 70 km en la zona de estudio, aunque nosotros utilizamos una interpolación de 0.25º) y resolución temporal de 6 horas. La ventaja del modelo es que proporciona un valor añadido a la base de datos *ERA-Interim*, ya que con solo cuatro de sus variables el modelo es capaz de generar estimaciones de GHI, variable no generada directamente por el reanálisis.

CAPÍTULO 3

En el capítulo 3 se aborda la estimación de la GHI diari, haciendo uso de la mejor resolución espacial y temporal de las imágenes de satélite: imágenes cada 15 minutos con una resolución de 3km en el nadir (unos 4.5 km en la zona de Andalucía). La región de estudio es la misma que el trabajo anterior.

La novedad de este trabajo es que utiliza como entradas del modelo todos los canales espectrales del satélite Meteosat, tanto los visibles como los infrarrojos. Los modelos actuales de conversión de cuentas de satélite a radiancias sólo tienen en cuenta los canales visibles. El modelo propuesto demuestra la utilidad de introducir estos canales infrarrojos ya que contienen información meteorológica muy útil, que la red neuronal es capaz de relacionar con la radiación solar: presencia de nubes, aerosoles, vapor de agua, etc…

El nuevo modelo propuesto genera estimaciones diarias de GHI en Andalucía a través de un ensamble de las 5 mejores redes de 1000 ANN entrenadas. Las entradas de las redes neuronales son los 11 canales del satélite MSG (Meteosat Second Generation) y un modelo de GHI de cielo despejado.

Los resultados del modelo ensamble de redes neuronales mejoran los obtenidos utilizando los datos de *ERA-Interim* como entradas, y también suponen una mejora respecto de los métodos actuales de generación de estimaciones de radiación. El RMSE de las estimaciones en las 18 estaciones independientes resulta del 6.74%, con un rango entre el 4% y el 9% dependiendo de las estaciones. Esta escasa variabilidad justifica que pueda utilizarse el modelo para generar estimaciones fiables en toda Andalucía, y por tanto, crear mapas de GHI diaria para esta región con una resolución espacial igual a la de las imágenes de satélite, es decir, unos 4.5 km.

Las estimaciones de GHI muestran una dependencia con las condiciones de cielo: en cielos despejados las estimaciones son muy precisas –RMSE global del 5.13%–, y empeoran en cielos nubosos, presentando un RMSE global del 21.20% en cielos cubiertos.

En cuanto a la metodología, se comprueba que las estimaciones del modelo ensamble de redes neuronales mejora los resultados de una red aislada. El procedimiento selecciona las mejores redes que alcanzan un error mínimo relativo más cercano al absoluto. La estimación agregada es la media de las estimaciones de los cinco mejores modelos ANN, y se verifica que los desaciertos de unas estimaciones se compensan con los aciertos de las otras, resultando una estimación más estable y fiable, con un RMSE menor que los RMSE individuales de cada ANN.

La propia naturaleza de las redes neuronales obliga a disponer de gran cantidad de observaciones de GHI. Una vez utilizadas para entrenar, el modelo no las vuelve a utilizar, generando estimaciones de GHI a partir tan solo de una imagen de 11 canales de satélite.

CAPÍTULO 4

En el capítulo 4 abordamos el objetivo de generar estimaciones horarias de GHI sobre un área geográfica extensa. Las aplicaciones de los mapas diarios de GHI (o series temporales diarias de GHI en un punto) son muy variadas, en campos como agricultura, medio ambiente, climatología, hidrología, ecología, etc… (cfr. revisión bibliográfica en (Linares-Rodriguez et al., 2013; Linares-Rodriguez et al., 2015) Pero otras muchas aplicaciones exigen el conocimiento preciso de la GHI a una escala temporal mucho menor: horaria o quince-minutaria. La mayor resolución temporal exige más precisión en el procedimiento, ya que la variabilidad del recurso solar es mucho mayor a escala horaria que a escala diaria.

Junto a la mejora en la resolución temporal, este nuevo modelo también aborda el objetivo de mejorar la capacidad de extrapolación espacial a una zona mucho más extensa que en los trabajos anteriores, donde los modelos se evalúan en Andalucía (España). Para ello, utilizamos 3 años (2009-2011) de datos horarios de GHI de 28 estaciones radiométricas que abarcan latitudes desde 22.79ºN (Tamanrasset, Algeria) a 58.25ºN (Toravere, Estonia) y longitudes desde 16.50ºW (Tenerife) hasta 34.78ºE (Sede Boqer, Israel); tan solo 7 de esas estaciones se han utilizado para calibración.

El diseño de los modelos de redes neuronales es semejante al utilizado en el trabajo anterior, pero esta vez haciendo uso de la disponibilidad cada 15 minutos de imágenes de satélite. Promediando los valores de las radiancias espectrales de 4 imágenes consecutivas, el modelo es capaz de generar estimaciones horarias de GHI. Las entradas de la red son los 11 canales de MSG más un modelo horario de GHI de cielo despejado.

El modelo ensamble de redes es más complejo que el desarrollado en el capítulo anterior. El ensamble se construye con un número de redes neuronales mayor y que además presentan un alto grado de diversidad entre ellas. Es éste un resultado característico de un buen ensamble: a mayor diversidad entre las muestras del ensamble, el agregado es mejor: hay menos información redundante y las carencias de un modelo son compensadas por la precisión de los otros.

En concreto, se generan dos tipos de ensambles de redes: 1) un primer modelo ensamble de las 10 mejores redes que generan estimaciones horarias de GHI, entrenadas con todos los valores del conjunto de entrenamiento; y 2) un ensamble formado a su vez por la unión de otros 3 ensambles, cada uno entrenado con datos de entrenamiento separados por condiciones de cielo: cielo despejado, intermedio y cubierto. Al final, el mejor modelo resulta ser el ensamble de los 20 modelos construidos en los pasos anteriores.

Los resultados del modelo *eANN* definitivo son prometedores. Las estimaciones, como suele ser habitual en modelos basados en ANN, presentan un MBE casi nulo (-0.9%). El RMSE en todo el conjunto de validación es del 13.5%, lo que supone una mejora del 21.5% respecto al RMSE obtenido por el método Heliosat-2, tomado como referencia internacional.

El modelo genera estimaciones fiables en toda la región de estudio, con la única excepción de la estación de Toravere (Estonia), en donde todos los modelos empeoran sus estimaciones, quizá debido a las condiciones climáticas adversas en zonas de altas latitudes, la presencia de nieve, etc…

Como en los estudios anteriores, el modelo es sensible a la mayor o menor presencia de nubes. Así, el rango de RMSE de las estimaciones varía entre el 9.2% global en cielos despejados, al 41.4% en cielos cubiertos. Estos resultados son mejores que los reportados en la literatura, en todas las condiciones de cielo.

Estos buenos resultados confirman que los canales espectrales de los satélites MSG contienen información muy valiosa en relación con la radiación solar, y que el modelo es capaz de extraer esa información eficientemente. Al estar entrenados con datos de tres años y ser validado en un área extensa, concluimos que el modelo es capaz de generar mapas de radiación de toda esa zona con gran precisión, un 20% mejor que la precisión de los mapas obtenidos por otros métodos utilizados comúnmente por la comunidad científica. La extrapolación temporal también ha sido comprobada: de hecho el modelo se utiliza actualmente para generar estimaciones horarias de GHI a tiempo real dentro del grupo MATRAS de la Universidad de Jaén.

CAPÍTULO 5

En el capítulo 5 abordamos el objetivo de generar estimaciones de alta resolución de DNI en lugar de GHI. La escasa disponibilidad de datos observados de DNI ha llevado en la práctica a que la mayoría de los modelos de estimación de esta variable pasen primero por la estimación de la GHI, y luego a partir de la GHI se consiga estimar la DNI aplicando un modelo de descomposición de la radiación global en sus componentes directa y difusa. Estos modelos están muy extendidos en la práctica, pero conllevan ya un RMSE implícito del 20%, al que habría que sumarle el error propio de las estimaciones de la GHI. Es éste por tanto un punto crítico donde aún queda mucho margen de mejora. Algunos pocos modelos de estimación de GHI a través de imágenes de satélite también generan directamente estimaciones de DNI, saltándose ese paso de descomposición de la GHI, pero suelen necesitar de otras variables meteorológicas adicionales, a menudo no fáciles de conseguir a altas resoluciones: aerosoles, contenido de vapor de agua en la atmósfera, coeficiente de turbiedad, etc…

El objetivo del trabajo es diseñar y evaluar un modelo ensamble de redes neuronales capaz de generar estimaciones horarias de DNI directamente a partir de las imágenes de satélite, sin necesidad de recurrir a otras variables meteorológicas externas.

La estructura de las redes neuronales es semejante a la utilizada en el trabajo anterior. Lo que varía es el número de variables de entrada y el procedimiento de optimización del ensamble de redes.

La variabilidad de la DNI es mucho mayor que la GHI, ya que es muy sensible al paso de las nubes y a la presencia de aerosoles y otros constituyentes de la atmósfera. Por esta razón, parece razonable contar con un mayor número de variables de entrada, que puedan ayudar a la red a generar estimaciones precisas. En este trabajo utilizamos 20 variables como posibles entradas de los modelos de ANN: los 11 canales del satélite MSG (visibles e infrarrojos) más otras variables adicionales utilizadas en otros métodos basados en imágenes de satélite, en particular el Heliosat-2.

La novedad del artículo es doble: 1) se pretende generar directamente la DNI horaria explotando la información contenida en todos los canales del MSG, y 2) se propone un nuevo procedimiento evolutivo capaz de seleccionar genéticamente las entradas del modelo óptimas a la vez que se selecciona un conjunto óptimo de redes neuronales para luego generar una estimación agregada de alta precisión.

La zona de estudio es la misma que en el capítulo 4: se utilizan 3 años de datos horarios de DNI de 28 estaciones radiométricas de alta calidad que abarcan latitudes desde 22.79ºN a 58.25ºN y longitudes desde 16.50ºW hasta 34.78ºE, además de imágenes del satélite Meteosat-9 del mismo periodo.

El procedimiento evolutivo selecciona como entradas óptimas del modelo las siguientes: todos los canales del satélite Meteosat-9 excepto los canales 8 y 11; la masa óptica relativa *m*, el espesor óptico de Rayleigh δ_r, la irradiancia global extraterrestre G_0, un índice de radiación directa en cielo despejado B_{cs} and el coseno del ángulo cenital θ. Paralelamente, el procedimiento selecciona un conjunto de redes neuronales optimizadas para ser agregadas en un ensamble.

El modelo ensamble definitivo *SEANNe* presenta resultados bastante prometedores:

1. En primer lugar es de destacar que el modelo sólo utiliza como variables exógenas las imágenes de satélite, de donde obtiene toda la información meteorológica necesaria para estimar la DNI. Las demás variables de entrada dependen de la geometría Sol-Tierra, y no utilizan en sus definiciones ninguna variable meteorológica. Este resultado simplifica bastante la aplicación del modelo, ya que es capaz de convertir cada imagen de satélite en un mapa de DNI de mayor precisión que los mapas utilizados hasta el momento, sin necesidad de adquirir datos de alta resolución de aerosoles, vapor de agua, turbiedad, etc.
2. Los resultados, en base a los valores de RMSE en las 21 estaciones de validación, mejoran un 35% los resultados de, por ejemplo, el modelo Heliosat-2 combinado con el método DIRINDEX que se toma como referencia internacional. Si el RMSE de los métodos actuales se puede situar en torno al 35% en medidas horarias de DNI, el modelo evolutivo propuesto reduce ese RMSE global al 24%.

3. El modelo genera directamente de salida un valor de índice de claridad, que luego se convierte automáticamente en una estimación de DNI. Al aplicar el modelo sobre una imagen entera de satélite, lo que genera en primer lugar es pues un mapa muy preciso del índice de claridad. Estos mapas son la base de los actuales sistemas de pronóstico de radiación a corto plazo, capaces de predecir la GHI y la DNI en los siguientes 15 minutos y hasta unas 6 horas. Una mejora en estos mapas implica por tanto una mejora en los consiguientes pronósticos de GHI y DNI.

Como sucedía en el trabajo anterior (capítulo 4), el modelo genera estimaciones fiables en toda la región de estudio (RMSE que varía entre el 16.48% y el 32.58% dependiendo de las estaciones, con un RMSE medio global en las 21 estaciones del 24.29%), con la única excepción de la estación de Toravere (Estonia), en donde todos los modelos empeoran sus estimaciones. Habrá que desarrollar un estudio específico para conocer el comportamiento del modelo en zonas críticas: altas latitudes, condiciones climáticas severas, elevadas altitudes, etc. Para el resto de la amplia zona de estudio, se demuestra que las estimaciones son fiables más allá del periodo de tiempo de entrenamiento. De hecho, paralelamente a los mapas de GHI se generan actualmente a tiempo real de forma automática mapas de DNI dentro del grupo MATRAS de la Universidad de Jaén.

Del estudio estacional de las estimaciones del modelo evolutivo se desprende que dependen también de las condiciones de cielo, obteniéndose estimaciones de DNI muy precisas en cielos despejados, empeorando en cielos con mucha variabilidad nubosa. En todas las condiciones de cielo, las estimaciones con el modelo propuesto mejoran las obtenidas con otros modelos de referencia internacionales.

BIBLIOGRAPHY

AEMET. "http://www.aemet.es/en/idi/medio_ambiente/vigilancia (last access: 2015/05/15)."

Akaike, H. (1974). "A new look at the statistical model identification." Automatic Control, IEEE Transactions on **19**(6): 716-723.

Akhand, M. A. H. and K. Murase (2010). "Neural network ensemble construction fusing multiple popular methods." IAENG International Journal of Computer Science **37**(4).

Akhand, M. A. H. and K. Murase (2012). "Ensembles of neural networks based on the alteration of input feature values." International Journal of Neural Systems **22**(01): 77-87.

Alhamdoosh, M. and D. Wang (2014). "Fast decorrelated neural network ensembles with random weights." Information Sciences **264**(0): 104-117.

Alsamamra, H., J. A. Ruiz-Arias, D. Pozo-Vázquez and J. Tovar-Pescador (2009). "A comparative study of ordinary and residual kriging techniques for mapping global solar radiation over southern Spain." Agricultural and Forest Meteorology **149**(8): 1343-1357.

Banks, J. R., H. E. Brindley, C. Flamant, M. J. Garay, N. C. Hsu, O. V. Kalashnikova, L. Klüser and A. M. Sayer (2013). "Intercomparison of satellite dust retrieval products over the west African Sahara during the Fennec campaign in June 2011." Remote Sensing of Environment **136**(0): 99-116.

Batlles, F., J. Bosch, J. Tovar-Pescador, M. Martinez Durban, R. Ortega and I. Miralles (2008). "Determination of atmospheric parameters to estimate global radiation in areas of complex topography: Generation of global irradiation map." Energy Conversion and Management **49**(2): 336-345.

Behrang, M. A., E. Assareh, A. Ghanbarzadeh and A. R. Noghrehabadi (2010). "The potential of different artificial neural network (ANN) techniques in daily global solar radiation modeling based on meteorological data." Solar Energy **84**(8): 1468-1480.

Benghanem, M., A. Mellit and S. N. Alamri (2009). "ANN-based modelling and estimation of daily global solar radiation data: A case study." Energy Conversion and Management **50**(7): 1644-1655.

Bertrand, C., G. Vanderveken and M. Journée (2015). "Evaluation of decomposition models of various complexity to estimate the direct solar irradiance over Belgium." Renewable Energy **74**(0): 618-626.

Bishop, C. M. (1995). Neural Networks for Pattern Recognition, Oxford University Press, Inc.

Bojanowski, J. S., A. Vrieling and A. K. Skidmore (2013). "Calibration of solar radiation models for Europe using Meteosat Second Generation and weather station data." Agricultural and Forest Meteorology **176**(0): 1-9.

Bosch, J., G. Lopez and F. Batlles (2008). "Daily solar irradiation estimation over a mountainous area using artificial neural networks." Renewable Energy **33**(7): 1622-1628.

Bosch, J. L., F. J. Batlles, L. F. Zarzalejo and G. López (2010). "Solar resources estimation combining digital terrain models and satellite images techniques." Renewable Energy **35**(12): 2853-2861.

Breiman, L. (1996). "Bagging Predictors." Machine Learning **24**(2): 123-140.

Calcagno, V. and C. de Mazancourt (2010). "glmulti: An R package for easy automated model selection with (generalized) linear models." Journal of Statistical Software **34**(12).

Cano, D., J. M. Monget, M. Aubuisson, H. Guillard, N. Regas and L. Wald (1986). "A method for the determination of global solar radiation from meteorological satellite data." Solar Energy **37**: 31-39.

Cao, J. and S. Cao (2006). "Study of forecasting solar irradiance using neural networks with preprocessing sample data by wavelet analysis." Energy **31**(15): 3435-3445.

Cao, J. and X. Lin (2008). "Study of hourly and daily solar irradiation forecast using diagonal recurrent wavelet neural networks." Energy Conversion and Management **49**(6): 1396-1406.

Castillo, P. A., J. J. Merelo, A. Prieto, V. Rivas and G. Romero (2000). "G-Prop: Global optimization of multilayer perceptrons using GAs." Neurocomputing **35**(1–4): 149-163.

Cebecauer, T., M. Suri and R. Perez (2010). "High performance MSG satellite model for operational solar energy applications." Proc. ASES Annual Conference, Phoenix, AZ.

Cook, D. F., C. T. Ragsdale and R. L. Major (2000). "Combining a neural network with a genetic algorithm for process parameter optimization." Engineering Applications of Artificial Intelligence **13**(4): 391-396.

Cros, S., M. Albuisson and L. Wald (2006). "Simulating Meteosat-7 broadband radiances using two visible channels of Meteosat-8." Solar Energy **80**(3): 361-367.

Chen, W.-C., L.-Y. Tseng and C.-S. Wu (2014). "A unified evolutionary training scheme for single and ensemble of feedforward neural network." Neurocomputing **143**(0): 347-361.

Chu, Y., H. T. C. Pedro and C. F. M. Coimbra (2013). "Hybrid intra-hour DNI forecasts with sky image processing enhanced by stochastic learning." Solar Energy **98, Part C**(0): 592-603.

Delucchi, M. A. and M. Z. Jacobson (2011). "Providing all global energy with wind, water, and solar power, Part II: Reliability, system and transmission costs, and policies." Energy Policy **39**(3): 1170-1190.

deLlano-Paz, F., A. Calvo-Silvosa, S. Iglesias Antelo and I. Soares (2015). "The European low-carbon mix for 2030: The role of renewable energy sources in an environmentally and socially efficient approach." Renewable and Sustainable Energy Reviews **48**: 49-61.

Ding, S., H. Li, C. Su, J. Yu and F. Jin (2011). "Evolutionary artificial neural networks: a review." Artificial Intelligence Review **39**(3): 251-260.

Djebbar, R., R. Morris, D. Thevenard, R. Perez and J. Schlemmer (2012). "Assessment of SUNY Version 3 Global Horizontal and Direct Normal Solar Irradiance in Canada." Energy Procedia **30**(0): 1274-1283.

Dorvlo, A. S. S., J. A. Jervase and A. Al-Lawati (2002). "Solar radiation estimation using artificial neural networks." Applied Energy **71**: 307-319.

Eissa, Y., M. Chiesa and H. Ghedira (2012). "Assessment and recalibration of the Heliosat-2 method in global horizontal irradiance modeling over the desert environment of the UAE." Solar Energy **86**(6): 1816-1825.

Eissa, Y., P. R. Marpu, I. Gherboudj, H. Ghedira, T. B. M. J. Ouarda and M. Chiesa (2013). "Artificial neural network based model for retrieval of the direct normal, diffuse horizontal and global horizontal irradiances using SEVIRI images." Solar Energy **89**: 1-16.

Elminir, H., Y. Azzam and F. Younes (2007). "Prediction of hourly and daily diffuse fraction using neural network, as compared to linear regression models." Energy **32**(8): 1513-1523.

Estévez, J., P. Gavilán and J. V. Giráldez (2011). "Guidelines on validation procedures for meteorological data from automatic weather stations." Journal of Hydrology **402**(1-2): 144-154.

EUMETSAT (2005). "MSG Level 1.5 Image Data Format Description. EUM/MSG/ICD/105." (3).

EUMETSAT (2007a). "A planned change to the MSG Level 1.5 Image Product Radiance Definition, v1A. EUM/OPS-MSG/TEN/06/0519."

EUMETSAT (2007b). "Radiometric calibration of MSG SEVIRI Level 1.5 Image Data in Equivalent Spectral Blackbody Radiance. EUM/OPS-MSG/TEN/03/0064."

EUMETSAT (2008). "Effective Radiance and Brightness Temperature Relation for Meteosat-8 and 9." EUM/OPS-MSG/TEN/08/0024.

European_Commission (2008). "Communication from the commission: Energy efficiency: delivering the 20% target." COM **772 final**

European_Commission (2009). "Directive 2009/28/EC of the European Parliament and of the Council of 23 April 2009 on the promotion of the use of energy from renewable sources.".

European_Commission (2012). "Directive 2012/27/EU of the European Parliament and of the Council of 25 October 2012 on energy efficiency."

European_Commission (2014a). "Communication from the commission: A policy framework for climate and energy in the period from 2020 to 2030." COM **15 final**.

European_Commission (2014b). "Communication from the commission: Energy Efficiency and its contribution to energy security and the 2030 Framework for climate and energy policy." COM **520 final**.

Foresee, F. D. and M. T. Hagan (1997a). Gauss-Newton approximation to Bayesian regularization. In Proceedings of the 1997 International Joint Conference on Neural Networks**:** 1930--1935.

Foresee, F. D. and M. T. Hagan (1997b). "Gauss-Newton approximation to Bayesian regularization." Proceedings of the 1997 International Joint Conference on Neural Networks: 1930-1935.

García-Cuesta, E., I. M. Galván and A. J. de Castro (2008). "Multilayer perceptron as inverse model in a ground-based remote sensing temperature retrieval problem." Engineering Applications of Artificial Intelligence **21**(1): 26-34.

Geiger, M., L. Diabaté, L. Ménard and L. Wald (2002). "A web service for controlling the quality of measurements of global solar irradiation." Solar Energy **73**(6): 475-480.

Goldberg, D. E. (1989). Genetic Algorithms in Search, Optimization and Machine Learning, Addison-Wesley Longman Publishing Co., Inc.

Gueymard, C. and D. Myers (2007). Performance assessment of routine solar radiation measurements for improved solar resource and radiative modeling. Proceedings of the solar conference, American Solar Energy Society; American Institute of Architects.

Gueymard, C. A. (2012). "Temporal variability in direct and global irradiance at various time scales as affected by aerosols." Solar Energy **86**(12): 3544-3553.

Gueymard, C. A. and J. A. Ruiz-Arias (2015). "Validation of direct normal irradiance predictions under arid conditions: A review of radiative models and their turbidity-dependent performance." Renewable and Sustainable Energy Reviews **45**(0): 379-396.

Hagan, M. T., H. B. Demuth and M. H. Beale (1996). Neural Network Design. Boston, MA, PWS Publishing.

Hammer, A., D. Heinemann, C. Hoyer, R. Kuhlemann, E. Lorenz, R. Müller and H. G. Beyer (2003). "Solar energy assessment using remote sensing technologies." Remote Sensing of Environment **86**(3): 423-432.

Hammer, A., D. Heinemann, E. Lorenz and B. Lückehe (1999). "Short-term forecasting of solar radiation: a statistical approach using satellite data." Solar Energy **67**(1–3): 139-150.

Hansen, L. K. and P. Salamon (1990). "Neural network ensembles." Pattern Analysis and Machine Intelligence, IEEE Transactions on **12**(10): 993-1001.

Harmsen, R., B. Wesselink, W. Eichhammer and E. Worrell (2011). "The unrecognized contribution of renewable energy to Europe's energy savings target." Energy Policy **39**(6): 3425-3433.

Harpham, C., C. W. Dawson and M. R. Brown (2004). "A review of genetic algorithms applied to training radial basis function networks." Neural Computing and Applications **13**(3): 193-201.

Hocaoglu, F., O. Gerek and M. Kurban (2008). "Hourly solar radiation forecasting using optimal coefficient 2-D linear filters and feed-forward neural networks." Solar Energy **82**(8): 714-726.

Hofierka, J. and M. Súri (2004). "A New GIS-based Solar Radiation Model and Its Application to Photovoltaic Assessments." Transactions in GIS **8(2)**: 175-190.

Hontoria, L., J. Aguilera and P. Zufiria (2005). "An application of the multilayer perceptron: Solar radiation maps in Spain." Solar Energy **79**(5): 523-530.

Hornik, K., M. Stinchcombe and H. White (1989). "Multilayer feedforward networks are universal approximators." Neural Networks **2**(5): 359-366.

IEA (2014). "World energy outlook 2014." Paris: IEA/OECD.

Ineichen, P. (2006). "Comparison of eight clear sky broadband models against 16 independent data banks." Solar Energy **80**(4): 468-478.

Ineichen, P. (2008). "Comparison and validation of three global-to-beam irradiance models against ground measurements." Solar Energy **82**(6): 501-512.

Ineichen, P. (2011a). "Five satellite products deriving beam and global irradiance validation on data from 23 ground stations." Geneva. http://archive-ouverte.unige.ch/unige:23669.

Ineichen, P. (2011b). "IEA SHC Task 36. Solar data inter-comparison study. University of Geneva, Switzerland." Available from http://www.unige.ch/cuepe/pub/ineichen_valid-sat-2011-report.pdf (Last access: 05/18/2013)

Ineichen, P. (2014). "Long Term Satellite Global, Beam and Diffuse Irradiance Validation." Energy Procedia **48**(0): 1586-1596.

Ineichen, P. and R. Perez (1999). "Derivation of cloud index from geostationary satellites and application to the production of solar irradiance and daylight illuminance data." Theoretical and Applied Climatology **64**(1-2): 119-130.

Iqbal, M. (1983). An introduction to solar radiation. Toronto; New York, Academic Press.

Jacobson, M. Z. (2009). "Review of solutions to global warming, air pollution, and energy security." Energy & Environmental Science **2**(2): 148-173.

Jacobson, M. Z. and M. A. Delucchi (2011). "Providing all global energy with wind, water, and solar power, Part I: Technologies, energy resources, quantities and areas of infrastructure, and materials." Energy Policy **39**(3): 1154-1169.

Janjai, S., J. Laksanaboonsong, M. Nunez and A. Thongsathitya (2005). "Development of a method for generating operational solar radiation maps from satellite data for a tropical environment." Solar Energy **78**(6): 739-751.

Janjai, S., P. Pankaew, J. Laksanaboonsong and P. Kitichantaropas (2011). "Estimation of solar radiation over Cambodia from long-term satellite data." Renewable Energy **36**(4): 1214-1220.

Jarvis, A., H. I. Reuter, A. Nelson and E. Guevara (2006). "Hole-filled seamless SRTM data V3." Int. Cent. Trop. Agric. (CIAT), Retrieved from: http://srtm.csi.cgiar.org.

Jiang, Y. (2009). "Computation of monthly mean daily global solar radiation in China using artificial neural networks and comparison with other empirical models." Energy **34**(9): 1276-1283.

Johansson, B. (2013). "Security aspects of future renewable energy systems–A short overview." Energy **61**: 598-605.

Kalogirou, S. A. (2000). "Applications of artificial neural networks for energy systems." Applied Energy **67**: 17-35.

Kalogirou, S. A. (2001). "Artificial neural networks in renewable energy systems applications: a review." Renewable and Sustainable Energy Reviews **5**: 373-401.

Kalogirou, S. A. (2004). "Optimization of solar systems using artificial neural-networks and genetic algorithms." Applied Energy **77**(4): 383-405.

Khazaee, P. R., N. Mozayani and M. R. J. Motlagh (2008). "A genetic-based input variable selection algorithm using mutual information and wavelet network for time series prediction." Systems, Man and Cybernetics, 2008. SMC 2008. IEEE International Conference on: 2133-2137.

Kleissl, J. (2013). Solar energy forecasting and resource assessment, Academic Press.

Koca, A., H. F. Oztop, Y. Varol and G. O. Koca (2011). "Estimation of solar radiation using artificial neural networks with different input parameters for Mediterranean region of Anatolia in Turkey." Expert Systems with Applications **38**(7): 8756-8762.

Koehn, P. (1994). "Combining Genetic Algorithms and Neural Networks: The Encoding Problem."

Kovordányi, R. and C. Roy (2009). "Cyclone track forecasting based on satellite images using artificial neural networks." ISPRS Journal of Photogrammetry and Remote Sensing **64**(6): 513-521.

Kraas, B., M. Schroedter-Homscheidt and R. Madlener (2013). "Economic merits of a state-of-the-art concentrating solar power forecasting system for participation in the Spanish electricity market." Solar Energy **93**: 244-255.

Kumar Sahu, B. (2015). "A study on global solar PV energy developments and policies with special focus on the top ten solar PV power producing countries." Renewable and Sustainable Energy Reviews **43**: 621-634.

Lam, J., K. Wan and L. Yang (2008). "Solar radiation modelling using ANNs for different climates in China." Energy Conversion and Management **49**(5): 1080-1090.

Lara-Fanego, V., J. A. Ruiz-Arias, D. Pozo-Vázquez, F. J. Santos-Alamillos and J. Tovar-Pescador (2012). "Evaluation of the WRF model solar irradiance forecasts in Andalusia (southern Spain)." Solar Energy **86**(8): 2200-2217.

Lefèvre, M., M. Albuisson and L. Wald (2004). Description of the software Heliosat-2 for the conversion of images acquired by Meteosat satellites in the visible band into maps of solar radiation available at ground level.

Lefèvre, M., L. Wald and L. Diabaté (2007). "Using reduced data sets ISCCP-B2 from the Meteosat satellites to assess surface solar irradiance." Solar Energy **81**(2): 240-253.

Leshno, M., V. Y. Lin, A. Pinkus and S. Schocken (1993). "Multilayer feedforward networks with a nonpolynomial activation function can approximate any function." Neural Networks **6**(6): 861-867.

Leung, F. H.-F., H.-K. Lam, S.-H. Ling and P. K.-S. Tam (2003). "Tuning of the structure and parameters of a neural network using an improved genetic algorithm." Neural Networks, IEEE Transactions on **14**(1): 79-88.

Linares-Rodriguez, A., V. Lara-Fanego, D. Pozo-Vazquez and J. Tovar-Pescador (2015). "One-day-ahead streamflow forecasting using Artificial Neural Networks and a Meteorological Mesoscale Model." Journal of Hydrologic Engineering **0**(0): 05015001.

Linares-Rodriguez, A., J. A. Ruiz-Arias, D. Pozo-Vazquez and J. Tovar-Pescador (2013). "An artificial neural network ensemble model for estimating global solar radiation from Meteosat satellite images." Energy **61**(0): 636-645.

Linares-Rodriguez, A., J. A. Ruiz-Arias, D. Pozo-Vázquez and J. Tovar-Pescador (2011). "Generation of synthetic daily global solar radiation data based on ERA-Interim reanalysis and artificial neural networks." Energy **36**(8): 5356-5365.

Lopez, G., F. J. Batlles and J. Tovar-Pescador (2005). "Selection of input parameters to model direct solar irradiance by using artificial neural networks." Energy **30**(9): 1675-1684.

Lu, N., J. Qin, K. Yang and J. Sun (2011). "A simple and efficient algorithm to estimate daily global solar radiation from geostationary satellite data." Energy **36**(5): 3179-3188.

MacKay, D. J. C. (1992). "Bayesian Interpolation." Neural Computation **4**(3): 415-447.

Marquez, R. and C. F. M. Coimbra (2011). "Forecasting of global and direct solar irradiance using stochastic learning methods, ground experiments and the NWS database." Solar Energy **85**(5): 746-756.

Marquez, R. and C. F. M. Coimbra (2013). "Intra-hour DNI forecasting based on cloud tracking image analysis." Solar Energy **91**(0): 327-336.

MATLAB "The MathWorks, Inc., 3 Apple Hill Drive, Natick, MA 01760–2098, USA."

Mefti, A., A. Adane and M. Y. Bouroubi (2008). "Satellite approach based on cloud cover classification: Estimation of hourly global solar radiation from meteosat images." Energy Conversion and Management **49**(4): 652-659.

Mellit, A. (2010). "ANN-based GA for generating the sizing curve of stand-alone photovoltaic systems." Advances in Engineering Software **41**(5): 687-693.

Mellit, A. and S. Kalogirou (2008). "Artificial intelligence techniques for photovoltaic applications: A review." Progress in Energy and Combustion Science **34**(5): 574-632.

Mellit, A. and S. A. Kalogirou (2014). "MPPT-based artificial intelligence techniques for photovoltaic systems and its implementation into field programmable gate array chips: Review of current status and future perspectives." Energy **70**(0): 1-21.

Mellit, A., S. A. Kalogirou and M. Drif (2010). "Application of neural networks and genetic algorithms for sizing of photovoltaic systems." Renewable Energy **35**(12): 2881-2893.

Mellit, A. and A. M. Pavan (2010). "A 24-h forecast of solar irradiance using artificial neural network: Application for performance prediction of a grid-connected PV plant at Trieste, Italy." Solar Energy **84**(5): 807-821.

Michalsky, J., E. Dutton, M. Rubes, D. Nelson, T. Stoffel, M. Wesley, M. Splitt and J. DeLuisi (1999). "Optimal Measurement of Surface Shortwave Irradiance Using Current Instrumentation." Journal of Atmospheric and Oceanic Technology **16**(1): 55-69.

Mohandes, M., A. Balghonaim, M. Kassas, S. Rehman and T. O. Halawani (2000). "Use of radial basis functions for estimating monthly mean daily solar radiation." Solar Energy **68**: 161-168.

Mohandes, M., S. Rehman and T. O. Halawani (1998). "Estimation of global solar radiation using artificial neural networks." Renewable Energy **14**(1-4): 179-184.

Moradi, I., R. Mueller, B. Alijani and G. A. Kamali (2009). "Evaluation of the Heliosat-II method using daily irradiation data for four stations in Iran." Solar Energy **83**(2): 150-156.

Moustris, K., A. Paliatsos, A. Bloutsos, K. Nikolaidis, I. Koronaki and K. Kavadias (2008). "Use of neural networks for the creation of hourly global and diffuse solar irradiance data at representative locations in Greece." Renewable Energy **33**(5): 928-932.

Mubiru, J. (2008a). "Estimation of monthly average daily global solar irradiation using artificial neural networks." Solar Energy **82**(2): 181-187.

Mubiru, J. (2008b). "Predicting total solar irradiation values using artificial neural networks." Renewable Energy **33**(10): 2329-2332.

Mueller, R. W., K. F. Dagestad, P. Ineichen, M. Schroedter-Homscheidt, S. Cros, D. Dumortier, R. Kuhlemann, J. A. Olseth, G. Piernavieja, C. Reise, L. Wald and D. Heinemann (2004). "Rethinking satellite-based solar irradiance modelling: The SOLIS clear-sky module." Remote Sensing of Environment **91**(2): 160-174.

Noia, M., C. F. Ratto and R. Festa (1993a). "Solar irradiance estimation from geostationary satellite data: I. Statistical models." Solar Energy **51**(6): 449-456.

Noia, M., C. F. Ratto and R. Festa (1993b). "Solar irradiance estimation from geostationary satellite data: II. Physical models." Solar Energy **51**(6): 457-465.

Nonnenmacher, L., A. Kaur and C. F. M. Coimbra (2014). "Verification of the SUNY direct normal irradiance model with ground measurements." Solar Energy **99**(0): 246-258.

Ohmura, A., H. Gilgen, H. Hegner, G. Müller, M. Wild, E. G. Dutton, B. Forgan, C. Fröhlich, R. Philipona, A. Heimo, G. König-Langlo, B. McArthur, R. Pinker, C. H. Whitlock and K. Dehne (1998). "Baseline Surface Radiation Network (BSRN/WCRP): New Precision Radiometry for Climate Research." Bulletin of the American Meteorological Society **79**(10): 2115-2136.

Palmes, P. P., T. Hayasaka and S. Usui (2005). "Mutation-based genetic neural network." Neural Networks, IEEE Transactions on **16**(3): 587-600.

Pedro, H. T. C. and C. F. M. Coimbra (2012). "Assessment of forecasting techniques for solar power production with no exogenous inputs." Solar Energy **86**(7): 2017-2028.

Perez, R., P. Ineichen, K. Moore, M. Kmiecik, C. Chain, R. George and F. Vignola (2002). "A new operational model for satellite-derived irradiances: description and validation." Solar Energy **73**(5): 307-317.

Perez, R., S. Kivalov, J. Schlemmer, K. Hemker Jr, D. Renné and T. E. Hoff (2010a). "Validation of short and medium term operational solar radiation forecasts in the US." Solar Energy **84**(12): 2161-2172.

Perez, R., S. Kivalov, A. Zelenka, J. Schlemmer and K. Hemker Jr. (2010b). "Improving the performance of satellite-to-irradiance models using the satellite's infrared sensors." Proc. ASES Annual Conference, Phoenix, Arizona.

Perez, R., R. Seals and A. Zelenka (1997). "Comparing satellite remote sensing and ground network measurements for the production of site/time specific irradiance data." Solar Energy **60**(2): 89-96.

Perez, R. R., P. Ineichen, E. L. Maxwell, R. D. Seal and A. Zalenka (1992). "Dynamic global-to-direct irradiance conversion models." ASHRAE Transactions **98**(1): 354-369.

Pinker, R. T., R. Frouin and Z. Li (1995). "A review of satellite methods to derive surface shortwave irradiance." Remote Sensing of Environment **51**(1): 108-124.

Polo, J., F. Antonanzas-Torres, J. M. Vindel and L. Ramirez (2014). "Sensitivity of satellite-based methods for deriving solar radiation to different choice of aerosol input and models." Renewable Energy **68**(0): 785-792.

Polo, J., L. Martín and M. Cony (2012). "Revision of ground albedo estimation in Heliosat scheme for deriving solar radiation from SEVIRI HRV channel of Meteosat satellite." Solar Energy **86**(1): 275-282.

Polo, J., J. M. Vindel and L. Martín (2013). "Angular dependence of the albedo estimated in models for solar radiation derived from geostationary satellites." Solar Energy **93**(0): 256-266.

Polo, J., L. Zarzalejo, L. Ramirez and B. Espinar (2006). "Iterative filtering of ground data for qualifying statistical models for solar irradiance estimation from satellite data." Solar Energy **80**(3): 240-247.

Polo, J., L. F. Zarzalejo, M. Cony, A. A. Navarro, R. Marchante, L. Martín and M. Romero (2011). "Solar radiation estimations over India using Meteosat satellite images." Solar Energy **85**(9): 2395-2406.

Posselt, R., R. Mueller, J. Trentmann, R. Stockli and M. A. Liniger (2014). "A surface radiation climatology across two Meteosat satellite generations." Remote Sensing of Environment **142**(0): 103-110.

Quesada-Ruiz, S., Y. Chu, J. Tovar-Pescador, H. T. C. Pedro and C. F. M. Coimbra (2014). "Cloud-tracking methodology for intra-hour DNI forecasting." Solar Energy **102**(0): 267-275.

Quesada-Ruiz, S., A. Linares-Rodriguez, J. A. Ruiz-Arias, D. Pozo-Vazquez and J. Tovar-Pescador (2015). "An advanced ANN-based method to estimate hourly solar radiation from multi-spectral MSG imagery." Solar Energy **115**: 494-504.

Rahimikhoob, A. (2010). "Estimating global solar radiation using artificial neural network and air temperature data in a semi-arid environment." Renewable Energy **35**(9): 2131-2135.

Ramos Ridao, A., E. Hontoria Garcia, B. Moreno Escobar and M. Zamorano Toro (2007). "Solar energy in Andalusia (Spain): present state and prospects for the future." Renewable and Sustainable Energy Reviews **11**(1): 148-161.

Reddy, K. (2003). "Solar resource estimation using artificial neural networks and comparison with other correlation models." Energy Conversion and Management **44**(15): 2519-2530.

Rehman, S. and M. Mohandes (2008). "Artificial neural network estimation of global solar radiation using air temperature and relative humidity." Energy Policy **36**(2): 571-576.

Remund, J., L. Wald, M. Lefevre, T. Ranchin and J. Page (2003). Worldwide Linke turbidity information. ISES Solar World Congress 2003, International Solar Energy Society (ISES).

Rigollier, C., O. Bauer and L. Wald (2000). "On the clear sky model of the ESRA European Solar Radiation Atlas with respect to the Heliosat method." Solar Energy **68**(1): 33-48.

Rigollier, C., M. Lefevre, P. Blanc and L. Wald (2002). "The operational calibration of images taken in the visible channel of the meteosat series of satellites." Journal of Atmospheric and Oceanic Technology **19**(9): 1285-1293.

Rigollier, C., M. Lefèvre and L. Wald (2004). "The method Heliosat-2 for deriving shortwave solar radiation from satellite images." Solar Energy **77**(2): 159-169.

Roerink, G. J., J. S. Bojanowski, A. J. W. de Wit, H. Eerens, I. Supit, O. Leo and H. L. Boogaard (2012). "Evaluation of MSG-derived global radiation estimates for application in a regional crop model." Agricultural and Forest Meteorology **160**: 36-47.

Rubio, M., G. Lopez, J. Tovar, D. Pozo and F. Batlles (2005). "The use of satellite measurements to estimate photosynthetically active radiation." Physics and Chemistry of the Earth, Parts A/B/C **30**(1-3): 159-164.

Ruiz-Arias, J. A., D. Pozo-Vázquez, V. Lara-Fanego, F. J. Santos-Alamillos and J. Tovar-Pescador (2011a). "A High-Resolution Topographic Correction Method for Clear-Sky Solar Irradiance Derived with a Numerical Weather Prediction Model." Journal of Applied Meteorology and Climatology **50**(12): 2460-2472.

Ruiz-Arias, J. A., D. Pozo-Vázquez, F. J. Santos-Alamillos, V. Lara-Fanego and J. Tovar-Pescador (2011b). "A topographic geostatistical approach for mapping monthly mean values of daily global solar radiation: A case study in southern Spain." Agricultural and Forest Meteorology **151**(12): 1812-1822.

Ruiz-Arias, J. A., J. Tovar-Pescador, D. Pozo-Vazquez and H. Alsamamra (2009). "A comparative analysis of DEM-based models to estimate the solar radiation in mountainous terrain." International Journal of Geographical Information Science **23**(8): 1049-1076.

Schapire, R. E. (1989). The strength of weak learnability. Foundations of Computer Science, 1989., 30th Annual Symposium on.

Schillings, C., H. Mannstein and R. Meyer (2004a). "Operational method for deriving high resolution direct normal irradiance from satellite data." Solar Energy **76**(4): 475-484.

Schillings, C., R. Meyer and H. Mannstein (2004b). "Validation of a method for deriving high resolution direct normal irradiance from satellite data and application for the Arabian Peninsula." Solar Energy **76**(4): 485-497.

Schmetz, J., P. Pili, S. Tjemkes, D. Just, J. Kerkmann, S. Rota and A. Ratier (2002). "An Introduction to Meteosat Second Generation (MSG)." Bulletin of the American Meteorological Society **83**(7): 977-992.

Şenkal, O. (2010). "Modeling of solar radiation using remote sensing and artificial neural network in Turkey." Energy **35**(12): 4795-4801.

Şenkal, O. and T. Kuleli (2009). "Estimation of solar radiation over Turkey using artificial neural network and satellite data." Applied Energy **86**(7-8): 1222-1228.

Sharkey, A. J. C. (1996). "On Combining Artificial Neural Nets." Connection Science **8**(3-4): 299-314.

Sharkey, A. J. C., Ed. (1999). Combining Artificial Neural Nets: Ensemble and Modular Multi-Net Systems. New York, Springer-Verlag.

Shen, Z. Q. and S. Fan (2004). Optimizing weights by genetic algorithm for neural network ensemble. **3173:** 323-331.

Simmons, A., S. Uppala, D. Dee and S. Kobayashi (2007). "ERA-Interim: New ECMWF reanalysis products from 1989 onwards." ECMWF Newsletter No. 11.

Siqueira, A. N., C. Tiba and N. Fraidenraich (2010). "Generation of daily solar irradiation by means of artificial neural networks." Renewable Energy **35**(11): 2406-2414.

Sozen, A. (2004a). "Estimation of solar potential in Turkey by artificial neural networks using meteorological and geographical data." Energy Conversion and Management **45**(18-19): 3033-3052.

Sozen, A. (2004b). "Use of artificial neural networks for mapping of solar potential in Turkey." Applied Energy **77**(3): 273-286.

Sozen, A., E. Arcaklioglu, M. Ozalp and N. Caglar (2005). "Forecasting based on neural network approach of solar potential in Turkey." Renewable Energy **30**(7): 1075-1090.

Trevino, V. and F. Falciani (2006). "GALGO: an R package for multivariate variable selection using genetic algorithms." Bioinformatics **22**(9): 1154-1156.

Tymvios, F., C. Jacovides, S. Michaelides and C. Scouteli (2005). "Comparative study of Angström's and artificial neural networks' methodologies in estimating global solar radiation." Solar Energy **78**(6): 752-762.

Valentine, S. V. (2011). "Emerging symbiosis: Renewable energy and energy security." Renewable and Sustainable Energy Reviews **15**(9): 4572-4578.

Vignola, F., P. Harlan, R. Perez and M. Kmiecik (2007). "Analysis of satellite derived beam and global solar radiation data." Solar Energy **81**(6): 768-772.

Voyant, C., M. Muselli, C. Paoli and M.-L. Nivet (2011). "Optimization of an artificial neural network dedicated to the multivariate forecasting of daily global radiation." Energy **36**(1): 348-359.

Wahab, M. A., M. El-Metwally, R. Hassan, M. Lefevre, A. Oumbe and L. Wald (2009). "Assessing surface solar irradiance in Northern Africa desert climate and its long-term variations from Meteosat images." International Journal of Remote Sensing **31**(01): 261-280.

Wang, D. and M. Alhamdoosh (2013). "Evolutionary extreme learning machine ensembles with size control." Neurocomputing **102**(0): 98-110.

Wang, Y., D. Niu and V. C. S. Lee (2011). Optimizing of BP neural network based on genetic algorithms in power load forecasting, Melbourne, VIC.

Widén, J., N. Carpman, V. Castellucci, D. Lingfors, J. Olauson, F. Remouit, M. Bergkvist, M. Grabbe and R. Waters (2015). "Variability assessment and forecasting of renewables: A review for solar, wind, wave and tidal resources." Renewable and Sustainable Energy Reviews **44**(0): 356-375.

Wolf, R. and D. Just (1999). LRIT/HRIT Global Specification. Coordination Group fro Meteorological Satellites, EUMETSAT. CGMS 03 (Technical Report 2.6).

Yacef, R., M. Benghanem and A. Mellit (2012). "Prediction of daily global solar irradiation data using Bayesian neural network: A comparative study." Renewable Energy **48**(0): 146-154.

Yao, X. (1999). "Evolving artificial neural networks." Proceedings of the IEEE **87**(9): 1423-1447.

Yao, X. and Y. Liu (1998). "Making use of population information in evolutionary artificial neural networks." Systems, Man, and Cybernetics, Part B: Cybernetics, IEEE Transactions on **28**(3): 417-425.

Zarzalejo, L. (2005). "Artificial intelligence techniques applied to hourly global irradiance estimation from satellite-derived cloud index." Energy **30**(9): 1685-1697.

Zarzalejo, L. F., J. Polo, L. Martín, L. Ramírez and B. Espinar (2009). "A new statistical approach for deriving global solar radiation from satellite images." Solar Energy **83**(4): 480-484.

Zelenka, A., G. Czeplak, V. d'Agostino, W. Josefson, E. Maxwell and R. Perez (1992). "Techniques for supplementing solar radiation network data." Technical Report, International Energy Agency, # IEA-SHCP-9D-1, Swiss Meteorological Institute, Krahbuhlstrasse, 58, CH-8044 Zurich, Switzerland.

Zelenka, A., R. Perez, R. Seals and D. Renné (1999). "Effective Accuracy of Satellite-Derived Hourly Irradiances." Theoretical and Applied Climatology **62**(3): 199-207.

Zervas, P., H. Sarimveis, J. Palyvos and N. Markatos (2008). "Prediction of daily global solar irradiance on horizontal surfaces based on neural-network techniques." Renewable Energy **33**(8): 1796-1803.

Zhang, T., P. W. Stackhouse Jr, W. S. Chandler and D. J. Westberg (2014). "Application of a global-to-beam irradiance model to the NASA GEWEX SRB dataset: An extension of the NASA Surface meteorology and Solar Energy datasets." Solar Energy **110**(0): 117-131.